

Inaugural - Dissertation  
zur  
Erlangung der Doktorwürde  
der  
Naturwissenschaftlich - Mathematischen Gesamtfakultät  
der  
Ruprecht - Karls - Universität Heidelberg

vorgelegt von  
Dipl.-Chem. Simon Daniel Schulz  
aus Heidelberg

Tag der mündlichen Prüfung: 31. März 2009



# Application of Micropillar Interfaces: A Study on Human Periodontal Cells and Actin Biomimetic Systems

Referees:

Prof. Dr. Joachim P. Spatz

PD. Dr. Rainer Dahint



# Zusammenfassung

Mikrostrukturierte Oberflächen wie Mikrosäulen aus Polydimethylsiloxan (PDMS) schaffen einerseits einen neuartigen Ansatz zur Kultivierung von Zellen auf topologisch definierten Oberflächen auf denen man Kräfte messen kann. Andererseits dienen sie auch als Gerüst für biomimetische Untersuchungen von Protein. Im ersten Teil werden Matrizen aus PDMS-Mikrosäulen, die mit Fibronectin funktionalisiert sind, als biomechanische Mikroumgebung für immortalisierte humane Gingiva-Keratinocyten (IHGKs) und Gingiva-Fibroblasten aus dem Bindegewebe (GCTFs) verwendet. IHGKs und GCTFs adhären und wachsen auf den Pillarköpfen. Die IHGKs üben Kräfte von bis zu 110 nN und die GCTFs von bis zu 174 nN auf die Pillarköpfe aus. Eine Veränderung der Pillarabstände beeinflusst die frühe Differentiation der Keratinocyten. Bei kleiner werdenden Pillarabständen weisen die IHGKs eine zunehmende Ausbreitung von Keratin 1 (K1) im Zytoplasma, eine zunehmende mRNA Transkription von Keratin 1 und eine Veränderung ihres Aussehens von einer mehr linearen Form zu einer mehr runden Form auf. Ein neuartiges Kokultursystem aus GCTFs und IHGKs wird entwickelt, um explizit die Rolle von GCTFs in der Morphogenese von den so erhaltenen Epitheläquivalenten zu untersuchen. Für Epitheläquivalente, die für 7 und 14 Tage auf Pillarfeldern kultiviert werden, auf denen sich GCTFs befinden, wird ein Phänotyp gefunden, der ähnlicher zu dem *in vivo* Phänotyp ist, als der, der auf GCTF-freien Kulturen gefunden wird. Diese Beobachtungen werden durch den mRNA Transkriptionsgrad für Keratin 1 bestätigt.

Eine neuartige, transparente, auf PDMS-Säulen beruhende Mikrofluidicplattform wurde im zweiten Teil der Arbeit entwickelt. Diese wird hergestellt, um Modelle des Aktinkortex zu untersuchen. Sie erlaubt die Kontrolle über die physikalische und chemische Umgebung und ermöglicht Beobachtungen mittels hoch auflösender

Fluoreszenzmikroskopie. Es wird die Bildung von mit Filamin, Myosin II,  $\alpha$ -Aktinin und Magnesiumionen vernetzten Netzwerken beobachtet. Abhängig von der geometrischen Anordnung der auf den Pillarköpfen verankerten Aktinfilamenten lässt sich eine reißverschlussartige Vernetzungen beobachten. Die Vernetzungsgeschwindigkeit dieses so genannten Reißverschlusses wird sowohl durch die Flussgeschwindigkeit als auch durch die Anzahl und Anordnung der in diesem Prozess involvierten Filamente beeinflusst. Hierbei zeigt sich eine Geschwindigkeit zwischen 2-15  $\mu\text{m/s}$ . Um den Vernetzungsprozess weiter zu quantifizieren, wird die Flusszelle mit einer optischen Pinzette kombiniert. Die Entnetzungskräfte werden für die Vernetzungsmediatoren  $\alpha$ -Aktinin und Magnesiumionen gemessen. Für Magnesiumionen wird eine Kraft von 17-20 pN and für  $\alpha$ -Aktinin von 30-45 pN erhalten.

# Abstract

Microstructured interfaces such as micropillars made of polydimethyl - siloxane (PDMS) provide a novel approach both as topologically defined, force sensing substrates in cell culture as well as scaffolds for biomimetic protein assays.

This work is divided into two parts.

In the first part, PDMS micropillar arrays functionalized with fibronectin, are applied as a biomechanical microenvironment for immortalized human gingival keratinocytes (IHGKs) and gingival connective-tissue fibroblasts (GCTFs). IHGKs and GCTFs show successful adhesion and growth on the pillar heads and exert forces up to about 110 nN in the case of IHGKs and about 174 nN for GCTFs. Varying the interpillar distances affects the early keratinocyte differentiation and morphology. At decreasing inter-pillar distances the IHGKs show an increased keratin 1 (K1) extension in the cytoplasm, increased mRNA transcription of keratin 1 and a shape change from a more linear to a more round form. A novel GCTF-IHGK co-culture system is developed as a model of the epithelial tissue, to study explicitly the role of the GCTFs in the morphogenesis of the derived epithelial equivalents. The epithelial equivalents, cultured for 7 and 14 days on GCTF-populated pillar arrays, are found more similar to the *in vivo* phenotype than the GCTF-free cultures. These findings are confirmed by following the mRNA transcription levels for keratin 1.

A novel, transparent microfluidic platform, based on PDMS pillars is developed in the second part of this work. It is designed to investigate actin cortex models and to provide control over the physicochemical environment, allowing simultaneous high resolution fluorescence microscopy. The formation of crosslinking networks is observed using various crosslinkers, such as filamin, myosin II,  $\alpha$ -actinin and magnesium ions. Dependent of the geometric configuration of the actin filaments anchored

to the pillar tops, so-called zipping crosslinks are observed. The zipping velocity is both influenced by the flow speed, as well as the number and the configuration of the filaments involved in the process. It is found to range between 2 - 15  $\mu\text{m/s}$ . To further quantify the crosslinking process, the flow-cell is combined with an optical tweezers system. The unzipping forces are measured for the crosslinkers  $\alpha$ -actinin and magnesium ions. Forces of about 17 - 20 pN are derived for magnesium ions and about 30 - 45 pN for  $\alpha$ -actinin.

# Contents

<b>Zusammenfassung</b>	<b>i</b>
<b>Abstract</b>	<b>iii</b>
<b>1 General Introduction and Motivation</b>	<b>1</b>
<b>I Periodontal Cells on Microstructured Surfaces</b>	<b>3</b>
<b>2 Introduction</b>	<b>5</b>
2.1 Intermediate Filaments . . . . .	12
<b>3 Materials and Methods</b>	<b>15</b>
3.1 Fabrication of Micropillar Arrays for Cell Adhesion . . . . .	15
3.1.1 Micropillar Fabrication . . . . .	15
Fabrication of the Chromium Photomask . . . . .	16
Fabrication of the SU-8 Master . . . . .	17
PDMS-casting . . . . .	18
3.1.2 Pillar Functionalization with Fibronectin . . . . .	19
3.1.3 Force Measurements on Micropillar . . . . .	22
3.2 Cell Culture . . . . .	23
3.3 Generation of Co-Cultures (CCs) . . . . .	24
3.4 Indirect Immunofluorescence (IIF) of IHGKs on Micropillars . . . . .	26
3.4.1 IHGKs on Micropillars . . . . .	26
3.4.2 GCTFs on Micropillars . . . . .	27

3.4.3	IHGK Co-Cultures on Micropillars . . . . .	27
3.5	RNA Extraction and Quantitative Real-time PCR Analysis . . . . .	28
3.5.1	IHGKs on Micropillars . . . . .	28
3.5.2	GCTFs and Epithelial Equivalentents . . . . .	29
3.6	Scanning Electron Microscopy (SEM) . . . . .	30
<b>4</b>	<b>Early Keratinocyte Differentiation on Micropillar Interfaces</b>	<b>31</b>
4.1	Creation of an <i>in vitro</i> Model Surface for IHGKs . . . . .	32
4.1.1	Traction Forces exerted by Keratinocytes on Micropillar Fields. . . . .	35
4.2	Keratinocyte Morphology and Expression of K1 and K10 on Microstructured Surfaces . . . . .	37
4.2.1	Morphology . . . . .	37
4.2.2	Expression of K1/10 . . . . .	42
<b>5</b>	<b>GCTFs and Epithelial Equivalentents on Micropillars</b>	<b>47</b>
5.1	GCTFs on Micropillars . . . . .	48
5.2	Co-Cultures of GCTFs and IHGKs on Micropillars . . . . .	52
<b>6</b>	<b>Conclusion and Outlook</b>	<b>57</b>
<b>II</b>	<b>Biomimetic Actin Networks</b>	<b>61</b>
<b>7</b>	<b>Introduction</b>	<b>63</b>
7.1	Protein filaments . . . . .	66
7.1.1	Microtubules . . . . .	66
7.1.2	Intermediate Filaments . . . . .	67
7.1.3	Actin . . . . .	68
7.2	Actin Binding Proteins (ABPs) . . . . .	71
7.2.1	Filamin . . . . .	71
7.2.2	$\alpha$ -Actinin . . . . .	72
7.2.3	Myosin II . . . . .	73
7.3	Optical Tweezers . . . . .	74
<b>8</b>	<b>Materials and Methods</b>	<b>77</b>
8.1	Microfluidic Devices . . . . .	77

8.1.1	Fabrication of the Photomask for the Flow-Channel . . . . .	78
8.1.2	Fabrication of the Master for the Flow-channel . . . . .	79
8.1.3	PDMS-casting and Flow-cell Assembly . . . . .	80
8.2	Actin, Actin-Binding-Proteins and Buffer Solutions . . . . .	80
8.2.1	Actin . . . . .	81
	Isolation and Purification . . . . .	81
	Storage and Dialysis . . . . .	82
	Polymerization and Staining . . . . .	82
8.2.2	Actin Binding Proteins . . . . .	84
	Myosin II . . . . .	84
	Filamin . . . . .	86
	Alpha Actinin . . . . .	86
8.3	Microparticles for OT experiments . . . . .	86
8.4	Microscopy . . . . .	87
8.4.1	Light Microscopy . . . . .	87
8.4.2	Optical Tweezers . . . . .	87
<b>9</b>	<b>Biomimetic of quasi 2-dimensional Actin Networks on PDMS-Micropillars</b>	<b>91</b>
9.1	Actin Network Assembly in a Flow-cell . . . . .	92
9.2	Crosslinked actin networks . . . . .	93
9.2.1	Filamin . . . . .	94
9.2.2	Divalent Cations . . . . .	95
9.2.3	Myosin II . . . . .	95
9.3	Actin Zipping . . . . .	99
9.3.1	The Theory of Zipping . . . . .	103
9.3.2	The Experiment . . . . .	107
<b>10</b>	<b>Unbundling Forces of Freely Suspended Crosslinked F-actin measured by Optical Tweezers</b>	<b>111</b>
10.1	Unzipping Forces of Actin Bundles . . . . .	112
<b>11</b>	<b>Conclusion and Outlook</b>	<b>119</b>
	<b>List of Figures</b>	<b>123</b>
	<b>Bibliography</b>	<b>127</b>

<b>Appendix</b>	<b>151</b>
<b>A Abbreviations</b>	<b>153</b>
<b>B Own Publications</b>	<b>155</b>

## General Introduction and Motivation

The interplay between the different factors governing proper cell function *in vivo* is very complex. In cell biology this system is commonly simplified to culture dishes to investigate the cellular machinery. These artificial substrates are usually made of special treated plastic or glass. However, *in vivo*, most cells are embedded in the extracellular matrix (ECM). The ECM is made of different protein fibers, providing an elastic surrounding for cells which are linked to the ECM via adhesion-mediating transmembrane proteins. In common culture dishes cells flatten quickly and develop stress fibers, which consist of filamentous actin and actin-associated proteins. However, cells *in vivo* do not show prominent stress fiber formation. This suggests that findings for cells, forced to adjust to flat and rigid surfaces are distorted, which depicts the difficulty in *in vitro* studies in cell biology.

Improvements in material technology enabled scientists to create biofunctionalized elastic substrates for cell culture. In comparison to rigid surfaces, a reduced spreading and increased motility of cells on elastic substrates was observed.<sup>[1]</sup> Moreover, a new generation of model surfaces made of polydimethyl-siloxane (PDMS) offered mechanically and topographically tunable surfaces. Pillar arrays of this elastic material were used as micromechanical sensors for the measurement of mechanical interactions between cells and their underlying substrate.<sup>[2]</sup> It was shown, that the topography of pillars influence cell morphology and migration.<sup>[3]</sup> This suggests, that also decisive cell functions, like differentiation and proliferation, must be dependent on the presented substrate.

The mechanical feedback of cells to the extracellular environment is mediated by their cytoskeleton. The cytoskeleton is mainly responsible for the mechanical prop-

erties of a cell. There are still many open questions regarding the biophysics and the mechanics of the cytoskeleton.<sup>[4]</sup>

One of the major cytoskeletal components is the actin cortex, which is responsible for the cell's shape. The cortex is a partially crosslinked quasi two-dimensional network, which is attached point-wise to the plasma membrane. There is evidence that such networks with infinite lateral extension differ in their physical properties from three-dimensional networks.<sup>[5,6]</sup> However, the mechanical properties of extended two-dimensional actin networks are largely unknown. Moreover, it is often difficult to distinguish between effects directly mediated by this network or generated by other sources. In recent studies, arrays of silicon micropillars were employed as a scaffold to assemble actin networks and manipulate them by crosslinkers.<sup>[7]</sup>

The aim of this work was to create elastic microstructured substrates for periodontal cells. We intended to gain insight in the mechanics and decisive cell functions of periodontal cells dependent on the configuration of the presented substrates. Moreover, we wanted to fabricate epithelial equivalents, which closely resemble the *in vivo* situation.

Additionally, to understand, which factors in detail are involved in the mechanics of a cell, it is necessary to consider the cytoskeleton. To simplify the complex interplay in the cell we aimed to create a biomimetic model of the actin cortex. Therefore, a physicochemical controlled microenvironment, containing transparent obstacles, was necessary. Using this device we intended to following the dynamics and to measure the forces of crosslinking. Finding out more about the biophysics of such extended protein networks would help to better understand the mechanical behavior of cells as a whole.

## **Part I**

# **Periodontal Cells on Microstructured Surfaces**



## Introduction

*In vivo*, cells behave in many complex ways. Their cellular characteristics such as replication, proliferation, differentiation, migration, morphogenesis and apoptosis are usually influenced by a variety of different factors. To reduce the complexity of *in vivo* systems, most investigations on the influence of different factors regarding cell fate are downscaled to the *in vitro* level. Commonly cells are cultured on glass coverslips or plastic culture dishes. Both exhibit a very hard substrate for the cells (elastic modulus  $E \sim 1$  GPa) whereas *in vivo* tissue from where the cells are extracted is relatively soft. This combination of adherent cells and molecules from the extracellular matrix (ECM) establishes an elastic environment for these cells. The elastic moduli  $E$  of tissue, formed by different cell types, range from  $\sim 0.5$  kPa in brain tissue to  $\sim 10$ - $20$  kPa in unstimulated muscle, to skin, which has an elastic modulus of  $\sim 50$  kPa.<sup>[8-10]</sup> Cultured cells under standard culture conditions usually flatten quickly and develop predominant stress fibers composed of F-actin, myosin and F-actin associated proteins. The assembly of stress fibers in culture has been observed through electron microscopy by Buckley and Porter in 1967<sup>[11]</sup> and through fluorescence microscopy by Schloss in 1977<sup>[12]</sup> and Goldman in 1979.<sup>[13]</sup> Compared to this *in vitro* situation a remarkable contrast to the one *in vivo* was observed. Migrating fibroblasts, for example, do not contain stress fibers if they are embedded in a ECM.<sup>[14]</sup> These findings suggest that cells "sense" their environment, and that the cells are not only affected by chemical signals like cytokines, chemokines and growth factors or by physical interactions with fibronectin and collagens, but also respond on their various extracellular environments. This inspired the development of substrates suitable for cell culture which are tunable in stiffness and shape. In

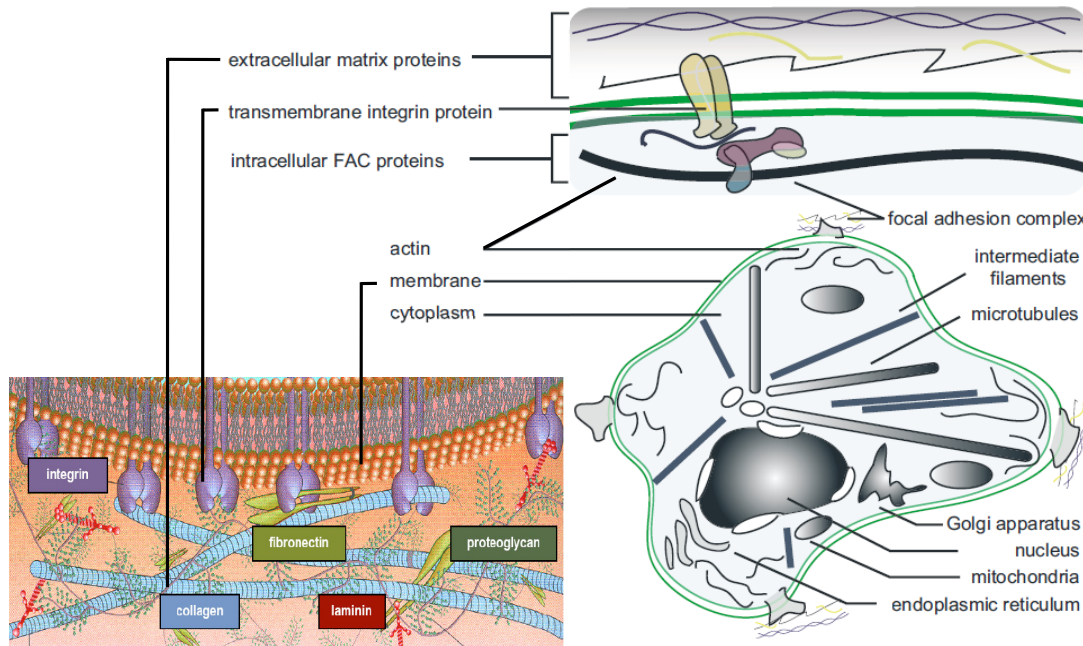


**Figure 2.1:** Schematic view of an eucaryotic cell linked to the ECM in a connective tissue. The proteins of the ECM like collagen and fibronectin are linked to the cell via adhesion-mediated transmembrane proteins, such as integrins. Images are adapted from [20,21].

1997 Pelham was the first, who observed reduced spreading and increased motility of epithelial and fibroblastic cells on collagen-coated polyacrylamide gel in comparison to cells cultured on rigid surfaces.<sup>[1]</sup>

Most cells in living organisms are embedded in extracellular matrix (ECM). Adhesion to this matrix and to neighboring cells plays an important role in fundamental cell functions.<sup>[15,16]</sup> The process of the molecular domains involved in cell-matrix interaction is very complex.<sup>[14]</sup> It was found that the cell's mechanosensing to the surrounding influences many cell functions: Changes in gene expression, proliferation and differentiation were observed and even the direction of stem cell fate stem cell fate could be influenced.<sup>[17-19]</sup>

In the ECM, five classes of macromolecules can be found: proteoglycans, hyaluronan, elastin, collagen, and adhesive glycoproteins. They all vary in organization and have different mechanical properties. The ECM-molecules like collagen, laminin or fibronectin bind via transmembrane receptors to the cell membrane (Fig. 2.1).

The ECM in tissue consists of a meshwork of fibers of glycoproteins and collagen embedded in a gel-like substance formed out of glycosaminoglycans and proteogly-

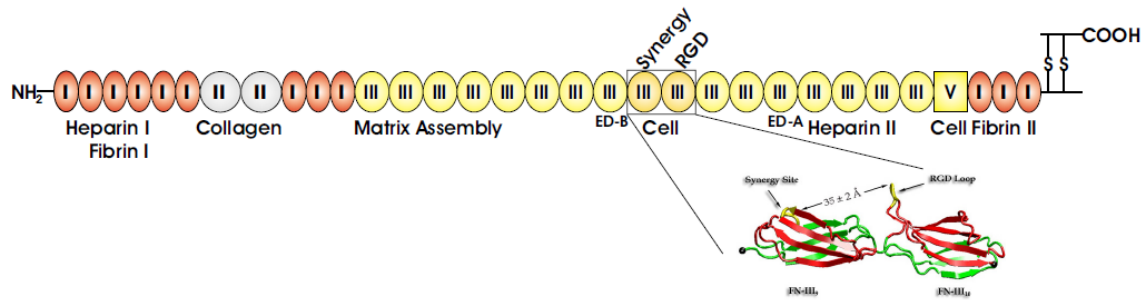


**Figure 2.2:** Schematic view of a fibronectin. The fibronectin chain has the three structural motifs, I, II and III. The major cell-binding site can be found on the 10th repeat of motif III containing the RGD-loop and a synergy region. Image is adapted from [23].

cans that store water by osmotic pressure. The ECM provides mechanical support for the cell, traffic routes for cellular migration and strongly influences embryonic development as well.

One of the major proteins found in the ECM of tissues like epithelial and connective tissue is Fibronectin (FN). Three types of FN have been identified so far. [22] FN consist of monomers of about 235 kDa, forming a large antiparallel homodimer, and contains various binding sites for proteins which are located along the fiber. The most prominent binding sites are the collagen binding domain in the FN II-motif and the cell-binding region in the FN III-motif (Fig. 2.2).

The cell binding region contains the so-called RGD-motif which is a repeated sequences of the amino acids arginine, glycine and asparagine. This motif is recognized by many cells, so it is often used as an adhesion linker.

The second fibrous protein which plays a crucial role in the ECM of connective tissue is collagen. In vertebrates, there are at least 16 types of collagen known. The major constituents in the body are collagen I, II and III whereas the basal lamina is formed by collagen IV. Collagen is synthesized from cells as procollagen and cleaved enzymatically in the extracellular space and assembled to fibers. [24] The collagen I base unit forms a triple helical structure which is 300 nm long and 1.5 nm thin. The high abundance of the tripeptide glycin-prolin-hydroproline is remarkable.

The mechanical properties of the extracellular environment of cells, like the topology and stiffness of the ECM, influence the ability of cells to exert forces to the substrate. [25,26]

Forces that are produced by single cells usually range from several nN to several

hundreds of nN while the forces produced by single molecular motors or protein-protein interactions are in the pN regime. In general, several approaches have been developed to measure these forces in biology, and further on to elucidate the relationship between substrate mechanics, cell adhesion and traction forces as well as to determine the viscoelastic properties:

- Micropipette aspiration: This is a widely used technique to study time-dependent deformation of living cells. To this end, individual cells were subjected to an extracellular pressure, while they were drawn with pressure into a defined glass tube. For example, it has been used to investigate the viscoelastic contribution of the cortex.<sup>[27,28]</sup>
- Single cell stretcher: In this case a cell is adhere between a hard and a soft glass micro-plate with a known spring constant. The cell is pulled by the hard plate and the forces can be measured by deflection of the soft plate. With this technique the viscoelastic properties of malignant cells were investigated.<sup>[29]</sup>
- Optical tweezers (OT): The improvements in image acquisition and processing techniques and the development of accurate light sources made it possible to measure forces with pN resolution with optical tweezers. A dielectric particle is trapped in a focused laser beam by generating a momentum on the particle. The laser trap has a certain stiffness  $k$  which typically is in the order of  $k = 50$  pN/ $\mu\text{m}$ .<sup>[30]</sup> If the particle is displaced from the focus of the trap either through active or passive forces the exerted forces can be calculated by  $F = -kx$ , whereas  $x$  is the displacement. Due to its high accuracy the OT is often used in single molecule experiments like the step-wise behavior of kinesin<sup>[31,32]</sup> or myosin V.<sup>[33,34]</sup> A possibility to derive unzipping forces of crosslinked actin bundles *in vitro* will be presented within this work in chapter 10.
- Atomic force microscopy (AFM): The principle of this technique is based on the measurement of the deflection of a cantilever with a known spring constant which applies mechanical force across a sample surface in one or more spatial dimensions. It affords Angstrom-scale positioning accuracy. Using AFM it was shown that actin filaments contribute more to the mechanical stiffness of the cell than do microtubules, despite the fact that microtubules have a higher bending stiffness.<sup>[35]</sup>

- Flexible Substrates: The engineering of soft material suitable for cell culture such as polyacrylamide or polydimethyl-siloxane (PDMS) gels<sup>[36,37]</sup> opened a new field of investigation on the influence of mechanical signals from a substrate on a cell's behavior. Flexible substrates provide a wide variety of possible modifications: They have a tunable Young's modulus, can be bio-functionalized, and microstructured. Since the patterns used in this work are biofunctionalized arrays of obstacles made of PDMS, the different applications and different approaches to derive quantitative data from cell experiments on flexible substrates will be described in detail as follows.

For the first time, Harris *et al.* observed traction forces of locomotive fibroblasts and other cell types as wrinkles in a thin film of PDMS. The length and the number of wrinkles gave a rough estimation of traction forces. This tool gave insights in the molecular pathway that regulates stressfiber formation, traction force and focal adhesion assembly.<sup>[38,39]</sup> To better exert traction forces, first latex beads were embedded to quantify the film distortions more accurately during cell migration.<sup>[40]</sup> Durotaxis was observed for fibroblasts on a flexible polyacrylamide gel, which had different stiffness, coated with collagen I.<sup>[41]</sup> Fluorescent microbeads were embedded into polyacrylamide gels to determine the displacement fields of the beads more precisely.<sup>[42]</sup> By imprinting arrays of these beads onto elastic substrates, traction forces of an individual focal adhesion could be measured more precisely than on substrates with randomly seeded beads.<sup>[43]</sup> Furthermore, flat substrates were used to elucidate the forces exerted by cells on flexible substrates.<sup>[44–48]</sup> However, one major drawback of the flat substrates emerges from their limited resolution in traction-force microscopy, which is described by the elastic Green functions<sup>[49]</sup>, and results from the surface thickness.<sup>[47]</sup>

To avoid this problem, Galbraith *et al.* fabricated cantilevers that deflected parallel to the plane of cell migration.<sup>[50]</sup> Cells, migrating under the microcantilevers, deflected these and allowed a simple calculation of the exerted forces. Tan *et al.* presented an array of vertical cantilevers made of PDMS which allowed determination of forces on different locations of the cell (Fig. 2.3).<sup>[2]</sup> They showed that induced spread muscle cells exerted forces on the substrate by bending these cantilevers while induced non-spread cells did not.

Since then, fabricated arrays of flexible microposts were the key issue in many investigations considering the influence of substrate's morphology and stiffness and the

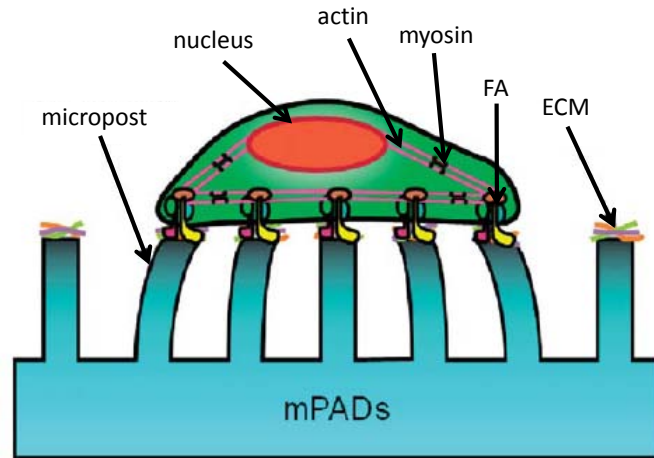


**Figure 2.3:** Schematic view of a cell adhered on a pillar. The cell can exert forces on the pillars and bend them. These forces can be derived by knowing the dimensions of the pillars, their elastic modulus and the deflection. Image is adapted from<sup>[53]</sup>.

measuring of laterally exerted forces of cells. Investigations on migrating epithelial cells showed that the traction forces exerted by the leading edge of a cell layer were higher than that of a single cell.<sup>[51]</sup> In comparison with flat surfaces, topography effects were shown on cell shape and movement of fibroblasts, grown on microstructured surfaces.<sup>[3]</sup> Forces exerted by heart cells in the excited and relaxed state were observed as well.<sup>[52]</sup>

In the presented studies, FN-biofunctionalized micropillar arrays were fabricated to investigate decisive cell functions in human gingival keratinocytes. These arrays were able to provide a defined tunable mechanical micro environment to the cells.

We focused on differentiation and morphogenesis of gingival keratinocytes (GKs) and gingival connective tissue fibroblasts (GCTFs). The gingiva covers the alveolar bone and tooth root to a level just coronal to the cemento-enamel junction and is classified anatomically into the free, the interdental and the attached gingiva<sup>[54]</sup>, whereas histologically it can be distinguished into the epithelial structure and the underlying connective tissue (Fig. 2.4).

The thickness of the oral epithelium is roughly 0.2-0.3 mm.<sup>[56]</sup> It can be distinguished in the stratum basale (basal layer), stratum spinosum (prickle cell layer), stratum granulosum (granular layer) and the stratum corneum (cornified layer). The basement membrane separates the epithelium from the connective tissue. The cells in the epithelium are called keratinocytes because they derive their structural in-

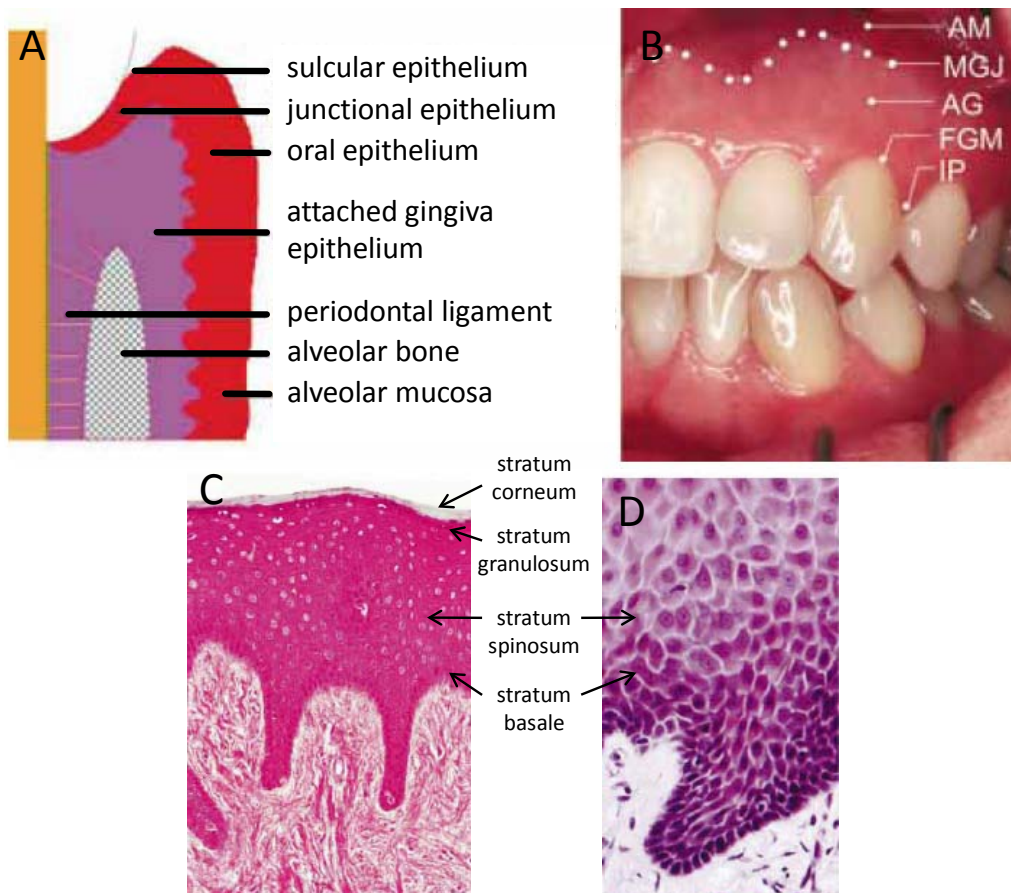


**Figure 2.4:** The structure of the gingiva. (A) Schematic view of the structure of the gingiva. (B) Shortcuts indicate the the mucogingival junction (MGJ), which separates the attached gingiva (AG) from the alveolar mucosa (AM), clinical landmarks include the free gingiva at the cervical margin of the teeth (FGM); the interdental papilla (IP). The low-power view (C) and the high power view (D) show the histology of a human gingival epithelium. In (D) the cuboidal morphology of cells in the basal layer and the polygonal shape of cells in the spinous layer. Images are adapted from<sup>[55]</sup>.

tegrity from the expression of specific cytokeratins, which are a class of intermediate filaments. The cells of the basal layer proliferate continuously into daughter cells that mature into keratinized fully differentiated cells. The basal keratinocytes in the stratified epithelia express the keratins K5, K14, K19 and K15. Keratinocytes of the the suprabasal cell compartment in the gingiva and the hard plate express keratin 1 and 10 in their early differentiation stages. The prickle cell layer is the thickest layer containing keratinized fully differentiated keratinocytes. Towards the cornified layer the cells become flattened until they are almost completely flattened

and closely aligned in the cornified layer. Mechanical stimuli are expected to play an important role for tissue integrity.

In the past, it was believed that fibroblasts of connective tissue, which are of mesenchymal origin, are only passive contributors to the tissue while nowadays they are expected to contribute actively to tissue phenotype and play an important role for the maintenance of epithelial tissue homeostasis.<sup>[57]</sup> Also, they play a key role in development, maintenance and repair of gingival connective tissue.

In the presented study, we focused on the differences in the amount and distribution of the early keratinocyte markers keratin 1 and 10, and the morphology expressed by human gingival keratinocytes on microstructured elastic supports. Additionally, we investigated the influence of connective tissue fibroblasts, precultured on these structures, on the epithelial morphogenesis.

The presented work was done in collaboration with Thorsten Steinberg, Eva Müssig and Pascal Tomakidi *et al.* and was published recently.<sup>[58,59]</sup>

## 2.1 Intermediate Filaments

Intermediate Filaments (IFs) are strong, stress resistant filaments. In cells IFs have a diameter of 10 nm (which is between actin and microtubules) and they usually have a length of roughly 47 nm. There are no motor proteins known which are associated to IFs. Despite the fact that IFs are less investigated than other cytoskeletal components, there are 6 classes of IFs known, in which proteins like nestin, lamin, neurofilaments, vimentin, desmin and keratin can be found. Two of these proteins form a coiled-coil homo- (e.g. laminin) or a hetero-dimer (e.g. keratin) which associates anti-parallel to a tetramer. These tetrameres form protofilaments by head-to-head assembly. Eight of these protofilaments form one IF (Fig. 2.5).

They prevent excessive stretching and provide a mechanical support for cells.<sup>[60]</sup> IFs attached to desmosomes and hemidesmosomes on the plasma membrane and the nuclear envelope respectively form a continuous network. Through this network desmosomes transmit forces from cell to cell and hemidesmosomes to the extracellular matrix. The continuum of IFs is especially crucial for epithelial cell integrity. Epithelial cells devote most of the protein-synthesizing machinery to produce an extensive intermediate filament network composed of keratin.<sup>[61]</sup> Keratin knock-out experiments point out the pivotal role of keratin for the mechanical integrity of

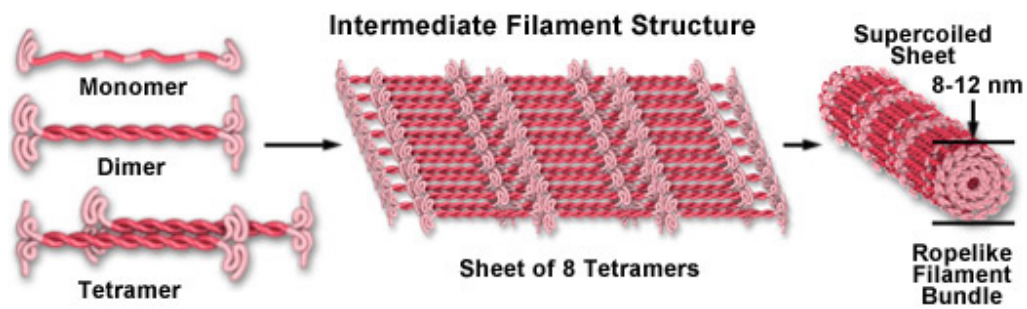


**Figure 2.5:** Structure of intermediate filaments. Two of the intermediate filament proteins of the same class form a coiled-coil homo- (e.g. laminin) or a hetero-dimer (e.g. keratin) which associates anti-parallel to a tetramer. These tetrameres form protofilaments by head-to-head assembly. Eight of these protofilaments form one IF. (<http://micro.magnet.fsu.edu/cells/intermediatefilaments/intermediatefilaments.html>).

cells. <sup>[61-63]</sup>



## Materials and Methods

### 3.1 Fabrication of Micropillar Arrays for Cell Adhesion

The micropillars used in the cell experiments presented in the next chapters were made of poly-dimethyl-siloxan (PDMS) (Sylgard 184, Dow Corning, USA). PDMS is a elastic, transparent, non-toxic and hydrophobic polymer without remarkable background fluorescence. The prepolymerized PDMS contains a vinyl-terminated 250 units long dimethyl-siloxane prepolymer mixed with a few weight percentage of a platinum catalyst as the base and a short hydrosilane as the crosslinker. Usually the base and the crosslinker are mixed vigorously at a weight ratio of 10:1 and polymerized at 65°C for at least 4 h. The prepolymer crosslinks in a catalytic cycle with the hydrosilane (Fig. 3.1). The resulted polymer has an Young's modulus  $E$  between 1-10 MPa depending on its mixture ratio and the curing parameters. This polymer can be used to fabricate micropillar structures by standard photolithography with desired geometry, stiffness and functionalization. This will be presented in the following sections.

#### 3.1.1 Micropillar Fabrication

In order to obtain a microstructured field with the desired dimensions, the first step in photolithography is to produce a chromium photomask. The mask is needed to later illuminate the master for the fabrication of microstructures. All steps for lithography must be done under cleanroom conditions and in yellow light to avoid

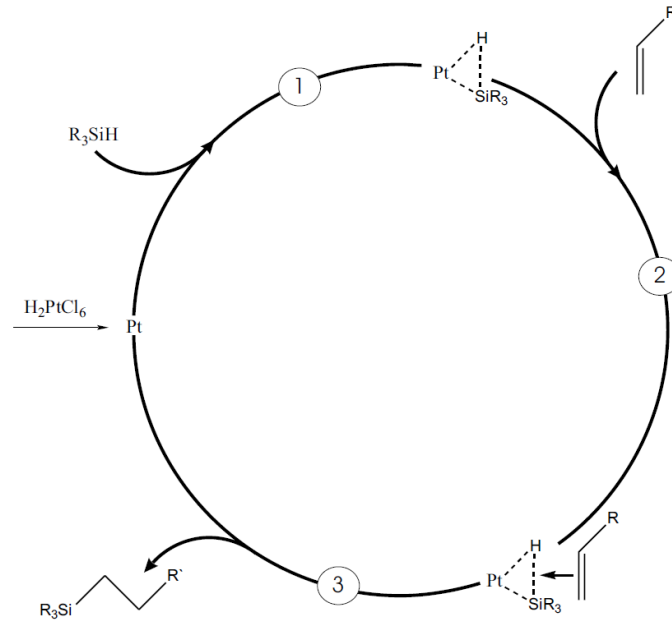


**Figure 3.1:** Catalytic cycle of the PDMS-hydrosilylation. (1) The platinum catalyst coordinates between the Si-H bond of the hydrosilane. (2) the vinyl-group of the oligo-dimethyl-siloxane is also complexed followed by a formation of a single bond between the complexed components and the release of the catalyst (3).

dust contamination and undesired illumination of the photoresist used.

### Fabrication of the Chromium Photomask

The positive photo resist AZ-1505 (Microchemicals, Ulm) was deposited on a  $5 \times 5$  cm glass slide via spin coating (3500 rpm, 25 s) to obtain a thin and homogenous layer of resist. To evaporate the dissolvent the coated glass was left in an oven at  $80^\circ C$  for 30 min. Then the desired structure was written into the resist by a laser mask writer (DWL66, Heidelberg Instruments, Heidelberg). The control file which contained the information for the structure was created in AutoCAD software (Autodesk, San Rafael, CA) or by a comparable software before writing. After the exposure the structure was developed for 1 min in AZ-351 developer (1:6 diluted in water). Since the AZ-1505 is a positive photoresist it is important to note that for pillar production only the regions for the pillars should be illuminated which comes clear later. The developed structure was sputter coated with a  $\sim 120$  nm non-transparent chromium layer (20 s/120 s, 120 mA,  $1.3 \times 10^{-2}$  mbar in argon atmosphere, Sputter Coater

MED020; Bal-Tec, Balzers, Lichtenstein) followed by resolving the remaining resin from the surface with acetone. The chromium only remained at the exposed areas and lifts off at the unexposed ones. A schematic drawing of the described processes is shown in Fig. 3.2.

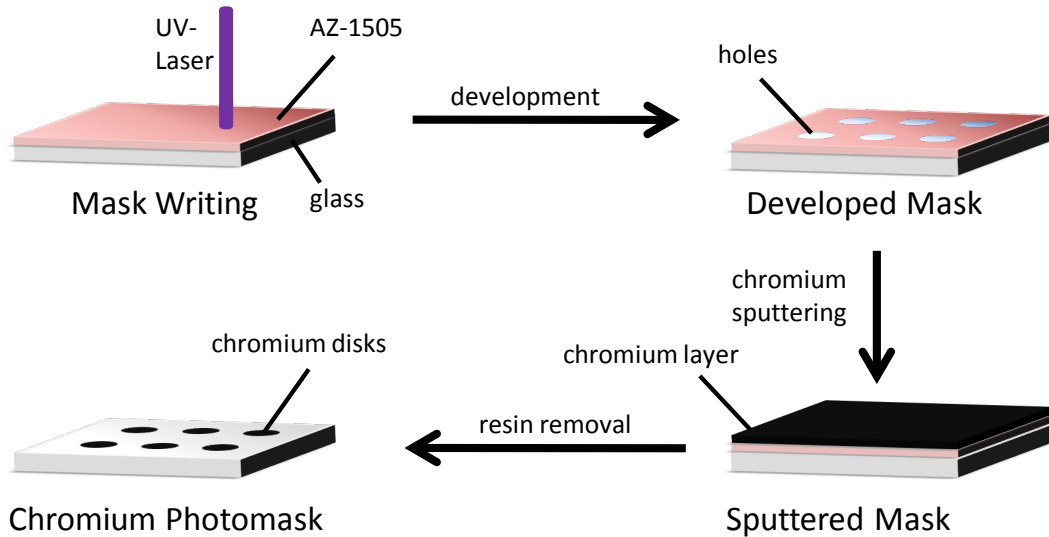


**Figure 3.2:** Scheme of steps for the production of a chromium photomask. A UV-laser writes the desired structure on a glass surface coated with resist. By development the exposed areas are dissolved from the substrate. After chromium sputtering, the remaining resin, and with it the chromium layer, is removed and the desired chromium mask is obtained.

### Fabrication of the SU-8 Master

For the fabrication of the masters the photoresist SU-8 was used (MicroChem Corp., Newton, MA). SU-8 is based on aromatic monomers containing 8 epoxy groups and a triaryl-sulfonium salt as photoinitiator. During exposure to UV-light, the salt is converted into its acid. In the following heating process it polymerizes the epoxy groups in a ring opening reaction. SU-8 is therefore a negative resist. The resin is of remarkable thermal and chemical stability and is a widely used tool in photolithography.

The resist was poured on a dry (15 min at 200°C), dust free silicon wafer (2" p/Bor 100, Si-Mat, Landsberg). There are several sorts of SU-8 available with different viscosities adjusted by the ratio of epoxy to solvent. For resin thicknesses between

10 and 15  $\mu\text{m}$  SU8-10 is the most suitable. The followed parameters are valid for resin thicknesses of 15 $\mu\text{m}$ , since a later pillar height of 15  $\mu\text{m}$  is desired whereas the principal steps remain for different thicknesses as well. The silicon wafer was spun for 7 s at 500 rpm followed by fast acceleration to 2000 rpm, which was held for 40 s.

To evaporate the solvent, the coated wafer was soft-baked prior to exposure on a hotplate at 65°C for 2 min followed by a temperature of 95°C for 5 min. This two-step process was performed in order to reduce internal thermal stress in the resin layer. The wafer was cooled down to room temperature (RT) for several minutes. After that the wafer was mounted in a mask aligner (MJB3, Karl Suss, München), equipped with a 350 W mercury lamp and exposed in hard contact mode. The exposure times for a resin layer of a thickness of 15  $\mu\text{m}$  varied between 2.0 and 2.5 seconds.

To complete the crosslinking (post exposure bake), the wafer was heated for 1 min at 65°C followed by heating at 95°C for 2 min and slowly cooling down to RT for several minutes. This step was again crucial in order to avoid thermal stress in the crosslinked resin. After that the structure was developed in SU-8 developer mrDEV-600 (MicroChem Corp., Newton, MA) for 1 min, washed clean for 10 s with fresh developer and blown dry in a nitrogen stream.

The fabrication parameters are again listed in Tab. 3.1. The obtained wafers were passivated with 1H,1H,2H,2H-perfluorooctyltrichlorosilane (ABCRC, Karlsruhe) to facilitate the later detachment of PDMS from the structure. The wafers were placed in a desiccator and 100  $\mu\text{l}$  of the silane was added. The desiccator was evacuated and kept closed overnight. The air sensitive silane reacted with the moisture and formed a covalently bound layer with the silane. After vapor deposition the wafers were rinsed with ethanol and water and blown dry under a stream of nitrogen.

### PDMS-casting

The PDMS was mixed vigorously at a ratio base to crosslinker 10:1. The mixture was degassed in a desiccator for 10 min at  $6 \times 10^{-2}$  mbar to remove trapped gas. Then a drop of PDMS was poured on a dry and clean 24 $\times$ 24 mm coverslip and the master was pressed upside down onto the PDMS. Thereafter the polymer was crosslinked at 65°C for 6 h. The substrates were cooled down to RT and the master and the overlapping parts of PDMS were removed from the coverslip with a razor blade under

**Table 3.1:** Photolithographic process of SU-8 mould fabrication of micropillars with a height of 15  $\mu\text{m}$ .

Process Step	Parameter
<b>Waver preparation</b>	Drying: 2 inch silicon wafer 15 min at 200°C
<b>Application of resin</b>	Spin coating: 2 ml SU8-10: 7 s at 500 rpm 35 s at 2000 rpm
<b>Soft bake</b>	Hot plate: 2 min at 65°C 5 min at 95°C
<b>Exposure</b>	350 W HBO, (MJB3): 2-2.5 s
<b>Post exposure bake</b>	Hot plate: 1 min at 65°C 2 min at 95°C
<b>Development</b>	SU8 developer mrDEV-600: 1 min/10 sec

sterile conditions. The result was a thin layer of PDMS on glass microstructured with an array of micropillars.

The obtained pillar fields showed a regular distance and diameter (Fig. 3.3 (A)) with a cylindrical shape of every single pillar (Fig. 3.3 (B)). Fig. 3.4 shows again the single steps for the formation of the micropillar arrays schematically.

### 3.1.2 Pillar Functionalization with Fibronectin

To provide better adhesion points for cell spreading the pillars have to be functionalized. Fibronectin (FN) was chosen for biofunctionalization since it is a protein ubiquitously found in the extracellular matrix of nearly every tissue. Cells bind to the RGD-region of the FN.

PDMS is a hydrophobic polymer. The additional surface structuring in micrometer size makes the surface superhydrophobic. This effect is often called the "lotus-

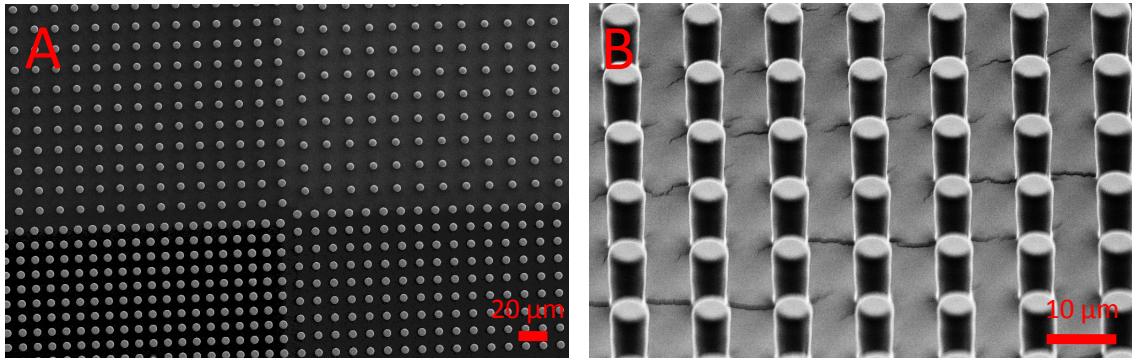


**Figure 3.3:** SEM-Pictures of microfabricated pillar arrays. (A) shows a field of pillars with an inter-pillar distance of  $5\ \mu\text{m}$ ,  $7\ \mu\text{m}$ ,  $9\ \mu\text{m}$  and  $11\ \mu\text{m}$  on one sample. The pillar diameter is  $5\ \mu\text{m}$ . And angle view reveals a reasonable cylindrical shape of the obstacles (B).

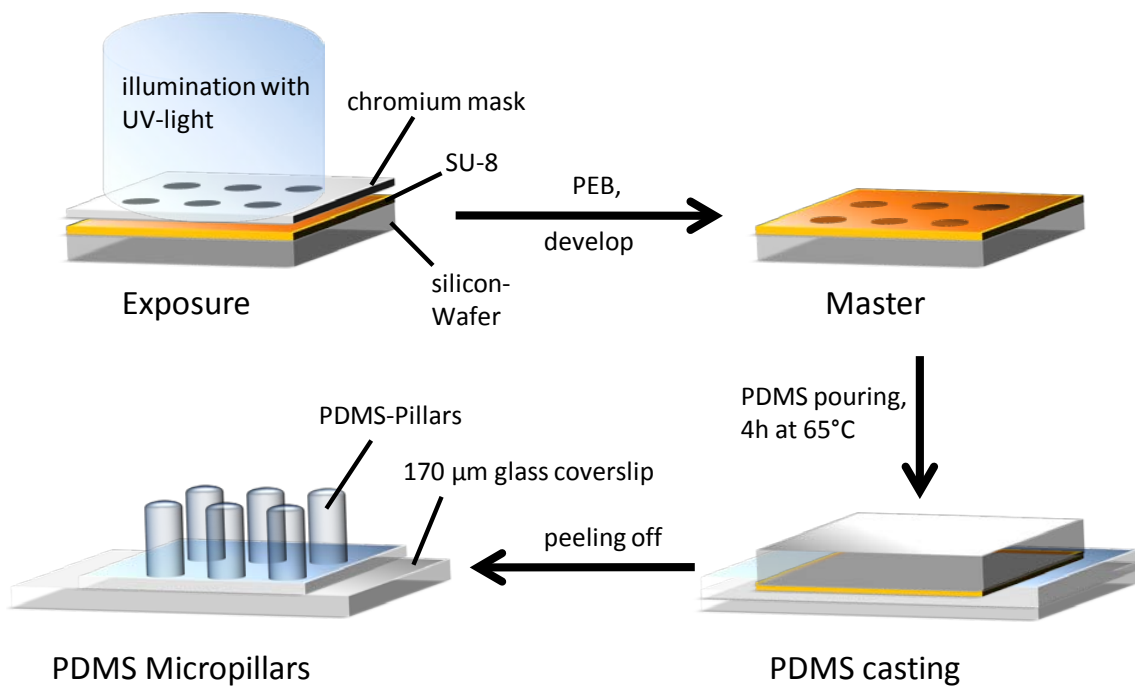


**Figure 3.4:** Scheme of the steps needed for PDMS mould fabrication. After spincoating a layer of SU8 with desired thickness onto a silicon wafer, the photoresist is illuminated through a photomask. After development of the structures the PDMS is cured. As the last step the master is removed to obtain the microstructures.

effect”. It is shown, that microstructured polymer surfaces can provide superhydrophobicity.<sup>[64-67]</sup>

For depositing FN only on the pillar tops, drops (100  $\mu\text{l}$ ) of a FN solution (1 mg/ml, Sigma-Aldrich GmbH, München, Germany) in phosphate buffered saline (PBS) were pipetted carefully to the surfaces and incubated for 10 min at 4°C. Immediately after withdrawing the drop, the surface was rinsed with PBS and directly used for cultivating cells on the pillar arrays.

Proteins in general adsorb relatively fast on essentially all synthetic surfaces but as well can undergo denaturation. The degree of denaturation is hard to predict and is dependent on many factors like the structure of the protein and the surface, the concentration of the protein and the composition of the solution.

Indirect immunofluorescence (IIF) of FN on the functionalized microstructures revealed both adsorption of FN only to the pillar tops, even at a micropillar distance of 11  $\mu\text{m}$ , and maintaining functionality of the FN (Fig. 3.5). These biofunctional-

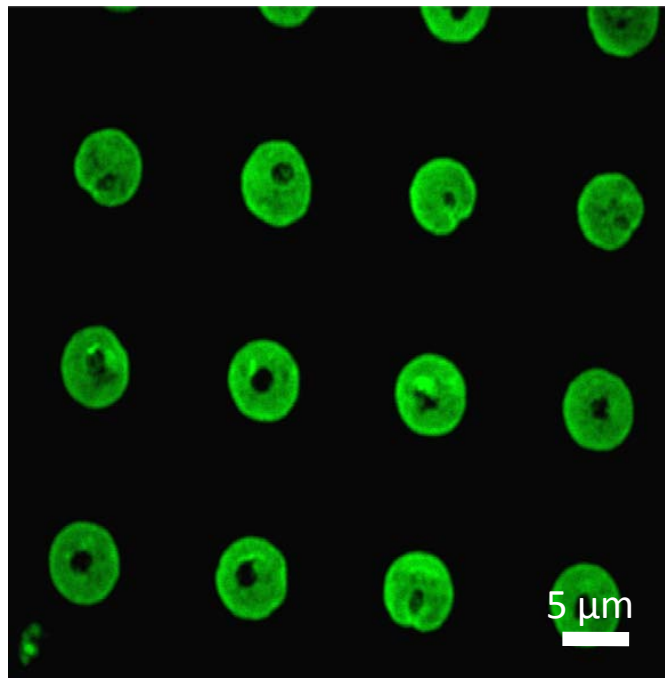


**Figure 3.5:** IIF of FN(green) on micropillars with an inter-pillar distance of 11  $\mu\text{m}$ . It indicates FN-functionalization only to the pillar tops and remaining functionality of the FN. The scalebar corresponds to 5  $\mu\text{m}$ .

ized microstructures are considered to be a reasonable substrate for the cell studies, which will be presented in the next chapters.

### 3.1.3 Force Measurements on Micropillar

As already mentioned one single pillar can be considered as a linear beam and act as a spring with a spring constant  $k$ . The force that is generated on a pillar is therefore

$$F = -k\Delta x \quad (3.1)$$

where  $\Delta x$  is the deflection of the pillar. According to the elastic beam theory of Landau and Lifshitz the spring constant for small deflections can be calculated to be

$$k = \frac{3}{4}\pi E \frac{r^4}{L^3} \quad (3.2)$$

where  $E$  is the Young's modulus of the material,  $r$  and  $L$  are the radius and the length of the pillar respectively (Fig. 3.6).<sup>[49]</sup> Several groups proved that for small deflections the force, acting on a pillar, generated by cells, really depends linearly on the deflection.<sup>[68-70]</sup> The exact values for the pillar radius  $r$  and length  $L$  can

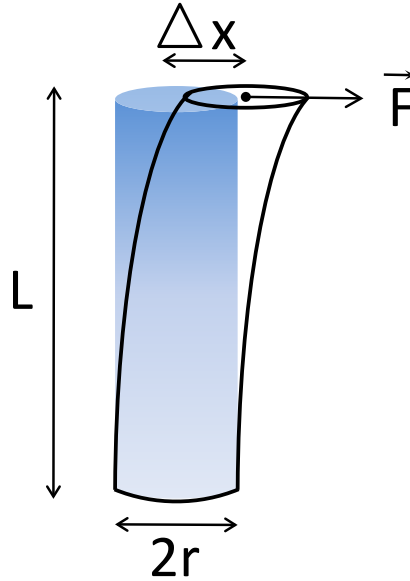


**Figure 3.6:** Schematic view of bending of a single pillar. A forces  $\vec{F}$  applied laterally to the pillar tops can bend the pillar. At known pillar length  $L$ , radius  $r$  and elastic modulus  $E$  of the material the spring constant  $k$  can be calculated from equation 3.2. Then, by measuring the displacement  $\Delta x$  the exerted force can be calculated.

be measured by electron micrographs. They have to be determined only once for substrates produced on the same master whereas the Young's modulus  $E$  for the

PDMS has to be measured before every experiment, since it can vary in ranges of several MPa. This is due to the uncertainty of the production parameters for the PDMS.

A convenient and easy method to derive  $E$  was described by Pelham *et al.*<sup>[1]</sup>: A rectangular piece of PDMS hangs down from a freely suspended anchor. After measuring the length  $l_0$  and the cross-section  $A$  of the PDMS beam a force  $F$  is applied by hanging a weight at the lower end of the PDMS. The elongation  $\Delta l$  is measured and the Youngs modulus  $E$  can therefore be calculated by

$$E = \frac{F l_0}{A \Delta l} \quad (3.3)$$

In this context it should be mentioned that this formula is only valid when the material, which is deformed by the applied strain, gets back to its original shape.<sup>[49]</sup>

To measure the deflection of the pillars during the cell experiments, bright field images of the the deflected pillars were recorded at different time points, and then related to images of two undeflected pillars. The centers of the pillars were detected by a home-written program in MATLAB by using tracking routines developed by J.C. Crocker and D. Grier<sup>[71]</sup>, originally written in IDL and transferred to MATLAB code by D. Blair and E. Dufresne. (Download: <http://physics.georgetown.edu/matlab/>). After image processing, to reduce background signals, a two dimensional gaussian profile was fitted to the images. Since the pillar heads were imaged in brightfield, this allowed the localization of the pillar centers in subpixel resolution.

## 3.2 Cell Culture

Establishment and serial cultivation of IHGK has been reviewed recently.<sup>[72]</sup> To avoid medium derived induction of keratinocyte differentiation, IHGK were maintained in low calcium keratinocyte growth medium (basal keratinocyte medium, KGM, with provided supplements, Promocell, Heidelberg, Germany) containing 50  $\mu\text{g}/\text{ml}$  kanamycin (Roche Diagnostics, Mannheim, Germany). After detaching the cells with trypsin, they were centrifuged, counted and calibrated in KGM to a cell density of  $1 \times 10^5$  IHGK/ $\text{cm}^2$ . Then, the cells were seeded on the FN-coated pillar surfaces for 24 hours.

Vitality of the cell was indicated by clear incorporation of neutral red (Sigma-Aldrich

GmbH, München, Germany) into the cells plasmamembrane. In contrast, a faint trypanblue (Sigma-Aldrich GmbH, München, Germany) stain reinforced cell vitality, since an intensive stain normally demarcates seriously damaged or dead cells. The staining was visualized by light microscopy using a Leica microscope (Leica DMRE microscope, Leica Microsystems, Inc., Bannockburn, IL). In preliminary experiments, IHGK attachment on micropillar arrays was tested 24 hours after cell seeding. Therefore, non-attached cells were determined by trypanblue staining using a Neubauer counting chamber. Calculation of non-attached cells from 5 individual cultures revealed an adhesion rate of nearly 100 %.

GCTFs were cultured in Dulbeccos Modified Eagles medium (DMEM) (PAA, Pasching, Austria) containing 10 % foetal calf serum (Seromed, Biochrom, Berlin, Germany) for routine cell culture.

### 3.3 Generation of Co-Cultures (CCs)

To investigate co-cultures of IHGKs and GCTFs *in vitro* on biofunctionalized micropillar interfaces a co-culture system was developed to explicitly study the role of GCTFs for keratinocyte differentiation (Fig. 3.7).

The gingival connective-tissue fibroblasts (GCTFs) calibrated to a cell number of  $1 \times 10^5$  cells per ml were precultured on the FN-coated pillar surfaces (Fig. 3.7 (A)) for 24 h in FAD medium (Hams F12/DMEM: mixing ratio 1:3, Biochrom, Berlin, Germany) including 5% foetal calf serum (FCS) and additionally containing cholera toxin (8.33 mg/ml), hydrocortisone (0.4 mg/ml), epidermal growth factor (EGF) (0.01 mg/ml), and insulin (5 mg/ml) (all additives: Promocell, Heidelberg, Germany) (Fig. 3.7 (B)). To mimic the *in vivo* situation, which was characterized by spatially separated growth of connective-tissue fibroblasts and keratinocytes, a collagen type-I cell-culture matrix with a thickness of about 1 mm and an extension equal to the size of the pillar array (about  $64 \text{ mm}^2$ ) was carefully placed on the pillar tops. The collagen lattice was generated from a collagen type-I solution (4 mg/ml) (Curacyte, Leipzig, Germany) containing FCS and Hanks buffered salt solution (10 $\times$ ), and the whole mixture was polymerized at 37°C. Then, immortalized human gingival keratinocytes (IHGKs) were seeded on the collagen-lattice surface at a density of  $1 \times 10^5$  cells per ml and co-cultured for 7 days and 14 days (Fig. 3.7 (C))

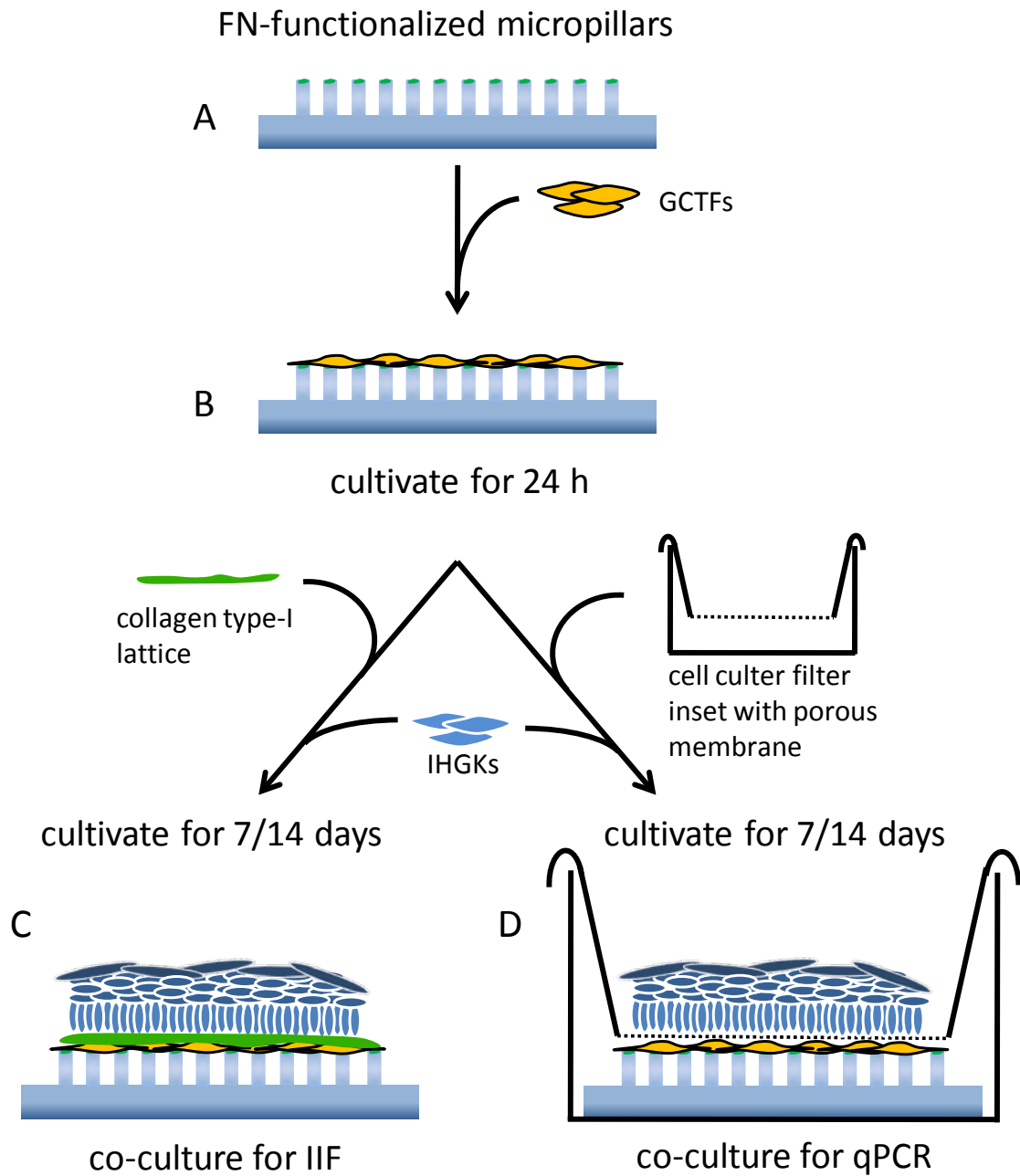


**Figure 3.7:** Schematic of the steps necessary to establish the co-cultures system. GCTFs are seeded on FN-functionalized pillars (A) for 24 h (B). Then for IIF a collagen type-I lattice (C) and a trans-well filter inset for qPCR (D) is placed on the GCTFs. Thereafter IHGKs are cultured for 7 and 14 days respectively.

for investigations by indirect immunofluorescence. For qPCR-experiments a trans-well filter inset (Greiner Bio-one, Frickenhausen, Germany) instead of the collagen lattice was used in order to isolate selectively the RNA from both cell types, devoid of cell-type cross contamination (Fig. 3.7 (D)).

For the control, IHGKs were seeded as described previously on 3 pillar arrays covered with the collagen lattice and on the trans-well system respectively that were devoid of GCTFs. For optimal reproducibility at the announced periods of one and two weeks, three CCs of GCTFs and IHGKs were maintained in FAD medium.

All of the cell-culture experiments were conducted under standard cell-culture conditions: 37°C, 97% humidity and 5% CO<sub>2</sub>.

To isolate selectively the RNA from both cell types, devoid of cell-type cross contamination, additionally a trans-well filter insert (Greiner Bio-one, Frickenhausen, Germany) was used. The IHGKs were seeded on the porous membrane as described above (Fig. 3.7 (B)). Empirically, these cultivation times had been known from our previous co-culture studies using conventional non-defined collagen type-I microenvironments to successively yield satisfactory epithelial morphogenesis. This was essentially based on two features provided by the co-culture device using collagen lattices. Firstly, both cell types grew in a spatially separated manner. Secondly, due to this spatial separation, the interactions between the epithelial keratinocytes and the connective-tissue fibroblasts resembled that under *in vivo* conditions.<sup>[73–75]</sup>

## 3.4 Indirect Immunofluorescence (IIF) of IHGKs on Micropillars

### 3.4.1 IHGKs on Micropillars

IHGKs were cultivated on micropillar interfaces for 24 h. In brief, after air drying, specimens were fixed in 80% methanol and in acetone (5 min. each, 4°C) and incubated with primary antibody overnight at 4°C following protocols described previously.<sup>[76]</sup>

Goat polyclonal anti-human K1, K10 (Santa Cruz Biotechnology Inc., Santa Cruz, CA, USA) or rabbit monoclonal anti-human FAK (Biomol, Hamburg) antibodies were adjusted to a final working dilution of 1:50. The samples were washed 3 times in

phosphate-buffered saline (PBS) (containing 0.01% TWEEN 20 (Sigma, München, Germany) and 12% bovine serum albumin (BSA) (Serva, Heidelberg, Germany) (PBT)) for 5 min and incubated with secondary fluorochrome-conjugated antibody (1:100; Alexa Fluor<sup>®</sup>, MoBiTec GmbH, Göttingen, Germany) for 1 h at RT.

To allow for total nuclei staining, propidium iodide (Sigma-Aldrich GmbH, München, Germany; 10 µg/ml) was added to the secondary antibody. Specimens were embedded in mounting medium (Vectashield, Vector Laboratories Inc., Burlingame, CA, USA) and documented by a confocal laser scanning microscope (Leica TCS/NTCLSM microscope, Leica Microsystems, Inc., Bannockburn, IL; or Zeiss LSM Pascal 5, Zeiss, Oberkochen). To test the specificity of the immunostaining, negative controls were run with the secondary antibodies alone.

### 3.4.2 GCTFs on Micropillars

The IHGK-epithelial equivalents, derived from co-cultures (CCs), were carefully removed from the pillar surface. The working parameters were the same as in the previous section only the antibodies used differed. Mabs directed against human vimentin (Acris, Hiddenhausen, Germany) and collagen type-I (Biodesign International, Saco, Maine, United States) were adjusted to a final working dilution of 1:20 in PBS. Thereafter secondary fluorochrome-conjugated antibody (Alexa Fluor 488<sup>®</sup>, MoBiTec GmbH, Göttingen, Germany, wd=1:50) was added. The nucleus are again counterstained with propidium iodide. Generally, the specificity of the employed primary antibodies was proven by only incubating the secondary antibody, which yield no specific fluorescence signal.

### 3.4.3 IHGK Co-Cultures on Micropillars

If not mentioned the parameters were the same as in the previous sections. As above, the IHGK-epithelial equivalents derived from CCs and controls were carefully removed from the pillar surface, embedded in TissueTek (Sakura, Zoeterwoude, Netherlands), and frozen in liquid-nitrogen vapour. Then, 10 mm of frozen sections of the CC and control specimens were mounted on adhesive slides (Histobond, Marienfeld, Germany), followed by fixation in ice-cold, 80% methanol and acetone (5 min each). Thereafter, the frozen sections were incubated overnight with the primary antibodies directed against keratin K1/10 (mouse monoclonal/ mab,

Acris, Hiddenhausen, Germany, working dilution (wd)=1:50). Then, the slides were washed in PBS three times (5 min each), followed by incubation with the secondary fluorochrome-conjugated antibody for K1/10 (Alexa Fluor 488<sup>®</sup>, MoBiTec Göttingen, Germany; IgG (HL) goat anti-mouse, wd=1:50) for 1 h at room temperature. Nuclei were again counterstained with propidium iodide. Finally, the frozen sections were embedded in a mounting medium (Biomedica; Foster City; CA; United States).

## 3.5 RNA Extraction and Quantitative Real-time PCR Analysis

### 3.5.1 IHGKs on Micropillars

Total RNA was extracted of about  $1 \times 10^5$  IHGKs on micropillar arrays using the RNeasy mini kit (Qiagen, Hilden, Germany). RNA concentration and integrity were determined by measuring total RNA with an automated electrophoresis system (Experion<sup>TM</sup> BioRad, München, Germany). First-strand cDNA was synthesized from 1 µg total RNA aliquot in reaction mixture containing random hexamer primer by performing the RevertAid reverse transcription protocol (Fermentas Inc., Hanover, MD, USA). The cDNA concentration was determined by fluorometry using a fluorescent dye (PicoGreen; Molecular Probes) and adjusted to 1ng/µl.

Gene-specific PCRs were performed with equal amounts of cDNA (1ng) in a total volume of 30 µl with the following keratin 1 (K1) primers, designed with Beacon Designer 5.0 Software, (BioRad Laboratories, Philadelphia, PA, USA): sense-3'-CCTTACTCTACCTTGCTCCTAC-5', antisense-3'-GCCACCACCACCATAACC-5'. In particular, after a general denaturation step at 95°C for 15 min with Hot-StarTaq DNA Polymerase (Qiagen, Hilden, Germany), denaturing was carried out at 94°C for 1 min. The annealing temperature was 56°C for 1 min, and elongation was performed at 72°C for 1 min. After amplification, 5 µl of each reaction was loaded onto a 2% agarose gel containing ethidium bromide (0.5 µg/ml), which was photographed by using a CCD camera (Casio Europe GmbH, Norderstedt, Germany). The relative mRNA transcription of K1 was determined by measuring of different gel band intensities. The relative densities were obtained by using NIH Image program 1.37h. Each RT-PCR experiment was run three times, based on cell cultures of independent cultivated immortalized human gingival keratinocytes (IGHK) from

passages 98-110.

qPCR analysis was performed with the iCycler Real-Time PCR Detection System (BioRad Laboratories, Philadelphia, PA, USA) according to the manufacturer's instructions. A commercially designed primer pair has been used (RT2 PCR Primer Set for Human KRT1, Superarray, Frederick, MD, USA). The standard temperature profile included initial denaturation for 15 min. at 95°C, followed by 40 cycles of denaturation at 94°C for 40 s, annealing at 55°C (primer-dependent) for 30 s, and extension at 72°C for 40 s. The results of the qPCR were analyzed as relative expression levels of IHGKs on the micropillar interfaces at different pillar head interspaces and in relation to a predefined control pillar array of 14  $\mu\text{m}$ . The relative expression levels of each mRNA were analyzed using a modification of the  $\Delta\Delta C_T$  equation, which allowed counting for differences in efficiencies ( $E = 10^{-1/\text{slope}}$ ) between the PCR reactions.<sup>[77]</sup> The data was calculated using the software Gene Expression Macro provided with the iCycler and normalized to the  $C_T$  of the unmodulated housekeeping gene (HKG)  $\beta$ -actin.

### 3.5.2 GCTFs and Epithelial Equivalents

The epithelial equivalents of the co-cultures and controls, and the pillar arrays with GCTFs were maintained in the above-mentioned trans-well system. After the respective culture periods, of one and two weeks, the total RNA was isolated selectively from both cell types using the RNeasy mini kit (Qiagen, Hilden, Germany). The specimens-derived RNA integrity and concentration was determined as described previously and the derived cDNA was adjusted to 1 ng/ml. qPCR analysis for the IHGKS was performed as described above whereas for GCTFs the PCR was performed with self-designed primers (BeaconDesigner 5.0 Software, BioRad Laboratories, Philadelphia, PA, USA), for collagen type-I (forward: 5'-CGGAGGAGAGT CAGGAAGG- 3'; reverse 5'-ACATCAAGACA AGAACGAGGTAG-3') and vimentin (forward: 50-TTTTTCCAGCAAGTATCCAACC-3', reverse: 5'-GTTTTCCAAAG ATTTATTGAA-3', Thermo Fisher Scientific, Germany). The data obtained for both cell types was normalized to the  $C_T$  of the glyceraldehyd-3-phosphat-dehydrogenase (GAPDH) non-modulated housekeeping gene.

## 3.6 Scanning Electron Microscopy (SEM)

The IHGKs and GCTFs were fixed with 4% glutaraldehyde in PBS for 1 h and rinsed 3 times with PBS buffer after the respective culture periods on the micropillar surfaces. Then, the specimens were dehydrated by rinsing through graded ethanol/water mixtures (50%, 70%, 80%, 90% and 100%; each step for 10 min at RT). Thereafter, ethanol was slowly exchanged by liquid CO<sub>2</sub> (critical point dryer; Balzers CPD, Balters Union, Liechtenstein). Finally, the samples were dried using the critical point method<sup>[78]</sup> and then sputtered with a thin layer of gold (sputter coater, Balzers SLD; Balzers Union, Liechtenstein), of approximately 10 nm in thickness. The electron micrographs were obtained by an Amray 1845 (Amray) or a Leo Gemini 1530 (Zeiss, Oberkochen) scanning electron microscope.

## Early Keratinocyte Differentiation on Micropillar Interfaces

Epithelial tissue in general and the gingiva in detail must exhibit an extended mechanical integrity. The epithelial cells, namely keratinocytes in the gingiva, overcome this challenge being tightly attached to each other and express intermediate filaments (IFs). Since IFs are known to be extensively stress resistant, but even more flexible than the two other protein polymers actin and the microtubules, they provide an ideal mechanical support for these cells.<sup>[60]</sup> Among the 6 families of IFs that are known, the cytokeratins are the hallmark among the IFs for epithelial differentiation.

In addition to proliferation, differentiation is a key cell function of keratinocytes to achieve and maintain epithelial tissue integrity, i.e., tissue homeostasis.<sup>[79]</sup> In squamous epithelia, differentiation occurs during keratinocyte migration from the basal to the suprabasal and apical epithelial cell layers, including morphological and biochemical changes. The biochemical changes are reflected by the synthesis of certain molecules indicating early and terminal stages of differentiation. While basal keratinocytes express keratin K5 and K14, they immediately downregulate their expression once they enter the differentiation pathway and upregulate the genes for K1 and K10. Therefore the expression of K1 and K10 characterize early differentiation stages in keratinized epithelia<sup>[80]</sup>, while the expression of K1 precedes that of K10 during differentiation.<sup>[81]</sup> Involucrin and filaggrin, in contrast, can be considered as markers of terminal differentiation.<sup>[82,83]</sup> The keratin gene family comprises 30 members and can be divided into 2 subfamilies, the more acidic type I and the more

basic type II cytokeratins according to their migration in electrophoresis. Whereas K1 belongs to the type II subfamily, K10 is a type I keratin.

For epithelial homeostasis, the adhesion of keratinocytes to extracellular matrix molecules is indispensable. Parts of the epithelial keratinocyte matrix form the epithelial basement membrane, while matrix constituents such as fibronectin (FN) are ubiquitously found in epithelial and connective tissue.

To provide a support that can give insight to the influence of substrates with defined mechanical properties and morphology on keratinocyte differentiation, above described biofunctionalized micropillar arrays were used. Immortalized human gingiva keratinocytes (IHGKs) were cultured on these micropillar arrays.

To minimize the influences of the presented microenvironment for the cells and to facilitate the interpretation of the obtained data, the diameter and the height of the pillars were kept constant at 5  $\mu\text{m}$  and 15  $\mu\text{m}$  respectively. Whereas four different interpillar distances were chosen for the experiments: 5  $\mu\text{m}$ , 8  $\mu\text{m}$ , 11  $\mu\text{m}$  and 14  $\mu\text{m}$ . Thus, the first step to investigate keratinocyte differentiation on different substrates *in vitro* was to check the adhesion and vitality of the cultured cells which will be presented in the first section of this chapter, followed by the investigation on the morphology of IHGKs and on the expression of early keratinocyte differentiation markers, keratin 1 and 10 (K1/10), on substrates with different pillar distances in the second part.

## 4.1 Creation of an *in vitro* Model Surface for IHGKs

The structure of a fabricated PDMS-micropillar field with an interpillar distance of 8  $\mu\text{m}$  is shown in Fig. 4.1 from a lateral perspective and from the top. The pillars were regularly distributed over the whole field and had a cylindrical shape.

To create a biomimetic model surface which is closer to the *in vivo* situation the pillar tops were functionalized with fibronectin (FN) as explained in chapter 3.1.2. As mentioned above FN is a ubiquitous found protein of the ECM and is present everywhere in epithelial and connective tissue. FN facilitates the adhesion of the keratinocytes to the pillar tops. This adhesion is necessary for all cells of solid tissue for entering a cell cycle and later the synthesis of cell- and tissue-specific differentiation products.<sup>[84]</sup>

The cells were seeded at a constant cell number of  $1 \times 10^5$  IHGK/cm<sup>2</sup> on the micropil-

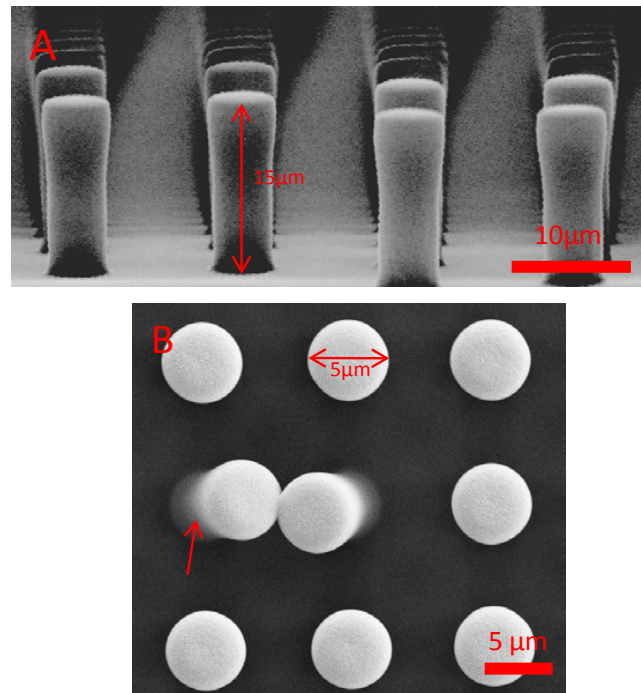


**Figure 4.1:** SEM images of a single micropillars from a lateral perspective (A) indicating a height of 15  $\mu\text{m}$  for the pillars. (B) shows a regular field of 5  $\mu\text{m}$  in pillar diameter and interpillar distance. The red arrow confirms the regular shape of the pillars in lateral direction. Image (A) is modified from [58].

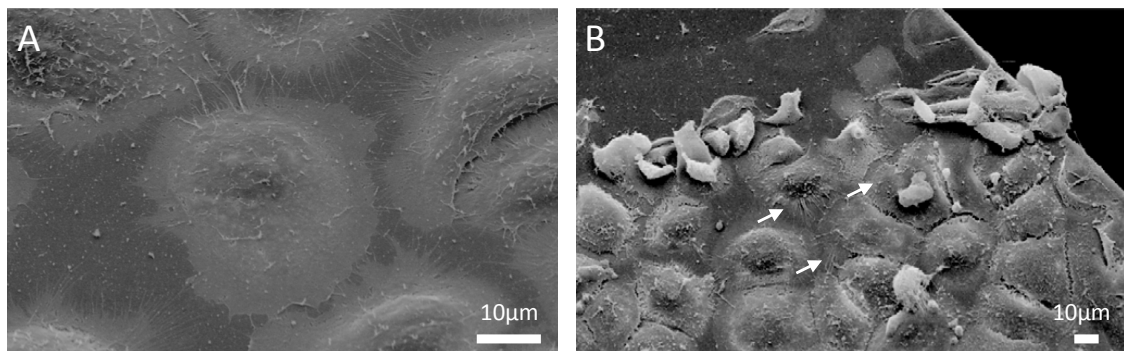


**Figure 4.2:** Scanning electron micrographs of IHGKs cultured on FN-coated glass. Single IHGKs are properly adhered on the glass surface (A) and form a nearly confluent cell layer (B). The cell-to-cell interconnections are marked by arrows. Scale bars are 10  $\mu\text{m}$ . Images are modified from [58].

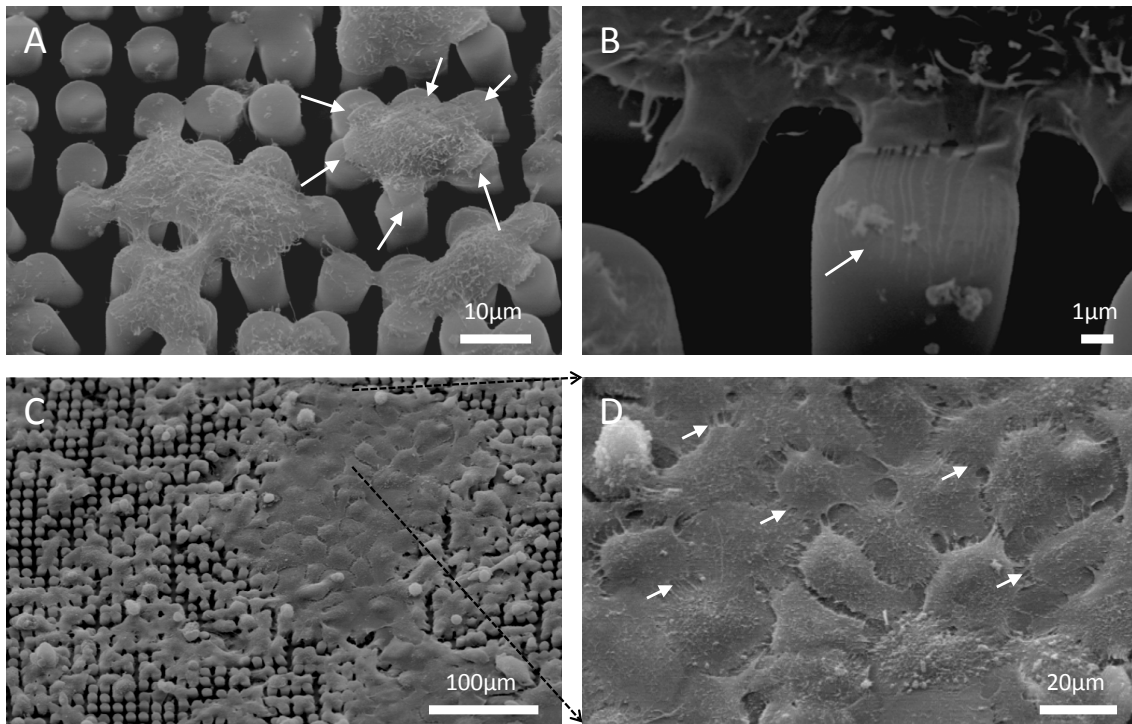


**Figure 4.3:** SEM images of IHGKs cultured on FN-coated micropillar arrays with an interpillar distance of  $8\ \mu\text{m}$ . (A) shows single keratinocytes attached to several pillars (arrows). The arrows mark the attachment sites of a single cell. The scale bar is  $10\ \mu\text{m}$ . Adhesive structures are formed on the pillar tops (white arrow in B). Scale bar corresponds to  $1\ \mu\text{m}$ . The IHGKs even form islands with cell-cell interconnections (C) (scale bar  $100\ \mu\text{m}$ ) which are marked with arrows in (D). The scale bar corresponds to  $20\ \mu\text{m}$ . Image is modified from<sup>[58]</sup>.

lar interfaces in the presence of low calcium medium to prevent calcium-dependent induction of early keratinocyte differentiation. <sup>[85,86]</sup>

To achieve proper cell adhesion on the micropillar surfaces, the IHGKs were cultured for 24 h on the substrates, based on the experience obtained from plastic culture dishes. The cells were also seeded on FN-coated glass and observed by electron microscopy (Fig. 4.2 (A)). After 24 h the cells were well spread (Fig. 4.2 (B)) and formed island of interconnected cells.

This finding was compared to IHGKs cultured on FN-functionalized micropillars (Fig. 4.3). A single fully spread IHGK occupied six up to eight pillars on a substrate with an interpillar distance of  $8\ \mu\text{m}$  (Fig. 4.3 (A)), and formed adhesive structures on the pillar tops (Fig. 4.3 (B)). The formation of such structures clearly contacting the pillars proved the true adhesion of the keratinocytes. Furthermore they formed

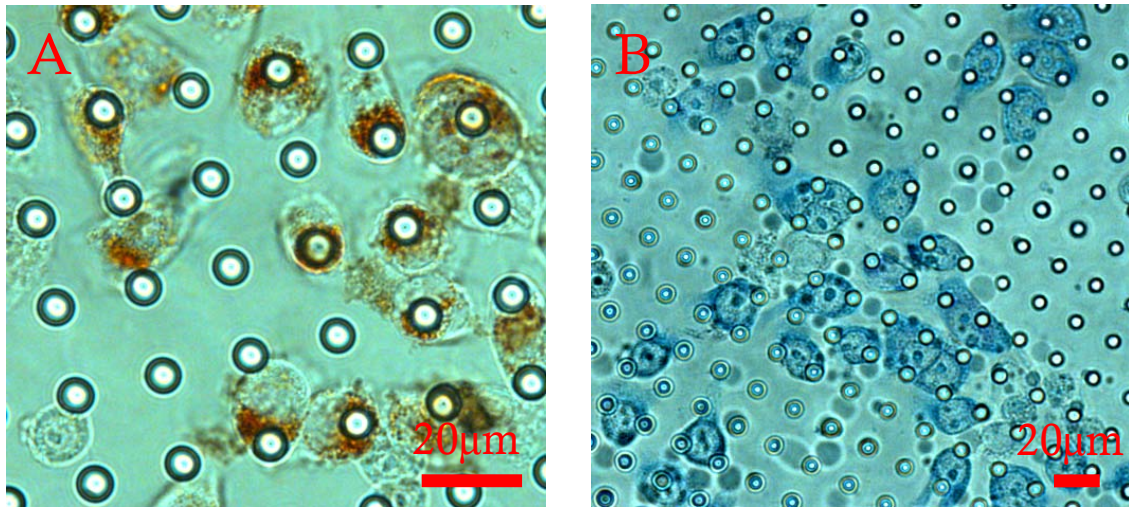


**Figure 4.4:** Light microscopy of IHGK viability analysis on micropillars with interspaces of  $8\ \mu\text{m}$ . Cell membrane bound neutral-red staining indicates living cells (A) while only trypanblue staining reinforces cell viability (B). Scale bars are  $20\ \mu\text{m}$ . Images are adapted from [58].

small islands of interconnected cells (Fig. 4.3 (C) and (D)) and were comparable to the situation found on glass (Fig. 4.2 (B)). This was remarkable, because the ability of IHGKs to aggregate in such islands is also present *in vivo*, where the epithelial is characterized by interconnected cells, arranged in layers.

The adhesion rate was approximately 100 % for seeded IHGKs on micropillar arrays like the ones shown above. The cell viability was proven by neutral-red (Fig. 4.4 (A)) and trypanblue staining (Fig. 4.4 (B)). Neutral red incorporates into the cells' plasma membrane while intensive trypanblue staining is a signal for seriously damaged or dead cells. Both showed a satisfactory cell viability and proved the practicability for the fabricated microstructured surfaces for *in vitro* experiments with IHGKs.

#### 4.1.1 Traction Forces exerted by Keratinocytes on Micropillar Fields.

The PDMS is a flexible substrate with a Young's modulus of 1-10 MPa. The fabricated micropillars can act as single defined springs (see chapter 3.1.3). As mentioned previously, the adhered cells can feel the stiffness of their environment and in a feedback loop produce forces themselves. While growing on the microstructured surfaces, bending of the pillars could be observed due to the traction of the keratinocytes (Fig. 4.5). The deflection of a single pillar was measured as described in

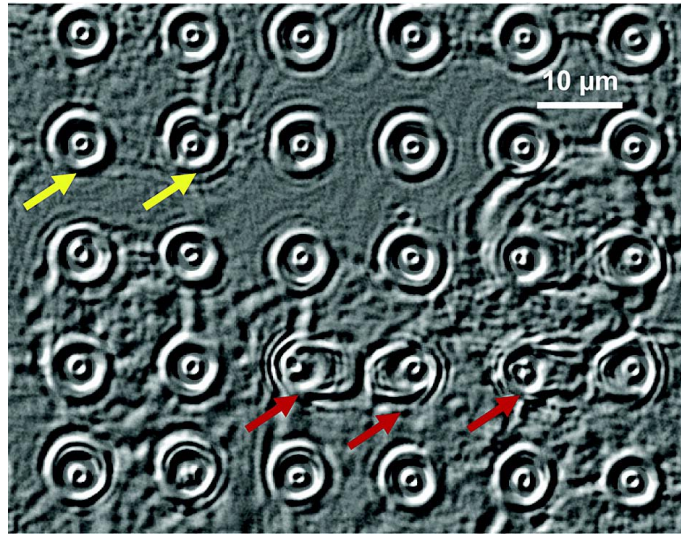


**Figure 4.5:** Bright-field live cell image of single IHGK on a FN-coated micropillar array with an interpillar distance of  $8\ \mu\text{m}$ . It can be distinguished between pillars which are deflected by a cell (red arrows) and non-deflected pillars (yellow arrows). Bar corresponds to  $10\ \mu\text{m}$ . The image is processed with a Laplacian gradient filter to enhance the visibility of the structures. Image is adapted from [58].

chapter 3.1.3. To allow an approximation of the forces directed from the pillars to the IHGKs, the cells were cultured on an FN-coated pillar array with an obstacle distance of  $8\ \mu\text{m}$ . The Young's modulus of the substrate was measured to  $6.5\ \text{MPa}$  by the method described in chapter 3.1.3. The spring constant  $k$  for a single pillar with  $5\ \mu\text{m}$  in diameter and  $15\ \mu\text{m}$  in height was calculated according to equation 3.2 to  $k=170\ \text{nN}/\mu\text{m}$ . Insertion of  $k$  in equation 3.1 revealed forces exerted by the keratinocytes to a single pillar up to be around  $110\ \text{nN}/\text{Pillar}$ .

The effects of environmental changes with respect to the morphology and expression of the early differentiation markers will be presented in the following chapter.

## 4.2 Keratinocyte Morphology and Expression of K1 and K10 on Microstructured Surfaces

### 4.2.1 Morphology

After successfully achieved keratinocyte adhesion and viability on the micropillar interfaces, the interpillar distances were varied. While keratinocytes, cultured on FN-coated pillars with interpillar distances of 8  $\mu\text{m}$  (Fig. 4.3) and 5  $\mu\text{m}$  (Fig. 4.6 (A)), covered the pillar tops and were quite flat and round-shaped, the cells already penetrated into the micropillar field on substrates with distances of 11  $\mu\text{m}$  (Fig. 4.6 (B)). They had a more linear or triangular shape depending on how many pillars they covered. To exclude drying artifacts from the sample preparation for the electron microscopy and to ensure successful adhesion of the keratinocytes, they were stained by IIF for the focal adhesion kinase (FAK), a protein which is expressed in the cytoplasm during adhesion (Fig. 4.6 (C) and (D)). The obtained results confirmed the morphological differences.

The strain energy  $u(i)$  for each post under a cell can be calculated by

$$u(i) = \frac{1}{2}k\delta(i)^2 \quad (4.1)$$

where  $\delta(i)$  is the displacement of the  $i^{\text{th}}$  post. Recent observations showed that the strain energy per cell, which was found by summing up  $u(i)$ , was nearly independent from the post geometry conformation.<sup>[69]</sup> That leads to the suggestion, that the morphology differences resulted from the lack of adhesion sites for the keratinocytes on substrates with higher interpillar distances.

To determine the lateral position for the cultured keratinocytes in Fig. 4.6 (C) and (D), optical cuts in lateral direction of the above mentioned cells were performed, using laser scanning microscopy (LSM 5 Pacal, Zeiss).

Typical examples of these cells are shown in Fig. 4.7 and 4.8. On the substrate with an interpillar distance of 5  $\mu\text{m}$  the keratinocytes were nearly round shaped and covered the pillar tops (Fig. 4.7 (A) and (B), arrows). They only penetrated slightly into the micropillar field. The FAK was again stained in green with a counterstain of

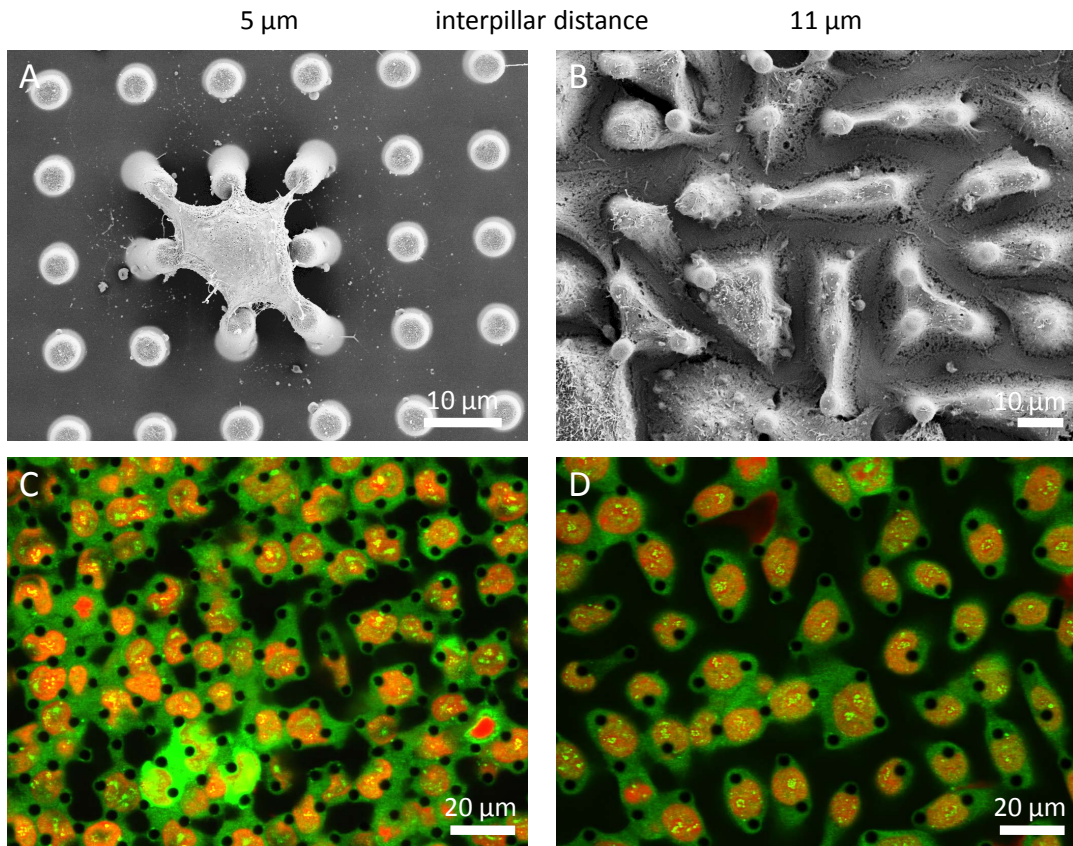


**Figure 4.6:** Morphology differences of IHGKs on pillar fields with interpillar distances of  $5\ \mu\text{m}$  (A, C) and  $11\ \mu\text{m}$  ((B), (D)): SEM-pictures of (A) a keratinocyte spread on a FN-coated pillar field. The cell adheres to the pillar tops and is spread over 8 pillars while the keratinocytes in (B) sink into the substrate and are more triangle shaped. Scale bars correspond to  $10\ \mu\text{m}$ . Fluorescent images of the cells stained for FAK (green) by IIF ((C), (D)) reveal the same morphological differences. The cell nuclei were counterstained by propidium iodide (PI) in red. Scale bars are  $20\ \mu\text{m}$ .

the cell nuclei by PI in red. Projection of the optical cuts made in Fig. 4.7 (A) on the  $zx$ -axis and the  $zy$ -axis (Fig. 4.7 (B)) revealed a flattening of the cells. These observations become even more obvious by a three dimensional reconstruction (4DInside plugin, Axiviosion software, Zeiss, Oberkochen) of the optical cuts (Fig. 4.7 (C-D1)).

A different morphology was observed for cells cultured on substrates with an interpillar distance  $11\ \mu\text{m}$  (Fig. 4.8). The cells were more linear shaped (Fig. 4.8 (A) and (B)) and penetrated almost completely into the micropillar field. They grew around the obstacles (arrow in the  $zy$ -projection in Fig. 4.8 (B)). Again the optical cuts of the observed keratinocyte were three-dimensional reconstructed, which confirmed

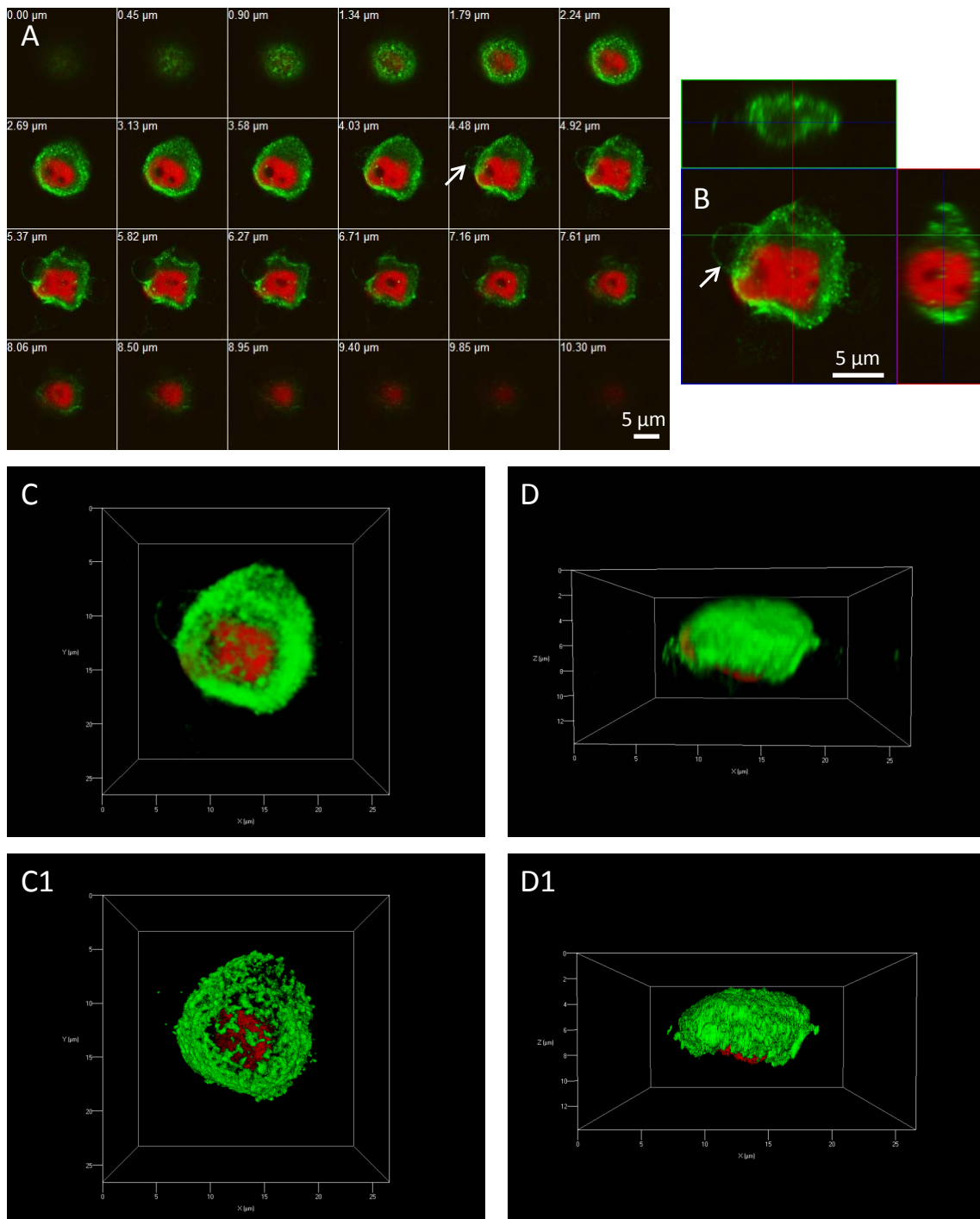


**Figure 4.7:** Optical cuts and 3D reconstruction of an IHGK on a 5 $\mu\text{m}$  substrate. The optical cuts of an IHGK (A) show the keratinocyte lying above the micropillars attached to the pillar tops (see white arrows in (A) and (B)). Green fluorescence reveals the FAK staining whereas the nucleus is counterstained by PI (red). The cell is nearly round-shaped and  $zx$ - and  $zy$ -projection in (B) reveals a flattening of the cell. By three dimensional reconstruction these findings are confirmed. (C) shows the cell from a top and (D) from a lateral view. (C1) and (D1) represent a surface reconstruction of the fluorescence of (C) and (D) respectively. Scale bars in (A) and (B) correspond to 5  $\mu\text{m}$ .

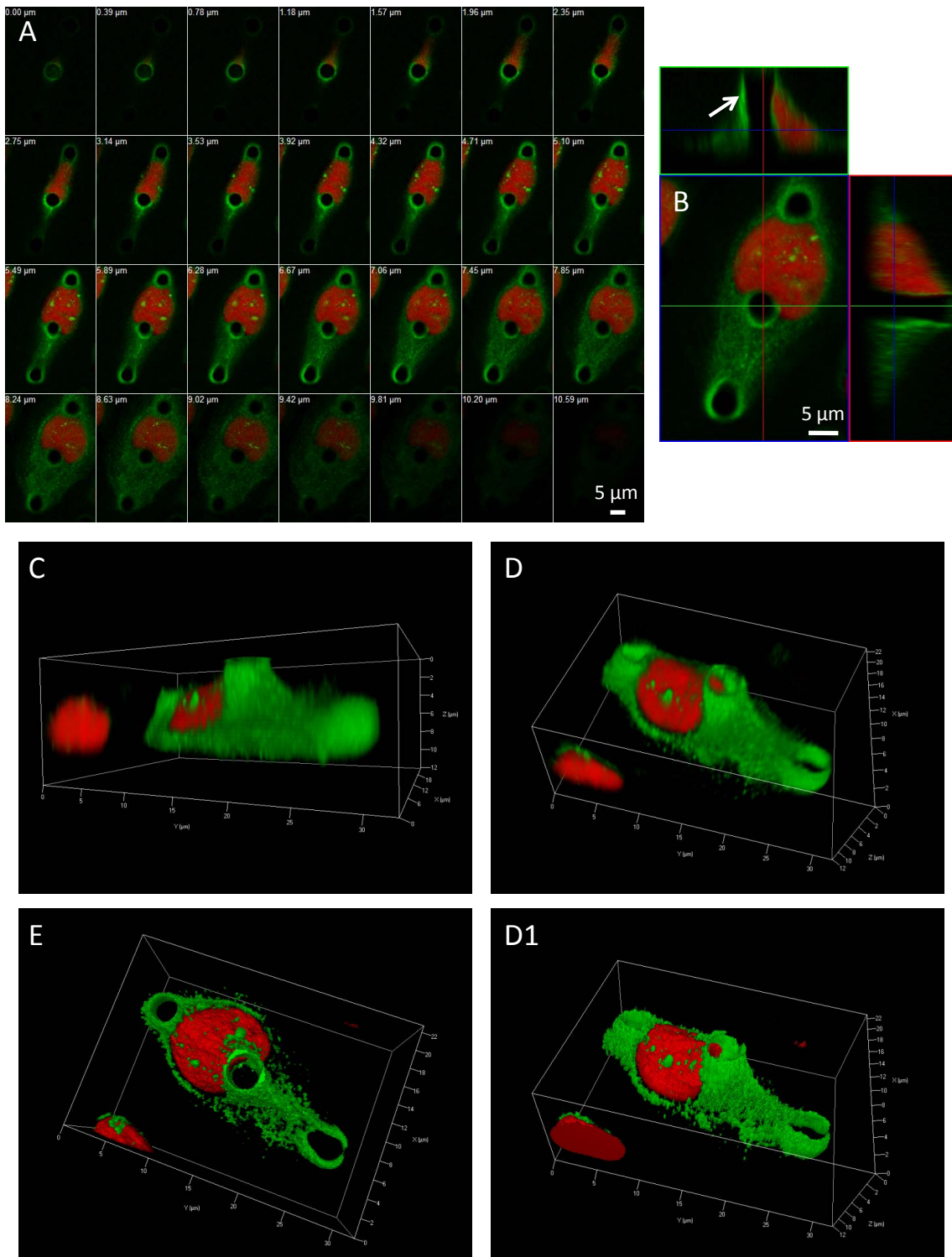


**Figure 4.8:** Optical cuts and 3D reconstruction of an IHGK on a  $11\mu\text{m}$  substrate. Again the keratinocyte is stained for FAK (green) and its cell nucleus with PI (red). The optical cuts of an IHGK (A) show the keratinocyte penetrating into micropillars attached to the pillar tops. It is more linear shaped and  $zx$ - and  $zy$ -projection in (B) point out the lateral position of the cell (FAK expressed around an obstacle marked by white arrow). By three dimensional reconstruction these findings are confirmed. (C) shows the cell from a lateral view (D) from an angular top view. (D1) and (E) represent a surface reconstruction of the fluorescence in (D) and a top view respectively. Scale bars in (A) and (B) correspond to  $5\mu\text{m}$ .

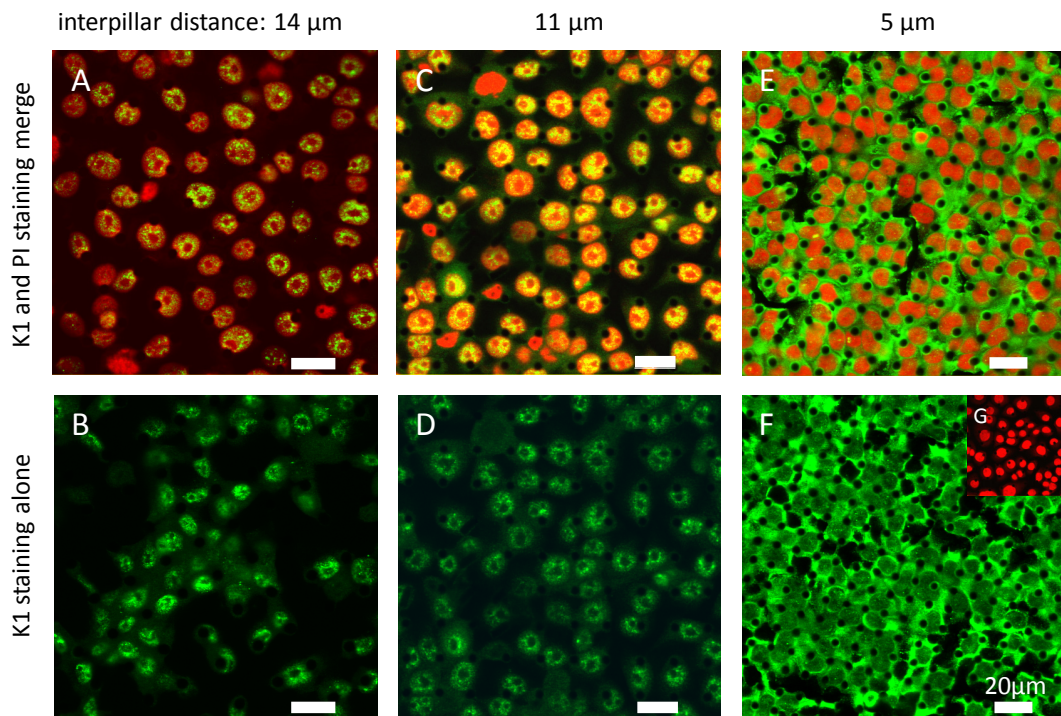


**Figure 4.9:** Fluorescence images of IHGKs illustrating the early differentiation marker K1 by IIF on substrates with different interpillar distances. The green fluorescence demarcates the K1 while the nuclei are stained by PI and appear in red. A granular, nucleus-associated pattern for K1 on a micropillar array of  $14\ \mu\text{m}$  pillar distance can be seen in the merged image (A), (B) shows the same motif with the K1 green fluorescence signal only, to better discriminate the nucleus-associated pattern. At an interpillar distance of  $11\ \mu\text{m}$  the cytoplasmic K1 distribution increases (C), (D) indicates again the K1 green fluorescence signal only. On the smallest interpillar distances of  $8\ \mu\text{m}$  the cytoplasmic K1 distribution is most extended (E), which becomes even clearer without the red PI counterstain signal (F). The authenticity of cytoplasmic K1 extension is proven by the absence of green fluorescence following incubation of respective pillar array specimens with secondary fluorochrome-coupled antibody alone (G). The PI counterstain demarcates again the cell nuclei. The scale bars correspond to  $20\ \mu\text{m}$ . Images are modified from [58].

the lateral position (Fig. 4.8 (C-E)).

These findings suggested that early keratinocyte differentiation also varies with respect to different interpillar distances which will be discussed in following.

### 4.2.2 Expression of K1/10

To evaluate early keratinocyte differentiation on the microstructures, pillars arranged in arrays with an interpillar distance of 14, 11 and 8  $\mu\text{m}$  were employed. The cultured IHGKs were investigated by IIF for the early differentiation marker keratin 1 (K1). On arrays with a large interpillar distance (Fig. 4.9 (A) and (A1)) the fluorescence signal of K1 showed a granular perinuclear pattern. With declining pillar distances K1 exhibited a progressive cytoplasmic protein distribution (Fig. 4.9 (B) and (B1)) and led to most extensive cytoplasmic distribution at 8  $\mu\text{m}$  (Fig. 4.9 (C) and (D)).

The intermediate filament K1 normally nucleates from an organizing center associated to the nucleus and distributes to the cytoplasm.<sup>[87]</sup> Thus, the cytoplasmic abundance of the keratin K1 protein can be considered as a biological correlate of the keratinocyte to fulfill its function in the epithelial context, which in our analysis is reflected by early differentiation. With respect to the IIF pattern found for K1 on the large-scale pattern of 14  $\mu\text{m}$ , the perinuclear fluorescence may reflect an initial stage in K1 filament formation starting from the above-mentioned nucleus-associated organizing center. Therefore, the most extended cytoplasmic K1 distribution observed in large cell areas on the lowest scale pattern of 8  $\mu\text{m}$  may suggest the progressive formation of K1 intermediate filaments in the cytoplasm. In addition, this cytoplasmic K1 extension demonstrated, that the 8  $\mu\text{m}$  pillar pattern rendered a favorable extracellular environment for early keratinocyte differentiation. While keratin K1 in IHGKs was abundant found in the cytoplasm after culturing on pillars with smaller distances for 24 h, IIF with a keratin 10 specific antibody only showed a granular nucleus-associated pattern. There was no difference in fluorescence signal visible between cells seeded on 14  $\mu\text{m}$  (Fig. 4.10 (A)) and on 8  $\mu\text{m}$  (Fig. 4.10 (B)) patterns. This observation was in accordance to already reported hints, that the expression of K10 in the early keratinocyte maturation stages may be delayed.<sup>[81]</sup>

While IIF revealed only qualitative data on differences of the expression of K1, polymerase chain reaction (PCR) was used to quantify modulations on the transcriptional level. This was done both semiquantitatively (sqPCR) and quantitatively (qPCR). A sqPCR only brought obtained gel band intensities in relation, while qPCR revealed quantitative protein expression relative to a predefined control.<sup>[77]</sup> With this method already small differences on the observed samples were

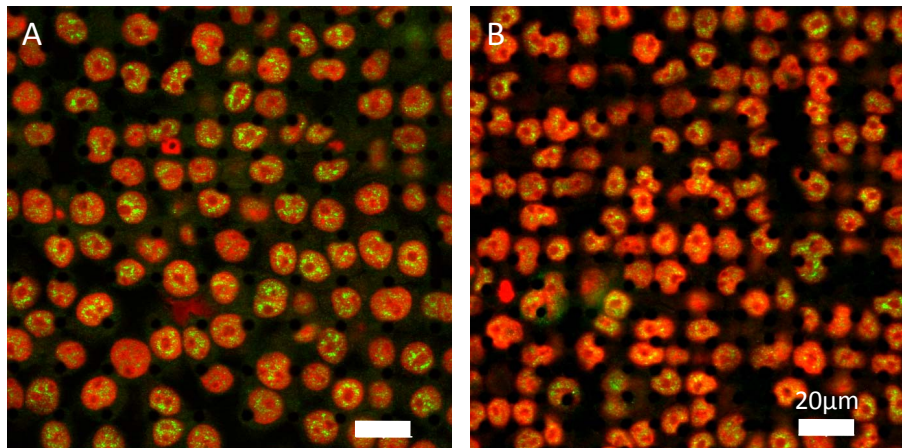


**Figure 4.10:** The intermediate-filament protein keratin 10 (K10) in the IHGKs is visualized by indirect immunofluorescence (IIF). The same nucleus-associated pattern for K10 is found for interpillar distances of 14  $\mu\text{m}$  (A) and 8  $\mu\text{m}$  (B). Bars correspond to 20  $\mu\text{m}$ . Images are adapted from<sup>[58]</sup>.

visualized.

Therefore, IHGKs were cultivated on the same pillar arrays for 24 h as used for the IIF. Thereafter RNA was extracted and amplified with the same amounts of cDNA (1 ng). Three independent experiments were performed (Fig. 4.11 (A)). The relative gel band intensities showed the trend, which was already expected from the IIF: Increasing interpillar distances from 8  $\mu\text{m}$ , to 11  $\mu\text{m}$  and finally to 14  $\mu\text{m}$  led to a decrease of transcription levels for keratin 1 (Fig. 4.11 (A)). This data showed that the most extended cytoplasmic distribution of the K1 protein, found for micropatterns with an interpillar distance of 8  $\mu\text{m}$ , corresponded to the highest K1 mRNA transcription levels found in the sqPCR.

These findings were even more confirmed by performing a qPCR. According to the values obtained from the sqPCR, the values of the cells cultured on interpillar distances of 14  $\mu\text{m}$  were set as the control. The trend to express more K1 at declining pillar distances was even more pronounced in the qPCR than in the sqPCR (Fig. 4.11 (B)). At a pillar distance of 11  $\mu\text{m}$  the relative expression level of K1 was 3.7 folds higher compared to the control, whereas the cells on pillars with an interpillar distance of 8  $\mu\text{m}$  even expressed K1 in a 5.5 fold value compared to cells of the control (Fig. 4.11 (B)).

The increased K1 expression transcription levels obtained for declining interpillar distances therefore reinforced the qualitative observations made by IIF of K1.

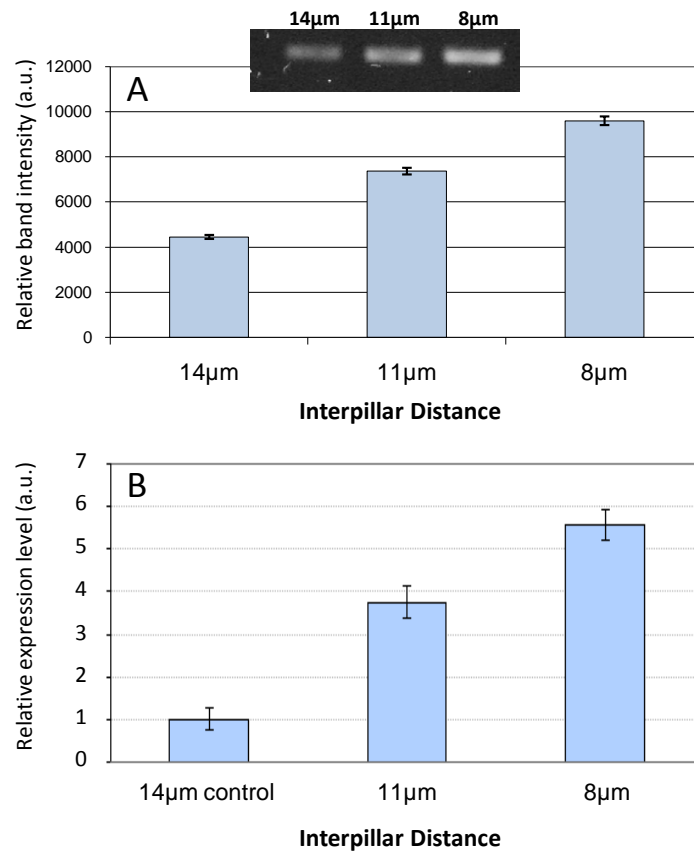


**Figure 4.11:** Expression profile of K1 in IHGKs, cultured on substrates with interpillar distances of 14, 11, and 8 μm, detected by semiquantitative (sqPCR) and quantitative RT-PCR (qPCR). The K1 mRNA transcription levels are compared by using equal amounts of cDNA. The observed gel bands for K1 (inset in A) show a decreasing relative band intensities for decreasing interpillar distances in the sqPCR (A). This correlates with the relative expression levels for K1 analyzed by qPCR (B). The expression levels are normalized to the  $C_T$  of the unmodulated housekeeping gene (HKG)  $\beta$ -actin and expression level for IHGKs on substrates with 14 μm interpillar distance are set as control. The data is analyzed as described in chapter 3.5.1. (MSD: n=3). Image is adapted from<sup>[58]</sup>.

Our coinciding observations strongly suggest, that there is a distance dependency on the early differentiation of human gingival keratinocytes in respect to anchorage points for cell adhesion created on the microstructures. Additionally this leads to the suggestion, that mechanical stimuli from the ECM have a feedback to early keratinocyte differentiation either on the protein and the transcriptional level.

The keratinocytes form the epithelial tissue, which is separated by the basement membrane (BM) from the underlying connective tissue fibroblasts (GCTFs). To

get a step closer to the *in vivo* situation, we developed a co-culture system where we could separately investigate the two co-cultured cell types, GCTFs and IHGKs. This is presented in the next chapter.



## GCTFs and Epithelial Equivalents on Micropillars

Connective tissue (CT) fibroblasts are located under the basement membrane (BM), which is separating the CT from the gingival epithelium. The CT is only poorly populated by cells, in contrast to its pendant, the epithelium. The major part in the CT is formed by extracellular matrix (ECM) molecules like collagens, proteoglycans and fibronectin (FN).<sup>[88]</sup> The ECM molecules are mainly synthesized by the cells themselves prior to their secretion. The ECM forms an elastic microenvironment for these cells. Collagen type-I is the collagen the most present in connective tissue and is produced by the CT fibroblasts. To gain stiffness, the CT fibroblasts express the intermediate filament vimentin, which is a typical protein for mesenchymal cells. The oral cavity gingival epithelium is termed lamina propria in contrast to the CT of skin epithelium, which is termed dermis due to regional differences.<sup>[55]</sup>

In former times it was believed that the fibroblasts *in vivo* only play a passive role in the tissue. Whereas, nowadays it is known that the fibroblasts of the CT are indispensable for epithelial homeostasis.<sup>[57]</sup> Within this homeostasis, diffusive molecules, so-called growth factors, play the major role in differentiation and proliferation.<sup>[89]</sup>

In the CT-epithelial junction zone the CT is separated by the basement membrane (BM) from the undermost cell layers of the oral-cavity gingiva. The BM consists of a layer of highly organized collagen-IV, laminin-1/10 and laminin-5 molecules. Whereas proliferation of epithelial cells, namely keratinocytes, is characteristic for these undermost cell layers, the basal cell layers, the early and late keratinocyte differentiation only occur in the suprabasal and apical cell layers. As mentioned in

the pervious chapter the keratins K1 and K10 are biomarkers of early keratinocyte differentiation. These markers were used as biomarkers to identify the influences of connective tissue fibroblasts grown on elastic microstructured substrates on the epithelial tissue morphogenesis.

In earlier morphogenic studies connective tissue fibroblasts were incorporated in a collagen matrix to mimic the elastic environment for connective tissue fibroblasts found *in vivo*.<sup>[73-75]</sup> The contraction of these lattices by oral or dermal connective-tissue cells or in response to fibroblasts to various growth factors was described.<sup>[90]</sup> However, within these biomechanic studies, the forces exerted by the cells were difficult to predict. Recently, there were studies on dermal fibroblasts grown in collagen-glycosaminoglycan scaffolds. The mean contractile forces exerted by these cells to the matrix were calculated to be in a range between 11 and 41 nN, while the upper bound of cell contractility was estimated to 450 nN.<sup>[90]</sup> However, these studies were made in a non-configured microenvironment.

The presented study shows a strategy to investigate epithelial morphogenesis in response to GCTFs on a predefined precise mechanically tunable microenvironment. According to the data derived from the experiments on the keratinocytes presented in the previous chapter an inter-pillar distance of 9  $\mu\text{m}$  was chosen.

## 5.1 GCTFs on Micropillars

As a first approach, we cultured GCTFs successfully on the micropillar arrays by seeding  $7.8 \times 10^3$  cells per  $\text{cm}^2$  on FN-coated pillar heads. 24 h after seeding the GCTFs were adherent and confluent. We measured the force exerted by a typical GCTF on a pillar top for 16 h, after preculturing the cells for 24 h (Fig. 5.1). A high power magnification of the phase contrast image showed a confluent cell, that was adhered to the FN-coated pillar tops (red square in Fig. 5.1 (A)). The three pillars marked with the red circle in the enlargement of the red square in Fig. 5.1 (A) were chosen for displacement measurements (Fig. 5.1 (B)), while the two non-deflected pillar served as a control to determine the center of the deflected pillar before displacement. Since the pillars provided an almost gaussian profile we determined both the center of the non-deflected and deflected pillars as described in chapter 3.1.3. The Young's modulus of the substrate was measured to be  $E = 2.5 \text{ MPa}$ . Therefore

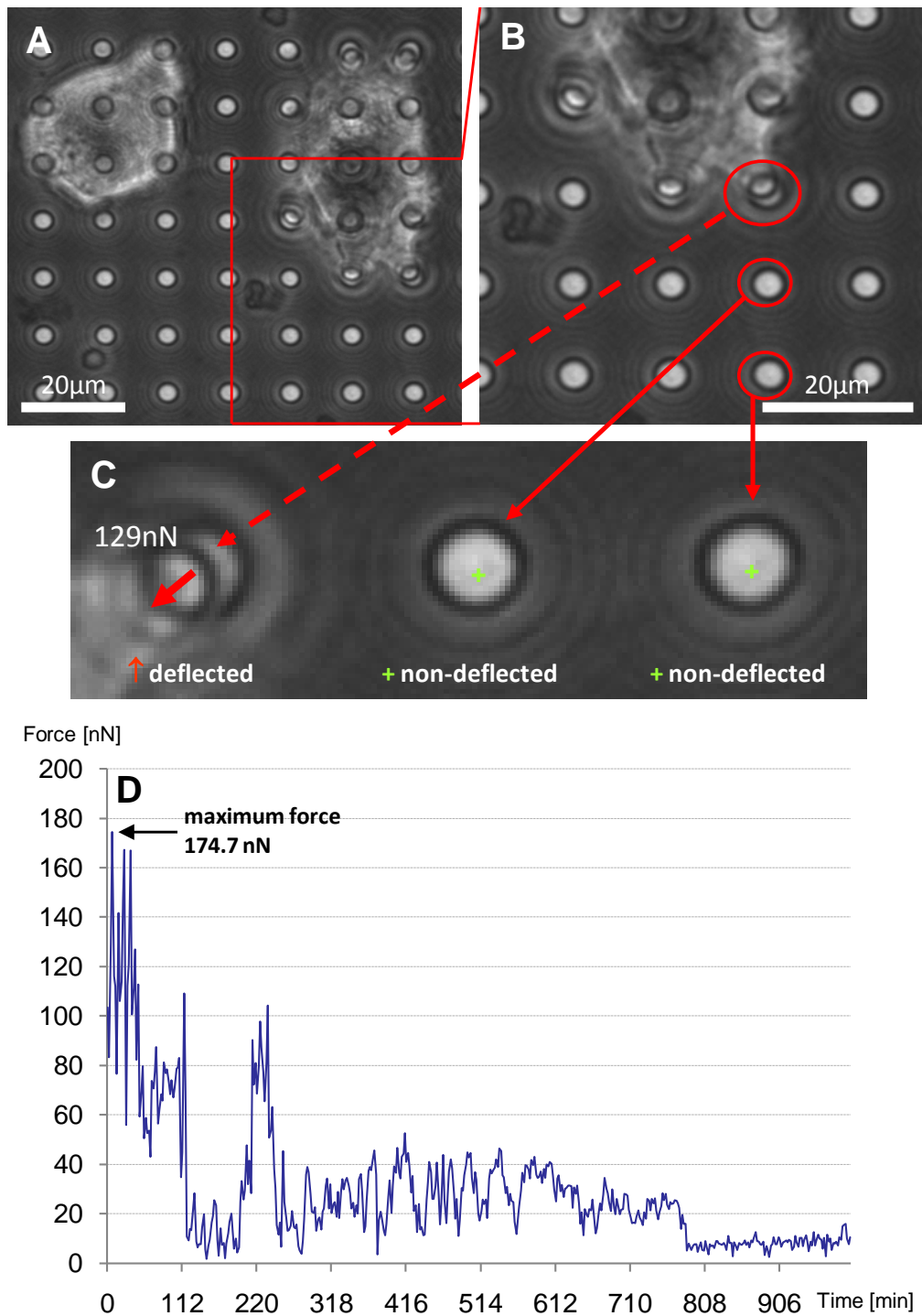


**Figure 5.1:** Live cell image of force exerted by a GCTF on a micropillar observed by phase contrast microscopy. The right cell in (A) is adherent to the pillar tops. The high magnification cut of the red square in (A) shows the deflection of the pillar (red circle in (B)) resulting from the force exerted by the GCTF on the pillar. For displacement measurements, two non-deflected pillars nearby are used (small red circles in (B)). A snapshot from a live-cell-imaging movie, where the traction force can be calculated to 129 nN at this time point is shown in (C). The traction forces exerted by a single GCTF on a single pillar over  $\sim 16$  h are calculated and show a maximum force of 174.7 nN (D). The bars in parts (A) and (B) correspond to 20  $\mu\text{m}$ . Images are modified from<sup>[59]</sup>.

the spring constant  $k$  of the pillars was calculated to be  $68 \text{ nN } \mu\text{m}$  by using equation 3.2. Thus, the traction-force diagram for a GCTFs was derived (Fig. 5.1 (D)), indicating a maximum traction force of  $174.7 \text{ nN}$  on the pillar.

After successful adhesion of the GCTFs to the micropillars, we investigated the growth behavior of the cells within the co-cultures. For that, the GCTFs were precultured for 24 h on the FN-coated pillar tops. Thereafter the cells were covered with a collagen matrix and co-cultured for 7 and 14 days with IHGKs (see chapter 3.2). Then the epithelial compartment was carefully removed. Electron micrographs revealed a subconfluent density of GCTFs at day 7 (Fig. 5.2 (A1)), whereas after 14 days they were nearly confluent (Fig. 5.2 (B1)).

We confirmed these findings both qualitatively by indirect immunofluorescence (IIF) as well as quantitatively by quantitative polymerase chain reaction (qPCR). Staining for the connective-tissue specific vimentin revealed a clear increase in the cells cultured for 14 days in comparison to 7 days (Fig. 5.2 (A) and (B)). The same situation was found for the cell-specific collagen type I (Fig. 5.2 (C) and (D)). The relative mRNA description levels, determined by qPCR, showed a  $\sim 7$ -fold increase for vimentin and collagen I for the GCTFs, grown close to confluence, at 14 days relative to the expression levels at 7 days (Fig. 5.2 (E)). The relative expression levels were normalized to the GAPDH housekeeping gene.

The increasing GCTF densities found at declining pillar distances in consistence with higher expression levels for their cell-specific proteins showed, that the GCTFs were capable to proliferate on the defined microenvironment when co-cultured with IHGKs. Additionally, the cell densities of the GCTFs increased. Thus, the chosen parameters were considered capable to further assemble an epithelial equivalent *in vitro*, and to investigate the influence of the GCTFs grown on these substrates on the morphogenesis of the epithelial cells. This assumption was confirmed by culturing the GCTFs for 14 days on the micropillars, where they formed a confluent cell sheet on the pillars (Fig. 5.3).

Thereafter, we investigated the influence of GCTFs, established on FN-functionalized micropillars, on the epithelial morphogenesis of IHGKs.

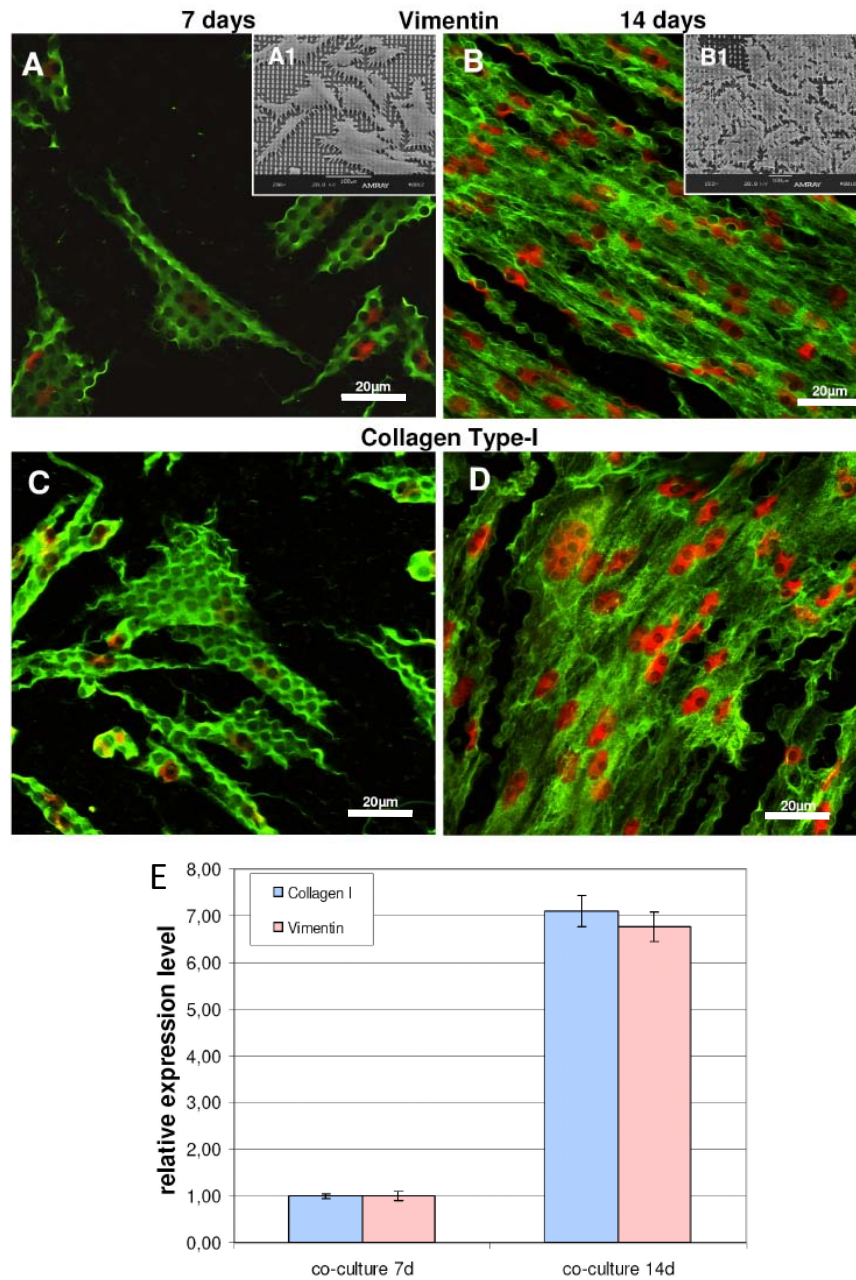


**Figure 5.2:** SEM and IIF of GCTFs, derived from co-cultures with IHGKs on FN-coated micropillars with an inter-pillar distance of 9  $\mu\text{m}$ . Electron micrographs reveal, that the GCTFs are subconfluent after a culture period of 7 days (A1) whereas they are nearly confluent after 14 days (B1). Staining the cells for cell-specific vimentin and collagen I (both in green) demarcate a clear qualitative increase of positive stained cells at 14 days (B) and (D)) compared to a culture period of 7 days ((A) and (C)). The nuclei are counterstained with PI (red). qPCR of mRNA expression of vimentin and collagen I on the different time period reveal a drastic increase of relative expression levels for both proteins at the later time period. The relative protein expression levels for cells are normalized to the  $C_T$  of the glyceraldehyd-3-phosphat-dehydrogenase (GAPDH) non-modulated housekeeping gene. Protein levels for cells cultured for 7 days are normalized to 1. The data is analyzed as described in chapter 3.5.1. (MSD: n=3). Bars correspond to 100  $\mu\text{m}$  (A1, B1) and to 20  $\mu\text{m}$  (AD). Images are modified from<sup>[59]</sup>.

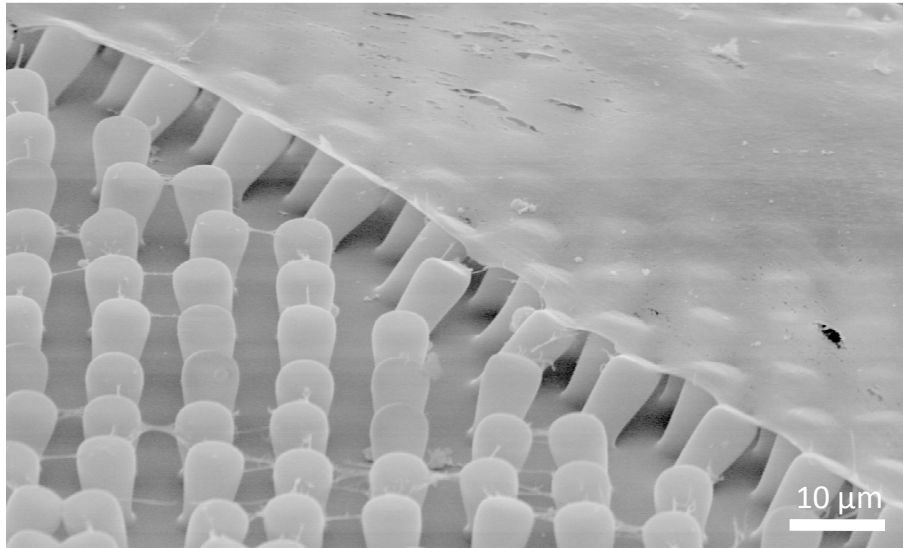


**Figure 5.3:** Electron micrograph of a confluent sheet of GCTFs on micropillars after a culture time of 24 h. The scale bar corresponds to 10  $\mu\text{m}$ . Image is modified from [59].

## 5.2 Co-Cultures of GCTFs and IHGKs on Micropillars

Co-cultures of GCTFs and IHGKs and the respective controls were generated as described in chapter 3.2. By that we could clearly separate the IHGKs from the GCTFs for the indirect immunofluorescence (IIF) and the quantitative PCR (qPCR).

The GCTFs were precultured on a micropillar structure with an inter-pillar distance of 9  $\mu\text{m}$  for 24 h. Thereafter, for the immunofluorescence, the GCTFs were covered with a collagen I lattice. For the qPCR the cells were covered with a trans-well filter set. Then, the IHGKs were seeded on these lattices and cultured for 7 or 14 days. We chose these time points and culture system because on the one hand culture periods of 7 and 14 days were found to be suitable for successful establish co-cultures of GCTFs and keratinocytes in a non-defined collagen matrix. [73–75] On the other hand the spatial separation of the GCTFs and the IHGKs mimicked the *in vivo* situation.

To qualitatively investigate the trans-active role of the GCTFs, cultured on micropillars, both for the expression of early keratinocyte differentiation markers K1 and K10, as well within the morphogenesis, we carefully separated the cultured IHGK-

layer from the underlying GCTFs at the respective time periods of 7 and 14 days. The samples were fixed, frozen and sliced into thin layers as described in chapter 3.4.

Staining by IIF for the early keratinocyte differentiation markers K1/10 revealed an inhomogeneous expression of these proteins in the epithelial equivalents derived from the co-cultures after 7 days (Fig. 5.4(A)), green fluorescence). Whereas the K1/10 was clear and homogeneous distributed in the cytoplasm after 14 days (Fig. 5.4(B)), which in some extend already started in the basal cell layer after 7 days. The cell nuclei were again counterstained by PI (red). As a proof for the direct influence of the underlying GCTFs on the expression of K1 and K10, we cultured the IHGKs without GCTFs directly on the pillar substrates for 7 and 14 days, respectively. The obtained cuts were almost devoid of detectable fluorescence for K1/10 after 7 days (inset in Fig. 5.4(A)) and showed only a patchy and irregular distribution at 14 days (inset in Fig. 5.4(B)). Additionally, the epithelial equivalents derived from IHGKs cultured on pillar arrays without GCTFs showed the tendency to contain fewer cells than IHGKs co-cultured with GCTFs.

To reinforce these findings quantitatively, we analyzed the mRNA transcription levels for K1 and K10 in the frozen sections of IHGKs co-cultures and controls at the respective time periods. We normalized the protein expression levels again to the GAPDH housekeeping gene and thereafter normalized the expression levels for the proteins after 7 days to 1. The relative expression level for keratin 1 in the co-cultured IHGKs was 7.39 fold higher at day 14 compared to day 1 (blue columns in Fig. 5.4(C)), whereas in the control the relative expression level for K1 was even lower at the later time period (blue columns in Fig. 5.4(D)). These findings paralleled quantitatively the data obtained qualitatively from the IIF. However, for K10 the mRNA quantities in the co-culture were slightly higher after 7 days and 14 (pink column in Fig. 5.4(A)) and were similar in the control (pink columns in Fig. 5.4). This quantities of expression of K10 was in accordance to the observations made in the previous chapter and to the literature.<sup>[81]</sup>

Summing up, the increase in expression of the early keratinocyte differentiation marker K1 in IHGKs, co-cultured on GCTFs, was observed both by IIF and by qPCR at the later time period. Whereas the respective control did not show this behavior. Additionally, there were similarities to the *in vivo* phenotype of the oral gingival epithelium<sup>[91,92]</sup> with respect to the protein orientation in the IHGK epithe-

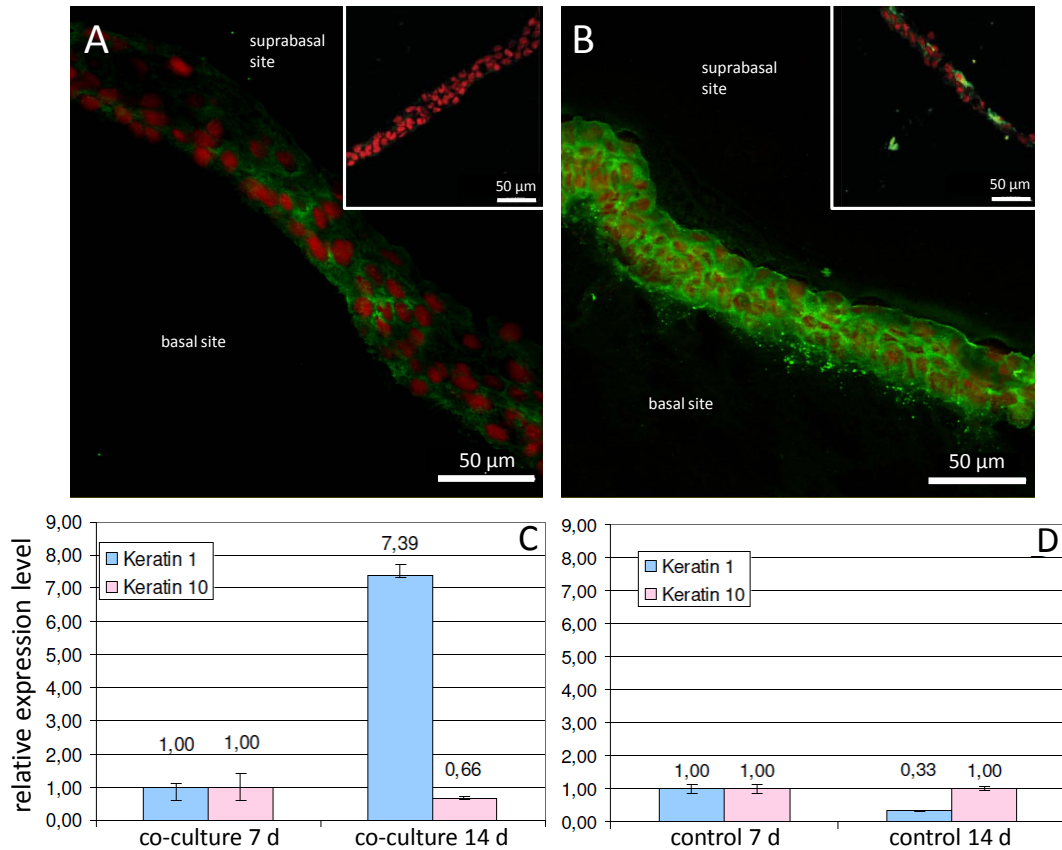


**Figure 5.4:** Indirect immunofluorescence (A) and (B) and related quantitative real-time-PCR (C) and (D) of early keratinocyte differentiation markers K1 and K10 from immortalized human gingival keratinocytes (IHGKs) derived from cryo-cuts of the co-cultures, cultivated for 7 and 14 days respectively, and matched controls. Keratin 1/10 is stained in green and the cell nucleus by PI in red. While the distribution of keratin 1 and 10 is inhomogeneous at a culture period of 7 days (A) the K1/10 is clear and homogeneously distributed in the cytoplasm after 14 days (B). IHGKs that are cultured without underlying GCTFs, as a control, are almost devoid of green fluorescence after 7 days (inset in A) and only show a irregular and patchy protein orientation at 14 days (inset in B). The findings derived from the qPCR for keratin 1 for IHGKs at the respective culture periods (C) and (D) reinforce the qualitative observation. The data is processed as described above. The relative expression levels at 7 days are normalized to 1. (MSD: n=3). The scale bars in (A) and (B) correspond to 50  $\mu$ m. Images are modified from [59].

lial equivalents cultured over 14 days on the GCTFs.

These findings suggest that the GCTFs, established and growing on the defined FN-biofunctionalized pillar array microenvironment, have a direct *in vivo*-like influence on the relative gene expression noted for K1 in the IHGKs.



## Conclusion and Outlook

The goal of this study was to create a novel biomimetic tool to investigate early differentiation of human gingival keratinocytes *in vitro*.

Since most cells in living organisms are embedded in an extracellular matrix (ECM), adhesion to this matrix and to neighboring cells play an important role in fundamental cellular functions.<sup>[15,16]</sup> It has already been shown that changes in differentiation, proliferation and cell fate are not only induced by chemical signals like cytokines, chemokines and growth factors or by physical signals like fibronectin and collagen. There is also a mechanical feedback to the substrate's stiffness and morphology.<sup>[19,93]</sup> It was shown that keratinocyte differentiation can be induced by chemical stimuli.<sup>[85]</sup> However, there is little known about differences in their differentiation due to mechanical stimuli.

In order to provide mechanical and configurable substrates for cells, fields of micropillars with different pillar interspaces were fabricated. To create adhesion points for cells, the pillars were functionalized with fibronectin (FN), because FN is ubiquitously found in the human gingiva. We proved successful biofunctionalization only of the pillar tops.

Cultures of immortalized human gingival keratinocytes were cultured successfully on the micropillars. We measured forces up to 110 nN/Pillar, exerted by the leading edge of the keratinocyte.

We characterized the morphology and the expression of the early keratinocyte differentiation markers keratin 1 and 10 with respect to different inter-pillar distances. While the keratinocytes at small inter-pillar distances of 5 and 8  $\mu\text{m}$  were round shaped and adhered on the pillar tops, they were more linear shaped and tended to

sink into the substrate at distances of 11 and 14  $\mu\text{m}$ .

The expression levels of keratin 1 and 10 were investigated both qualitatively and quantitatively. Hereby, declining inter-pillar distances revealed increased cytoplasmic extension of keratin 1. These findings coincided with the semiquantitative and quantitative PCR, which showed increased K1 transcription levels at smaller distances.

Here we could demonstrate for the first time, that the extracellular environment, independent from miscellaneous cell culture medium additives, modulated a biological relevant cell function in human gingival keratinocytes (IHGKs) in a distance-dependent manner.

The epithelial tissue, where keratinocytes differentiate and proliferate continuously, is separated by the basement membrane (BM). The BM mainly consists of highly organized collagen IV and laminin and separates the epithelial from the underlying connective tissue fibroblasts. We used our system as a biomimetic tool to investigate epithelial morphogenesis *in vitro* in co-cultures in a defined micromechanical environment. The co-cultures consisted of human gingival keratinocytes and gingival connective tissue fibroblasts (GCTFs) which reflected the physiological situation of both cell types in the human gingiva.

As the first step we successfully established mesenchymal GCTFs cultures on FN-coated pillar arrays with an inter-pillar distance of 9  $\mu\text{m}$ . It was demonstrated for the first time, that these substrates allowed for adhesion and growth of mesenchymal GCTFs. We measured forces up to 174.7 nN/pillar at the leading edge of the cell. Thereafter, IHGKs were co-cultured by a self developed co-culture system, which allowed for investigation of early keratinocyte differentiation and morphogenesis, independent from the underlying GCTFs. The cells were co-cultured for 7 days and 14 days, respectively. It could be shown, that keratin 1 was homogeneously distributed at the later culture period whereas its distribution was inhomogeneous at 7 days. The respective controls with IHGKs cultured over the same time periods did not show or exhibited only patchy keratin distribution. This finding was confirmed by quantitative PCR which revealed a 7.4 fold increase of keratin 1 expression at 14 days in comparison to the earlier time period, whereas the relative keratin 10 expression in the controls remained almost the same at both periods.

We demonstrated, that the underlying tissue fibroblasts, grown on the micropillar field, were pivotal for expression of tissue-specific markers and epithelial morpho-

genesis, and thereby the established gingival epithelium closely resembles the *in vivo* situation.

In conclusion, the used conditions are suitable for studying cell adhesion, cell growth and for determining cell-derived traction forces. The selected microenvironment can be prospectively used as a basis to study periodontal cell adhesion, growth, gene expression and synthesis of cell-specific biomolecules by varying predefined microenvironmental parameters attributing to elasticity and/or ECM cell adhesion ligands. Other cell types of the oral tissue like osteoblasts or fibroblasts from the periodontal ligament can be addressed to our developed system and are already under investigation.

In the future, the knowledge of the biological consequences of targeted variation of predefined microenvironmental parameters assigned to biofunctionalization or biomechanics can be used for the optimization of existing cell-culture substrates. This, in turn, can form the basis for optimization or even a new generation of biomaterials by varying predefined environmental parameters to achieve an *in vivo*-like cell growth and differentiation, indispensable for tissue morphogenesis during regeneration.



## **Part II**

# **Biomimetic Actin Networks**



## Introduction

Evolution has formed a vast variety of different organisms ranging from simple prokaryotes like bacteria to the "most complex eucaryote", the human. A cornerstone in evolution is that cells are highly adaptive. Unlike an assembly of mechanical parts they can tremendously change their structure, physiology and functions in response to environmental changes. In multicellular organisms they work together and organize themselves into communities called tissue and further organize to organs which finally form the organism. Although there is a tremendous effort to understand the interplay of cells to form a living healthy organism there is still no "blueprint" of the cells. Cells *in vivo* react in a very complex way to their environment. Often one can not differentiate between the different factors by which they are affected. Thus, to understand the exact mechanisms of cell behavior this complex system has to be simplified to controllable conditions. This is achieved by creating *in vitro* systems. The requirement for such systems is to be as close as possible to the *in vivo* situation at controllable conditions, thus, *mimicking* the *in vivo* situation. The aim of this study is to create a biomimetic model of the actin cortex of cells.

Beside functions like gene expression, protein synthesis and energy production, mechanical integrity and active response to the surrounding are essential for cells. Epithelial cells, for example, have to resist excessive stress, while other cells, like muscle cells, produce extensive forces in a cooperative way. There are three filamentous proteins playing an important role in these processes: microtubules, actin and intermediate filaments.<sup>1</sup> Each type of these proteins exhibits different structural and mechanical properties, dependent on their purpose. All together they form the

---

<sup>1</sup>Details are presented in the following section

cytoskeleton of a cell.

The cytoskeleton also plays a crucial role in cell division, differentiation, exo- and endocytosis, and even in stem cell fate.<sup>[19,43,94–98]</sup> Disorders of this cytoskeleton are known to be associated to many diseases. For example, the Parkinson disease is a consequence of changes in the neural cytoskeleton.<sup>[99]</sup> Epidermolysis Bullosa Simplex (EBS), which is a genetic skin disease, typified by skin blistering, is a defect in the intermediate filaments producing machinery.<sup>[61,100]</sup> Even the Alzheimer disease is related to alterations in the cytoskeleton.<sup>[101–103]</sup>

There are two different types of cytoskeletal networks found in the cell: a three-dimensional network of filamentous proteins in the cytoplasm giving the cytosol gel-like properties, and an extensive flat network of crosslinked actin, the actin cortex. It is located below the cell membrane point-wise anchored to membrane by proteins.

If the cell membrane is removed the actin bundles are visible forming an apparently random network.<sup>[104,105]</sup> Cells control their appearance by various actin binding proteins which can either crosslink, sever, cap or actively polymerize actin. Regulating these factors, the cells are actively controlling their motility, shape and their polarity.<sup>[106–108]</sup> Bundles and networks of actin serve as a supporting mesh for the plasma membrane. In bundles the actin filaments are closely packed and aligned parallel, whereas in networks they form angles of various degrees and are loosely packed.<sup>[104]</sup> This network can be considered as a partially crosslinked solution. It determines the shape of a cell and is important for mechanosensing of the environment.

Up today many studies on actin mechanics have only addressed the actin in bulk.<sup>[109–113]</sup> However, there is evidence that such networks differ from networks with infinite lateral extension both in their physical properties and structural phase transitions.<sup>[5,6]</sup> This is due to the fact that actin is a semiflexible polymer, which means that the polymer has a bending stiffness  $\kappa$  determining its shape and fluctuations. The bending rigidity  $\kappa$  of a semiflexible polymer is often and more obvious expressed in its persistence length  $l_p$  which is  $\kappa$  divided by the thermal energy. The values in literature for the persistence length vary. But generally it is believed that for stabilized actin *in vitro* the persistence length is more than 10  $\mu\text{m}$ . This in turn is comparably large to the thickness of the actin cortex which is only a few hundreds of nm, while the cortex is laterally extended over tens of microns.<sup>[114,115]</sup> Therefore it can be considered a quasi two-dimensional. Up to now there is only little known about

---

the mechanical properties of extended two-dimensional actin networks since in cells it is difficult to distinguish between effects directly mediated by this network or generated by other sources.

A biomimetic platform to create quasi two-dimensional uncrosslinked and crosslinked actin networks *in vitro* was presented by Roos *et al.* in 2003.<sup>[7]</sup> In his system filamentous actin was only grafted locally to the top of silicon micropillar arrays while the rest of the polymer could dangle free in solution. The filaments could also be crosslinked with filamin forming a self assembled network of bundles. These networks exhibit clear structural similarities with the actin cortex in cells. This biomimetic system minimized the number of parameters influencing the observations, without being unrealistic being a model of the system *in vivo*. Such extremely minimized self-assembled biomimetic quasi two-dimensional actin networks can provide insights into biophysical, biochemical and structural properties of the cell cortex. Also as a further step, Roos developed micropillars of PDMS where he could analyze microtubule gliding.<sup>[116]</sup>

Based on his studies we further developed his system. We aimed the development of a versatile, closed microfluidic biophysical reactor, in which quasi two-dimensional networks can be produced and investigated under various physicochemical conditions. Therefore, micropillar arrays, made of PDMS and fabricated by standard photolithography, were used as substrates for actin network assemblies. To allow control over the chemical environment and the flow conditions at any time of the experiment, a closed flow-cell system was developed. These flow-cells contained a microreactor, exhibiting the micropillar field, which allowed for creation of extended two-dimensional networks. Due to the free standing pillars, these networks were freely accessible to the chemical environment in three dimensions. We observed actin network bundling dynamics mediated by actin binding proteins filamin, myosin II and  $\alpha$ -actinin and by divalent cations. Moreover, the further feasibility of this tool is demonstrated.

In the first chapter of this part it is shown that unbundled and bundled self-assembled actin networks were successfully established on the micropillar arrays. The dynamics of network formation and bundling could be followed in real-time. Within the crosslinks so-called zipping events were observed. Zipping of actin in principle always occurs when actin filaments, which are covered with actin crosslinker, come in close proximity. The first formation of crosslink decreases the thermal fluc-

tuations in the nearby region of the filaments. In turn, this increases the probability for further bundling. The bundling then propagates in a zip-like manner. We could, for the first time, follow such events in real-time on a two-dimensional actin network.

In the second chapter of this part we demonstrate the feasibility of closed flow-cells containing micropillars on quantitative measurements of forced single actin unbundling by optical tweezers. We could measure unbundling forces for both  $\alpha$ -actinin and  $Mg^{2+}$ .

## 7.1 Protein filaments

Protein filaments play a crucial role in cell functionality and are highly abundant through evolution.

### 7.1.1 Microtubules

Microtubules (MTs) are hollow cylindrical polymers with an outer and inner diameter of 25 nm and 18 nm respectively. They usually consist of 13 protofilaments. However there are indications that the number of protofilaments ranges from 11 to 16.<sup>[117]</sup> The MTs can grow larger than 20  $\mu\text{m}$  in cells and 3 mm *in vitro*. The protofilaments are heterodimers of 100 kDa, containing an  $\alpha$ -tubulin and a  $\beta$ -tubulin tightly bound to each other. They are uniformly oriented in the wall giving the MT a molecular polarity, the so-called plus- and minus-end which have different polymerization kinetics and binding affinities. At the plus-end association and dissociation of dimers are much faster. MTs undergo a rapid depolymerization and regrow over seconds.  $\beta$ -tubulin is oriented towards the plus-end and  $\alpha$ -tubulin towards the minus-end (Fig. 7.1 (B)). Both tubulins have a binding pocket for GTP.<sup>[20]</sup> When the dimer associates to the MT the GTP in the  $\beta$ -tubulin hydrolyses to GDP.<sup>[118]</sup> The polymerization process is characterized by rapid depolymerization and regrow called dynamic instability (Fig. 7.1 (A)).<sup>[119]</sup> This helps the cell to reconfigure the MT network rapidly, e.g. during mitosis. Typically the plus-end of the MTs is oriented to the periphery of the cell whereas the minus-end is anchored in a microtubule-organizing center, the centrosomes for cytoplasmical MTs and basal bodies for axomes. During

mitosis the MTs polymerize from these centrosomes forming the mitotic spindle to separate the chromosomes.<sup>[120,121]</sup>

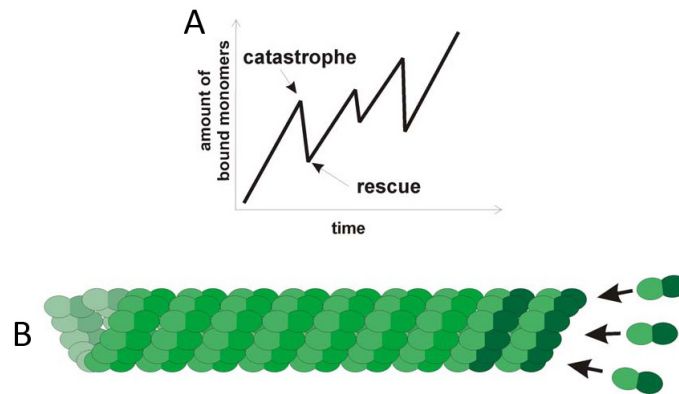


**Figure 7.1:** Model of microtubule polymerisation. (A) Dynamic instability of MT growth. The polymerisation of MTs undergoes a rapid depolymerisation and regrows over seconds. (B) Model of MT growth.  $\beta$ -tubulin (dark green) is oriented towards the plus-end and  $\alpha$ -tubulin (light green) towards the minus-end. The heterodimers consisting of  $\alpha$ - and GTP- $\beta$ -tubulin associate to the plus-end of the growing MT.<sup>[20,122]</sup>

MTs have a persistence length of more than 1 mm.<sup>[123,124]</sup> Their stiffness, length and polarity make them valuable for both cytoskeletal transport and intracellular transport. In various cells MTs and actin cooperate in cellular processes.<sup>[125]</sup> They can also resist compression.<sup>[126]</sup> Therefore they are believed to support asymmetrical cellular structures rather than actin or intermediate filaments.<sup>[107,127]</sup> There are more than a dozen microtubule-associated proteins (MAPs) known, which can sever or stabilize MTs, bind to MT ends or to its dimers. Within these MAPs there are two motor families in eucaryotes, kinesins and dyneins. Conventional kinesin (kinesin-1) moves organelles to the plus-end<sup>[128]</sup>, while dynein walks to the minus-end. This motor activity on single MTs could be observed *in vitro* by using kinesin-coated micropillar interfaces.<sup>[116]</sup> Self-organized networks of MTs and motors have been also studied *in vitro*.<sup>[129]</sup>

### 7.1.2 Intermediate Filaments

Intermediate Filaments (IFs) are stress resistant and more flexible than the other cytoskeletal filaments. The diameter of 10  $\mu\text{m}$  is in between that of microtubules

and actin. This is why they are called intermediate filaments. An introduction to this class of filaments was given in chapter 2.

### 7.1.3 Actin

Actin is one of the most conservative proteins in evolution. It is ubiquitously found in eucaryotic cells in different concentrations. In muscle cells 60% of the total protein mass is actin, non-muscle cells contain around 25%. Actin is probably one of the most investigated proteins. It is involved in many vital cell functions like cell division, cell motility, muscle contraction, endo- and exocytosis, and guided cargo transport. There are numerous homologous of actin found in cells. They can be classified in ten classes. The amino acid sequences are highly conserved within these classes. Moreover, there are over 60 classes of actin binding proteins (ABPs) known. Actin is a globular protein (G-actin) that polymerizes under physiological conditions and in presence of ATP to filamentous actin (F-actin). The monomer has a mass of 42 kDa, containing around 375 amino acids. It has 4 subunits that enclose the ATP binding site. F-actin is a double stranded  $\alpha$ -helix with a diameter of 5-9 nm and a pseudo-periodicity of  $\sim 36\text{nm}$ .<sup>[130,131]</sup> Therefore it has the smallest diameter within the cytoskeletal filaments.

The polymerization to F-actin is a multi-step process, which starts with the nucleation of monomers to dimers or trimers, followed by the growth of the filament on both ends and leading into the so-called treadmilling cycle, which is shown schematically in Fig. 7.3:

- Nucleation (Fig. 7.3 (A)): Each G-actin contains a charge of  $11 e^-$ . At a certain concentration of G-actin it overcomes its electrostatic repulsion and forms dimers or trimers. This nucleation process is very slow, so the nucleation rate  $k_n$  is the limiting factor in the whole polymerization. The growth can only start from these seeds. However, cells contain as well nucleation proteins, like ARP2/3, from where filament growth can be initiated.
- Filament growth (Fig. 7.3 (B)): In the presence of ATP the filament grows from both ends. However the adsorption kinetics at these end are different. Actin is asymmetric. It has a barbed end and a pointed end. The adsorption rate  $k_1$  for G-actin at the barbed end is much higher than  $k_2$  at the pointed

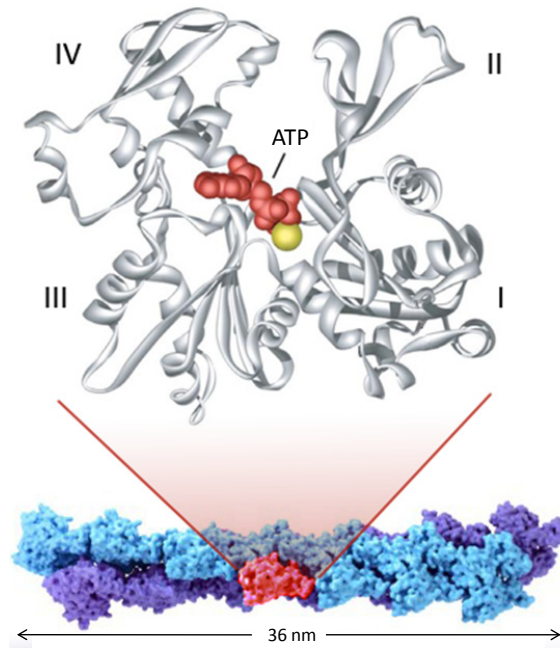


**Figure 7.2:** Structure of F-actin. The monomer consists of 4 subunits that enclose the ATP binding site. The filamentous actin has a pseudo-periodicity of 36 nm. Image is modified from (<http://ghr.nlm.nih.gov/handbook/illustrations/actin.jpg>).

end. Whereas, the situation is *vice versa* for the desorption rate  $k_{-1}$  and  $k_{-2}$ . However, at this state the monomer concentration in bulk is high enough to polymerize the filament at both ends under hydrolysis of ATP to ADP.

- Treadmilling cycle (Fig. 7.3 (C)): With decreasing monomer concentration in the bulk the desorption rate  $k_{-2}$  at the pointed end overcomes the adsorption rate  $k_2$ , while at the barbed end the desorption rate  $k_{-1}$  is still small. If ATP is present in the bulk, this leads to a dynamic equilibrium situation of depolymerization at the pointed and polymerization at the barbed end under consumption of ATP. The overall length of the filament remains constant. This process is called treadmilling cycle. The average migration velocity in the filament can reach  $2 \mu\text{m/h}$ .

If the ATP concentration in the bulk drops or the actin monomer concentration falls under the critical concentration for polymerization, the depolymerization rate is high enough to shrink the actin filament. This is why F-actin *in vitro* has to be stabilized. Stabilization is commonly achieved by phalloidin, a toxic from the death cap (*amanita phalloides*), which only binds to F-actin and prevents depolymeriza-

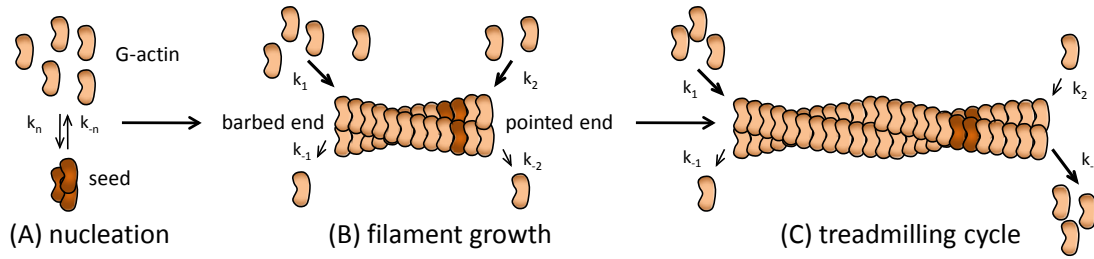


**Figure 7.3:** The scheme shows the multi-step mechanism of actin polymerization. (A) If the monomer concentration is high enough, the actin monomers form dimers or trimers in the nucleation step. This is defined by the rate constant  $k_n$ . Since  $k_n$  is small this is the speed limiting step of filament assembly. From this seed the filament grows at different concentration rates  $k_1$  and  $k_2$  (B) until a dynamic equilibrium where monomer adsorption rate at the barbed end  $k_1$  equals the desorption rate  $k_{-2}$  at the pointed end. The overall filament length remains constant. This is called the treadmilling cycle (C).

tion.

For the polymerization a high ionic strength and the presence of divalent cations  $Mg^{2+}$  and  $Ca^{2+}$  are necessary as well. [132,133]

For a cell it is pivotal to control this dynamic process of actin polymerization. Despite of regulating the polymerization dynamics by varying the ATP or monomer concentration, the cell can actively either promote or inhibit polymerization and depolymerization, by expressing nucleation promoting proteins, severing substances, capping proteins, or proteins to complex monomers to prevent nucleation. [133,134]

Moreover, the cells can customize the appearance and the mechanical behavior of the filaments in the cytoskeleton according to their requirements. Proteins can crosslink filamentous actin to bundles which form stress fibers or transport guides for cargo. They can interconnect them to form networks or to associate them to other cell compartments like the cell membrane or the nucleus or even to connect them with microtubules or intermediate filaments. [135,136] Actin bundles are also formed as a guide to create directed forces mediated by motor proteins like myosins.

The actin cortex as a part of the cytoskeleton is an extended flat network of partially crosslinked actin, point-wise grafted to the cell membrane.

In our studies the self-assembled two-dimensional actin networks were crosslinked with  $Mg^{2+}$  and the actin binding proteins filamin,  $\alpha$ -actinin and the motor protein myosin II.

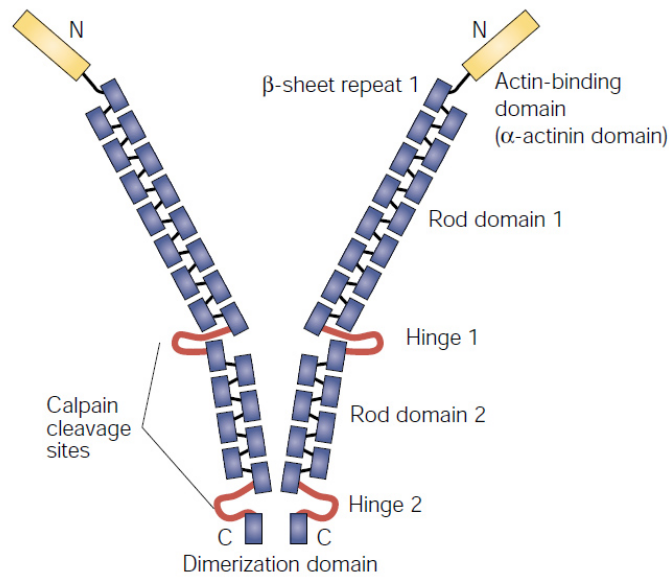


**Figure 7.4:** Structure of human filamin. The filamin is a homodimer. Each of the two filamin monomers contain an actin-binding domain at their N-terminus. They dimerize at their C-terminus. The rod-like structure is interrupted by two hinge regions which make the protein very flexible. Image is adapted from <sup>[137]</sup>.

## 7.2 Actin Binding Proteins (ABPs)

### 7.2.1 Filamin

Filamin is long flexible tail-to-tail homodimer with a mass of 270 kDa (Fig. 7.4). It has a length of 160 nm, a diameter of 3-5 nm and has a rod-like structure. <sup>[138,139]</sup> It contains one actin binding site located at the N-terminal of each monomer. In most cell type many isoforms of filamin are found. The number of the isoforms is still undetermined. There was even isoform switching observed during myogenesis. <sup>[140,141]</sup> Depending on the isoform, the rods contain one or two hinge regions which make the protein rather flexible. Filamin is dimerised at its C-terminal. <sup>[142]</sup>

Filamin is one of the major components in actin networks and plays a crucial role in the three-dimensional *in vitro* and in *in vivo* arrangement of the actin fibers. <sup>[143]</sup> *In vitro* it can either bundle the actin at high filamin/actin ratios or form three-dimensional actin networks at lower concentrations which have the properties of a viscoelastic gel. <sup>[112,144]</sup> Filamin crosslinks starts at very molar ratios of filamin dimer to actin monomer. <sup>[145]</sup> It was shown that already a molar ratio of 1:700 is sufficient

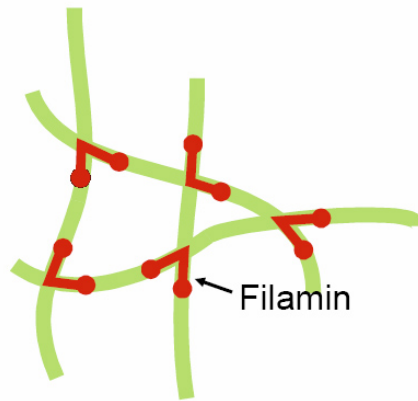


**Figure 7.5:** F-Actin network crosslinked with Filamin. The actin can be crosslinked in various angles due to the flexible structure of filamin.

to crosslink actin<sup>[137,146]</sup>, which is probably due to its high flexibility, because it does not have increased binding affinity in comparison to other crosslinkers.<sup>[147,148]</sup>

*In vitro* networks of actin often have remarkable high crossing angles (Fig. 7.5).<sup>[149]</sup> It was found that prestressed actin networks hinged by filamin replicate the mechanical properties of cells.<sup>[112]</sup>

### 7.2.2 $\alpha$ -Actinin

$\alpha$ -Actinin forms a rod-shaped antiparallel homodimer. Each subunit has a mass of  $\sim 100$  kDa. It was discovered as a component of the Z-disc in skeletal muscles. But it was found out recently that it is also related to adherence-type junctions, membrane associated dense plaques and cytoplasmic dense bodies of smooth muscles.<sup>[150]</sup> The actin binding region is located at the N-terminus of each monomer. The length of the protein varies between 3-4 nm in diameter and 30-40 nm in length. However lengths up to 44 nm can be found. The length is also dependent on the salt concentration. At low salt concentrations  $\alpha$ -actinin has a length of about 74 nm. Thus is suggested that it exists in a compact and in an extended conformation.

The binding properties and the interaction between actin and  $\alpha$ -actinin is rather complex. The binding affinity  $k_d$  of  $\alpha$ -actinin from actin varies within the species between 0.6-4.7  $\mu\text{M}$ .<sup>[151]</sup> The binding reduces at higher temperatures. Additionally there is a phase transition in network formation of  $\alpha$ -actinin with actin. At high  $\alpha$ -actinin concentrations the actin is bundled, whereas at low concentrations isotropic networks are formed. A temperature dependent gel-sol transitions in  $\alpha$ -

actinin crosslinked actin networks could also be observed.<sup>[152]</sup> It is suggested that  $\alpha$ -actinin binds to the opposite site of the actin subdomain 1 than that recognized by myosin.<sup>[153]</sup>

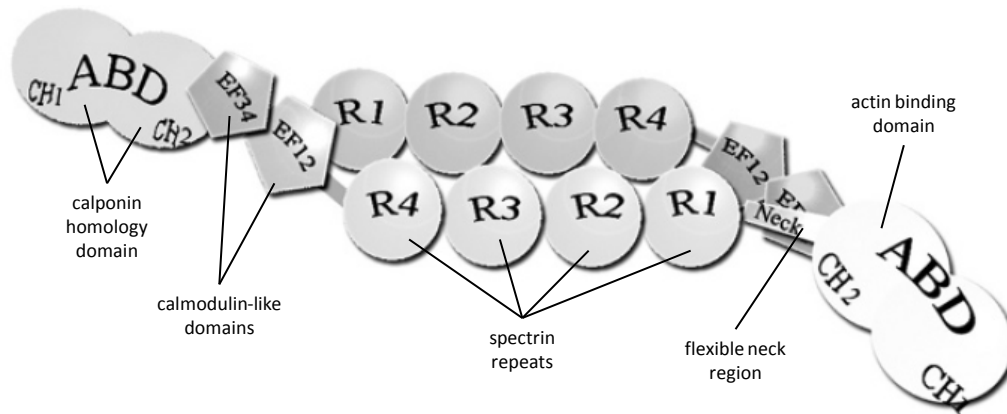


**Figure 7.6:** Schematic of the structure of  $\alpha$ -actinin. The actin binding regions are located at the N-termini of the antiparallel homodimer, followed by a flexible neck region. After 4 spectrin repeats the monomers end in 2 calmodulin (CaM)-like domains. Image is adapted from<sup>[154]</sup>

### 7.2.3 Myosin II

Among the many different types of myosins the myosin type II was the first to be discovered. Myosin belongs to the family of ATPase motor proteins transforming chemical energy to mechanical energy. This energy is derived from the cleavage of adenosine-triphosphate (ATP) in adenosine-diphosphate (ADP) and inorganic phosphate. Up to now 17 classes of myosins are known.

Myosin II is abundant most eucaryotic cells. It is a dimeric protein containing two heavy chains of  $\sim 200$  kDa, 2 essential light chains and 2 regulatory light chains of  $\sim 20$  kDa.<sup>[155,156]</sup> The C-termini of the heavy chains coil together and form an  $\alpha$ -helix, 150 nm long, the so-called coiled-coil structure. By enzymatic cleavage of myosin with chymotrypsin a heavy chain and a light chain can be derived. The light chain is the C-terminus of the myosin and has a rod-like structure with a length of about 100 nm. It is insoluble in water at physiological conditions and is also called light meromyosin (LMM). The heavy chain (heavy meromyosin, HMM) can be further cleaved enzymatically by papain in the neck region (S2) and the head region (S1).<sup>[157]</sup> The S2 part is a 50 nm long soluble region, which interconnects the

head with the stalk. The S2 together with the stalk are responsible for the bundle formation found for myosin under physiological conditions.

The head domain has a length of 15-20 nm and a diameter of 4-5 nm. It is soluble in water under all salt conditions.<sup>[158]</sup> In muscles the heads of the myosin reach from the core of the thick myosin filaments and can interact with the nearby actin filaments. It was shown that this globular head region alone contains both the actin binding region and the motor activity.<sup>[104,159,160]</sup>

As mentioned, the myosin converts the chemical energy of ATP in mechanical energy. During this process, the protein changes its conformation, the so-called force-stroke. The mechanism of this process was first postulated by Huxley in 1958.<sup>[161]</sup> This so-called *rotating-crossbridge-model* (RCM) describes the mechanism of the directed force translation of myosin to the actin filaments. Nowadays it is believed that the stroke of one single myosin II head advances the actin of about 5 nm<sup>[118]</sup> and it was found that the force for one stroke is  $\sim 1$  pN.<sup>[162]</sup> Myosin II is a non-processive motor protein moving from the plus to the minus end of the actin. Non-processive means that within the force stroke the myosin detaches from the actin. Without ATP, the myosin is tightly bond to the actin (*rigor-state*).

In muscles the myosin filaments and the actin filaments are closely packed. Additionally, non-processive motor proteins have a small duty ratio, which is the relation between the time the motor binds to the actin and the overall cycle time. During contraction, the heads act asynchronously, ensuring continuous sliding of the actin along the myosin.<sup>[128,163]</sup> Myosin from the skeletal muscle can gain velocities up to  $6 \mu\text{m/s}$  *in vivo* and  $8 \mu\text{m/s}$  *in vitro*.<sup>[164-166]</sup>

## 7.3 Optical Tweezers

The crucial part in optical tweezers is a coherent monochromatic light source of high intensity, a laser. The laser is focused in the sample and can trap dielectric particles in its focus.

The mechanism of trapping in a single laser beam can not be explained by simple radiation pressure. Here the light passes a space filled with medium and interferes with a dielectric particle. In the following the origin of trapping forces of on the applied theory will be presented briefly.

The optics for objects much bigger than the wavelength of the light ( $r \geq 10\lambda$ ) can be

explained simply by ray optics which describe the relationship between the angles of incidence and refraction of light beams passing through the particle.

If the objects are in the same of size or bigger than the wavelength of the incident the Rayleigh-Guns-Debye (RGD) theory can be employed. The exact solution for a single particle in this regime was described by Mie (Gustav Mie (1869-1957)), the so-called Mie theory. For smaller objects, that means much smaller than the wavelength an electromagnetic description has to be used, the Rayleigh theory (Rayleigh (1842-1919), which considers the particles as point-like dipoles in an electromagnetic field. Since the microspheres used in the following experiments have a diameter  $\geq 1 \mu\text{m}$  their optical properties can be described by the Mie theory. A schematic view a principle of single laser trap is shown in Fig. 7.7. When a beam with a typical gaussian profile in a medium with a refractive index  $n_m$  hits an object with a higher or lower refractive index  $n_o$  the light is diffracted. This changes the momentum of the rays and a due to the momentum conservation theory a opposite momentum has to be transferred to the object. For optical traps usually  $n_m < n_o$ . If the object is slightly shifted to the left of the center of the beam (Fig. 7.7 (A)), more light is diffracted to the left due to the gaussian profile of the beam. So their momentum transferred to the object points to the right and pulls it to the center of the beam. If the object is exactly in the focus of the beam (Fig. 7.7 (B)) the sum of the radial momentum components is zero. Accordingly the forces on an object in a stable optical trap always point to the center of intensity. So objectives with a high numerical aperture and strong monochromatic light sources are used in optical traps. One can also see that peripheral rays contribute more to the trapping force than center rays, so the performance of an optical trap can also improved by overfilling the aperture of the objective.<sup>[167]</sup>

The restoring force of a particle trapped with an optical trap towards the trap center is approximated to the restoring force of a spring (Hookes Law). The force is proportional to the displacement  $x$  and dependent on the spring constant  $k$ :

$$F = -\kappa x \tag{7.1}$$

which is valid for displacements of around half of the particle's radius.<sup>[168]</sup> At known spring constant  $\kappa$  for the trap and displacement  $\Delta x$  of the particle from the trap's center, the force  $F$  can be calculated.

The optical trap can be calibrated using the Brownian motion of the particle either

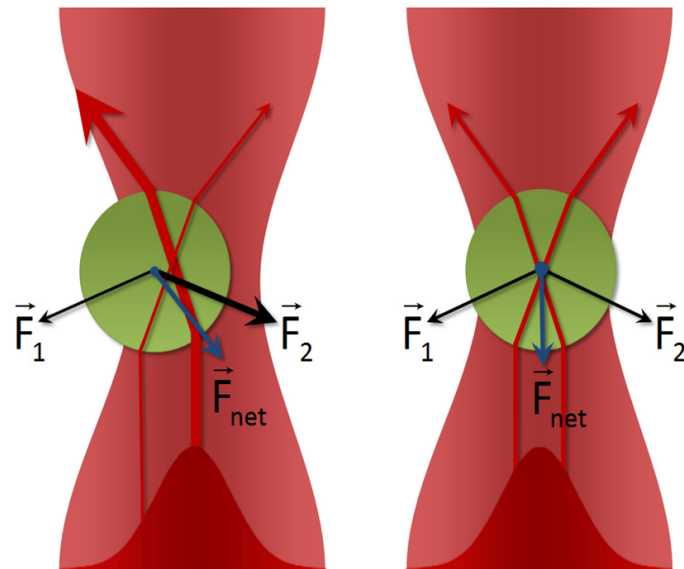


**Figure 7.7:** Scheme of an optical trap. (A) A momentum is transferred to the dielectric sphere pulling it back to the center of the trap. (B) The radial momentum components transferred on the sphere sum up to zero in the center of the trap.

with a statistical or a power spectrum analysis. For details refer to<sup>[169]</sup>.

# Materials and Methods

## 8.1 Microfluidic Devices

To allow experiments investigating of 2-dimensional actin networks on micropillars, a controlled microenvironment is required. Building up such networks in an open system is hardly possible since the creation of high local flows affect the protein structures and destroy them. Additionally, the amount of protein solutions needed for experiments in flow-cells is in the range of microliters, and therefore is significantly smaller than for open systems. It was shown, that it is possible to create actin networks on micropillars in a simple flow-cell having a sticky tape on a coverslip with the micropillar field above.<sup>[170]</sup> However, these microfluidic devices could not provide defined flow speeds.

In this work, closed microfluidic flows cells were fabricated that could be combined with microfabricated pillar arrays. These cells allowed control over the flow speed and the chemical environment within the experiment. This further allowed feasibility both for bundling experiments on 2-dimensional actin networks, flow experiments and investigation of actin unbundling forces by single optical tweezers.

The flow-cells were made of polydimethyl-siloxane which contained structures produced by photolithographic techniques.<sup>[171,172]</sup> The flow-cells consisted of two parts which had to be fabricated differently: the micropillar field and the flow channel.

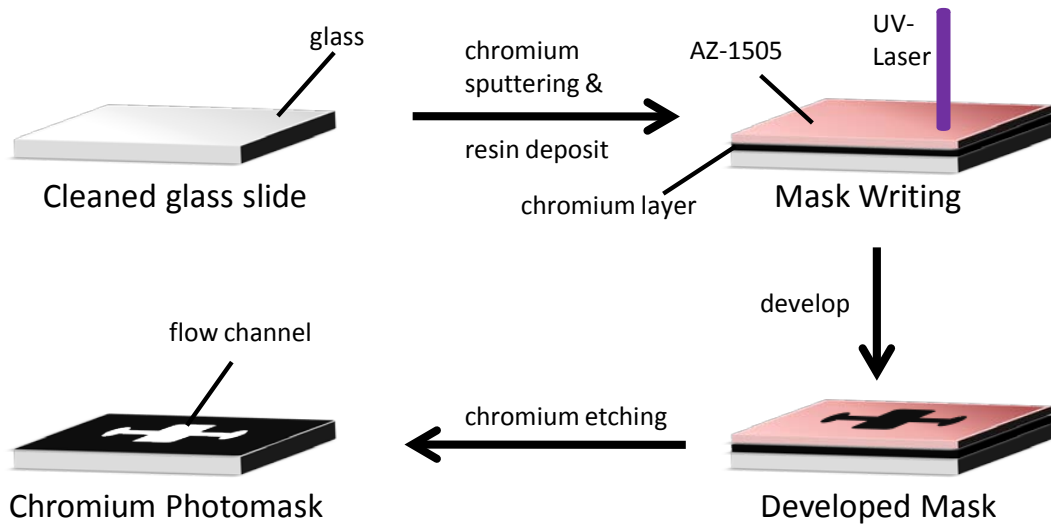


**Figure 8.1:** Scheme of steps for the production of a chromium photomask for the flow-channel. A cleaned glass is sputtered with chromium and spin-coated with positive photoresist. Then, a UV-laser writes the desired structure on the resist. By development the exposed area is dissolved from the substrate. The unprotected chromium is etched and the desired photomask is obtained.

### 8.1.1 Fabrication of the Photomask for the Flow-Channel

The technique to fabricate masks for microstructured pillar fields was already described in chapter 3.1. However, the fabrication parameters for the microfluidic channel differed slightly.

Whereas the the parameters for the production of the photomask remained the same as for the pillar fields, the chromium layer was sputtered on the glass slide before applying the positive resist (Fig. 8.1). In the deveolment process the exposed region was dissolved and the chromium remained unprotected and etched in a chromium etching solution (Merck, 1 min, 1:3 diluted in water). Therefore, the unexposed regions remained black in contrast to the micropillar fabrication, where the exposed regions remained as black chromium disks. One must consider that the dimensions of the channel must fit to the pillar field created for the later assembly to a closed flow-cell.

**Table 8.1:** Photolithographic process of SU-8 mould fabrication of flow channels with a height of 40  $\mu\text{m}$ 

Process Step	Parameter
<b>Waver preparation</b>	Drying: 5 $\times$ 5 cm glass slide 15 min at 200°C
<b>Application of resin</b>	Spin coating: 2 ml SU8-25: 10 s at 500 rpm 50 s at 1000 rpm
<b>Soft bake</b>	Hot plate: 3 min at 65°C 7 min at 95°C
<b>Exposure</b>	350 W HBO, (MJB3): 8-10 s
<b>Post exposure bake</b>	Hot plate: 2 min at 65°C 5 min at 95°C
<b>Development</b>	SU8 developer mrDEV-600: 2 x 2 min

### 8.1.2 Fabrication of the Master for the Flow-channel

A glass slide (5 $\times$ 5 mm) was cleaned and slightly etched in Extran solution (1:10 diluted in water) in an ultrasonic bath for 15 min. After that it was blown dry under nitrogen and left in an oven at 200°C for 15 min. The desired height for the channel was 40  $\mu\text{m}$ . Therefore, the resist SU8-25 was used. The following of the procedure steps are listed in Tab. 8.1.

Again the slide's surface was passivated with 1H,1H,2H,2H-perfluorooctyltrichlorosilane as described before, to facilitate the later detachment of the PDMS by chemical vapor deposition.

### 8.1.3 PDMS-casting and Flow-cell Assembly

As described previously, the PDMS was mixed in a ratio of 10:1 base to crosslinker ratio and evaporated to remove trapped air. To create the pillar field structure, ~5 ml of PDMS were poured over the pillar structure in a 2 inch petri dish while only a drop of PDMS was applied to a cleaned 24×60 mm coverslip (Carl Roth, Karlsruhe). The channel structure was pressed tightly onto the coverslip. They were left in an oven for at least 4 h at 65°C.

Thereafter the master was peeled off the coverslip with a razor blade under ethanol in order to obtain the channel structure. Whereas, the pillar structure was peeled off the wafer by hand and cut with a razor blade to fit over the channel structure.

To attach the tubing to the pillar field, two holes were drilled to fit to the two ends of the microchannel by a biopsy punch with a diameter of 0.75 mm in diameter (Harris Uni-Core, Ted Pella Inc., Redding, CA).<sup>[173]</sup> Then polyethylene tubes of 0.61 mm in diameter were drawn through the holes (Smiths Medical, Watford, UK, inner diameter: 0.28 mm) and pulled back to exactly fit to the surface level of the substrate. The tubes were sealed with a two component silicon rubber (Twinsil; Picodent GmbH, Wipperfürth).

In order to assemble the flow-cell the two parts have to be mounted in a way that the pillar structure exactly fits to the channel. To create a stable adhesion of the two parts to each other the substrate containing the channel was activated in an oxygen plasma for 30 s at 150 W and 0.5 mbar (100-E, TePla AG, Wetzlar). In this process the plasma oxidizes the methyl groups of the PDMS. The so-created Si-OH groups on the surface can form stable bonds to the other surface.<sup>[174–176]</sup> After mounting the two parts, the edges between the two PDMS parts were also sealed with Twinsil. A schematic drawing for the flow-cell assembly is shown in Fig. 8.2.

## 8.2 Actin, Actin-Binding-Proteins and Buffer Solutions

A critical point in the experiments is the quality of the required proteins. Bacterial proteases and oxidative processes can easily damage proteins in solution.<sup>[177–179]</sup> In such cases, even different bundling behavior and polymerization rates of actin could

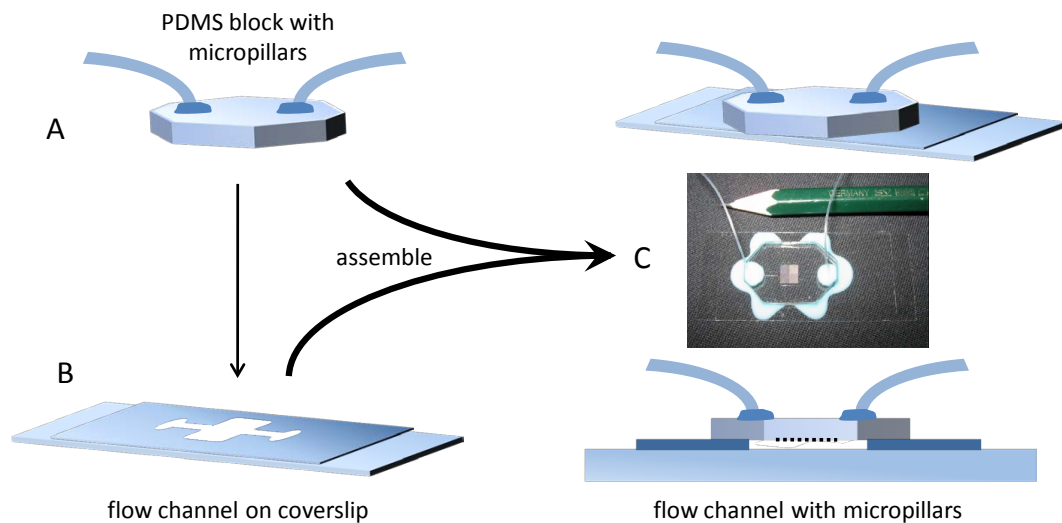


**Figure 8.2:** Schematic of flow-cell assembly. The PDMS-block, containing the micropillar field and the attached tubes (A), is placed exactly over the flow channel (B) to get a closed flow-cell (C). The picture in (C) is taken by Timo Maier.

be observed. <sup>[180,181]</sup>

To diminish effects of actin degradation in the experiments, the actin had to be always polymerized and diluted freshly. Freshly polymerized F-actin which has a concentration of 5  $\mu\text{M}$  can be stored up to three weeks, while its dilution in T-buffer necessary for the experiments has to be prepared before each experiment. Additionally its integrity has to be controlled. Unpolymerized G-actin can be kept in solution for only a few days.

Therefore actin storage and preparation of buffer solutions were designed to provide fresh solutions for the experiments at any time without great effort.

## 8.2.1 Actin

### Isolation and Purification

Actin monomers (G-actin) were prepared from rabbit skeletal muscle following the established method of Pardee and Spudich. <sup>[182]</sup> Additionally it was purified by an additional step using gel column chromatography (Sephacryl S-300) to remove residual cross-linking and capping proteins, as described by MacLean-Fletcher and Pollard. <sup>[183]</sup> Only the late fractions of the molecule peak from the column chromatography were used, because earlier fractions could also contain tropomyosin which is

**Table 8.2:** G-buffer, pH: 8,0 (*MW*: molecular weight, *c*: concentration, *m*: content in 1000 ml buffer)

Substance	<i>MW</i> in [g/mol]	<i>c</i> in [mmol/l]	<i>m</i> [mg]
TRIS	121	2.0	242
CaCl <sub>2</sub> · 2H <sub>2</sub> O	147	0.2	19
DTT	154	0.2	31
NaN <sub>3</sub> (20% solution)	65	3.0	1 ml
Na <sub>2</sub> ATP	551	0.2	110

known to alter the crosslinking properties of the actin. Aliquots of 3 mg were freeze-dried using a (Lyophilizer) and can be stored at -80°C for more than 12 months.

### Storage and Dialysis

The aliquots were defrosted and diluted in 2 ml degassed MilliQ water and were dialyzed to remove residual elution buffer from the chromatography. The diluted actin was injected in a dialysis cassette Slid-A-Lyzer, MWCO 7000; Perbio, Bonn) and dialyzed against so-called G-buffer ("G" for globular actin). The buffer contained 20% sodium azide to mortify bacteria and dithiothreitol to stabilize the actin. The pH-value was adjusted to 8.

The solution was ultra centrifuged at 100,000 g for 2 hours (Sorvall Discovery M 120 SE; Thermo Scientific, Waltham, MA) to remove degraded protein and bacteria. The actin concentration was determined using UV-Vis spectroscopy (Nanodrop 1000; Thermo Scientific, Waltham, MA) by its absorbance at 290 nm where actin has an extinction coefficient ( $\epsilon^{290}$ ) of 0.63 ml/mg. 20% ethylene glycol were added to prevent the formation of ice crystals during the following freezing process.

The dialyzed actin was stored at -80°C. To avoid harming of the actin the aliquots containing 0.5 nmol actin were dropped into liquid nitrogen, collected in PCR-tubes and stored at -80°C. The amount of volume needed had to be marked on the PCR-tubes.

### Polymerization and Staining

The actin was polymerized in the so-called F-buffer ("F" for F-actin) at 5  $\mu$ M actin. Above concentrations of  $\sim$  1 mM G-actin, at high salt concentrations and in the

**Table 8.3:** F-buffer, pH: 8.0 (*MW*: molecular weight, *c*: concentration, *m*: content in 100 ml 10x buffer)

Substance	<i>MW</i> in [g/mol]	<i>c</i> in [mmol/l]	<i>m</i> [mg]
TRIS	121	2.0	240
MgCl <sub>2</sub> · 6H <sub>2</sub> O	203	2.0	410
KCl	75	100.0	7500
CaCl <sub>2</sub> · 2H <sub>2</sub> O	147	0.2	30
DTT	154	0.2	30
MgATP	507	0.5	250

**Table 8.4:** T-buffer, pH: 7.4 (*MW*: molecular weight, *c*: concentration, *m*: content in 100 ml 10x buffer)

Substance	<i>MW</i> in [g/mol]	<i>c</i> in [mmol/l]	<i>m</i> [mg]
Imidazol	69	25.0	1700
EGTA	380	1.0	380
MgCl <sub>2</sub> · 6H <sub>2</sub> O	203	4.0	812
KCl	75	25.0	1870

presence of ATP, actin polymerizes to F-actin. F-buffer was prepared as a 10x stock stored in 50  $\mu$ l aliquots at -20°C to prevent hydrolyzation of the ATP. The concentration of the actin for the polymerization had to be 5  $\mu$ M. Therefore, 10  $\mu$ l 10x F-buffer were diluted in an amount of degassed Milli-Q water, that the obtained volume together with one aliquot of actin was 95  $\mu$ l. This solution was mixed gently and stored at 4°C for 30 min. To prevent the filamentous actin from depolymerization and simultaneously label it for further investigation via fluorescence microscopy phalloidin-TRITC (Sigma-Aldrich) was added. Phalloidin only binds to filamentous actin while TRITC is a rhodamine dye with a maximum absorption wavelength of  $\lambda = 544$  nm and a maximum emission wavelength of  $\lambda = 527$  nm. The phalloidin-TRITC was diluted to 0.1 mM in Methanol (0.1 mM in methanol, Sigma-Aldrich). Thereafter, 5  $\mu$ l of that solution was added to the polymerized actin and kept overnight to complete actin polymerization.

To use the actin in flow-cell experiments it had to be diluted 1:200 in T-buffer ("T" for test). This buffer was also prepared as a 10x stock and kept at -20°C in 2 ml aliquots. The integrity and length of the filaments was checked prior to every experiment by using laser scanning microscopy (LSM Pascal 5, Carl Zeiss, Jena).

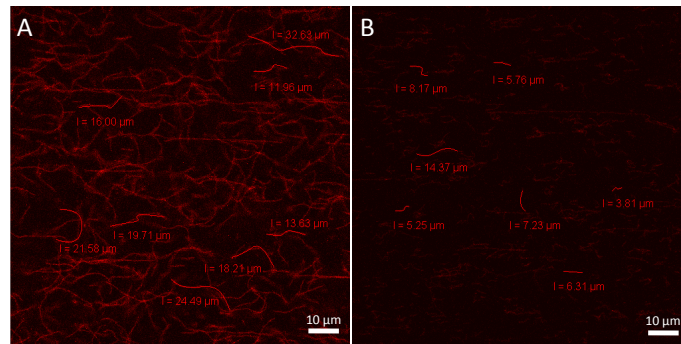


**Figure 8.3:** Confocal micrographs of actin filaments attached to a glass surface. (A) The polymerized stained actin filaments exhibit an average length of over  $10\ \mu\text{m}$  and show a reasonable fluorescence intensity. They can be used for further experiments. Whereas samples as shown in (B) should be avoided since the filaments are only faint and many short pieces are visible. The scale bar corresponds to  $10\ \mu\text{m}$

Care was taken that the average length of the filaments was not be below  $10\ \mu\text{m}$  and no bundled actin was observed. Fig. 8.3 shows typical images of an actin sample that can be used for the experiments and samples that should be avoided.

## 8.2.2 Actin Binding Proteins

### Myosin II

Myosin II and N-ethylmaleimide modified heavy meromyosin (NEMHMM) were provided by E. Sackmann (TU München). Myosin II and HMM were prepared following the procedure of Margossian and Lowey<sup>[158]</sup> with additional modifications as described by Hynes *et al.* from rabbit muscle.<sup>[184]</sup> N-ethylmaleimide modified heavy meromyosin (NEMHMM) was prepared as described by Cande.<sup>[185]</sup> N-ethylmaleimide binds to cysteine groups in the active center of the myosin and blocks its ATP activity while the actin binding site remains functional.

NEMHMM was used to provide adhesive points for the actin on the micropillar structure. It was diluted to a concentration of  $5\ \mu\text{M}$  in T-Buffer, was incubated in the flow-cell for 3-5 min and washed out prior to actin binding to the pillars. It adsorbed unspecifically to the pillar tops.

It is known that actin can only hardly be crosslinked by myosin in solution when the myosin is not in its filamentous state. Above KCl concentrations of  $300\ \text{mM}$  the myosin II exists only as single filaments. However, at low concentrations like  $25\ \text{mM}$  KCl, which is the case in the T-buffer, it forms thick bundles. Thus, to

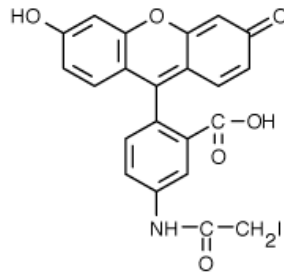


**Figure 8.4:** Structure of 5-iodoacetamidofluorescein (5-IAF).

**Table 8.5:** B-buffer, pH: 7.4 (*MW*: molecular weight, *c*: concentration, *m*: content in 100 ml 1x buffer)

Substance	<i>MW</i> in [g/mol]	<i>c</i> in [mmol/l]	<i>m</i> [mg]
Imidazol	69	25.0	170
EGTA	380	1.0	3.8
MgCl <sub>2</sub> · 6H <sub>2</sub> O	203	4.0	810
KCl	75	600.0	4500

observe crosslink of actin, T-buffer containing 200 mM KCl concentration was used, in which the myosin only assembled to mini-filaments.

To visualize the myosin by fluorescence microscopy, the myosin was fluorescently labeled by 5-iodoacetamidofluorescein (5-IAF, Molecular Probes, Göttingen, Germany) (Fig. 8.4). In the presence of amines and at physiological pH this marker binds covalently to reactive thiol groups of proteins forming thio-ethers. 5-IAF has an absorption maximum at  $\lambda=492$  nm and an emission maximum at  $\lambda=515$  nm. It was shown in literature that the active center remained intact after staining.<sup>[186]</sup> The myosin II was diluted in 300  $\mu$ l B-buffer ("B" for binding) to a concentration of 2 nM. The provided myosin stock contained DTT for the stabilization of the protein that would compete with the binding of the 5-IAF to the thiol groups. Therefore, the diluted myosin was dialyzed in a dialysis cassette (Slid-A-Lyzer, MWCO 7000, Perbio, Bonn) overnight at 4°C in B-Buffer.

Prior to staining, a stock solution, containing 250 mM 5-IAF diluted in B-buffer, was prepared and can be stored at 4°C for several days. For staining, 25  $\mu$ l of this stock were added drop-wise to the myosin solution while stirring. Thereafter an excessive amount of DTT was added to bind unbound 5-IAF in order to remove excessive amount of free 5-IAF in the following dialysis.

To purify the stained myosin it was again dialyzed against B-buffer at 4°C for 2 days. The obtained labeled myosin can be stored at 4°C for several days.

### Filamin

Filamin was provided by E.Sackmann (TU München). It was purified from chicken gizzard as described by Shizuta *et al.*<sup>[187]</sup> For investigation of actin crosslinking it was diluted to a concentration of 400 nM in T-buffer prior to every experiment.

### Alpha Actinin

Alpha actinin was purchased from Sigma-Aldrich. The solution contained 4 mg/ml ammonium sulfate to stabilize the protein. However for crosslinking experiments it had to be dialyzed. 250 µl of the suspension was centrifuged for 30 min at 50.000 g and the precipitate was collected. After removing the supernatant, the actinin was resuspended in 250 µl T-buffer containing 15 mM DTT in order to stabilize the actinin in its natural state. The solution was mixed for 2 hours at 4°C and subsequently dialyzed against T-buffer, containing 0.2 mM DTT and 3 mM NaN<sub>3</sub>, using mini dialysis units (Mini Slide-A-Lyzer, Pierce).

The concentration of the  $\alpha$ -actinin was determined by UV-Vis spectroscopy, using an absorption coefficient ( $\epsilon^{280}$ ) of 1.238 ml/mg.

## 8.3 Microparticles for OT experiments

The polystyrene microparticles were coated with poly-L-lysine prior to their usage. The commercially provided microparticles usually contain negatively charged sulfate moieties that prevent them from clustering. However, this makes them nonadhesive for the also negatively charged actin. Poly-lysine on the contrary is a highly positive charged poly peptide and binds tightly to the negatively charged actin.

First, a solution of 50 µl polystyrene beads with a diameter of 2 µm (Polysciences, Eppenheim) was centrifuged at 11,000 g. The supernatant was discarded and the pellet is resuspended in 50 µl water. This step was repeated for three times. The pellet was again resuspended in Milli-Q water and 10 µl of this solution were added to 90 µl solution which contains 5 mg/ml poly-L-lysine (MW 15,000-30,000; Sigma Aldrich). These functionalized beads were stored at 4°C under continuous agitation

to prevent clustering. Prior to each experiment this solution was washed again in water as described before and resuspended in T-buffer.

## 8.4 Microscopy

### 8.4.1 Light Microscopy

Light microscopy was performed using a Zeiss Axiovert200M (Zeiss, Oberkochen) equipped with a Hamamatsu ORCA-ER camera capable to acquire pictures up to a frame rate of 50 pictures per second. The pictures were taken with a 40x water-immersion objective (Epifluor Apochromat, NA=1.20; Zeiss, Oberkochen). The microscope can either be used in the confocal mode (LSM 5 Pascal) or in the normal light microscopy mode.

### 8.4.2 Optical Tweezers

The whole microscopy setup is based on the Alpha-SNOM platform (Witec, Ulm) and is placed on a damped optical table (Newport, Irvine, CA). The platform is equipped with 2 confocal objectives opposite to each other. However, the beam paths for image acquisition and optical trap are home made. The setup allows control over 3 independent image acquisition systems: the low magnification brightfield setup, the fluorescence setup and the high speed high magnification brightfield setup. This allows to visualize simultaneously actin and high speed particle tracking within the experiment. The following describes the single visualization systems briefly:

- Low-magnification brightfield setup: Used for a visible overview of the channel. A narrow band red LED (Collimated Red LED, LEDC28; Thorlabs, Newton, NY) which is emitting light at the wavelength 630nm is coupled into the light path and the picture is taken by an AxioCam (Zeiss, Oberkochen) at the upright part of the microscope by using a 2.5x objective (Plan Neofluar; Zeiss, Oberkochen). During high speed acquisition the objective is replaced by a 20x objective (Plan Neofluar, Zeiss, Oberkochen).
- High-magnification setup: Used for particle tracking. The red LED illuminates the sample in transmission mode through filters to a high-speed camera

(Phantom V7.2, Vision Research, Wayne, NY). The camera is coupled to the fluorescence image recording to allow synchronized image recording.

- Fluorescence setup: Used for stained actin visualization: A 50 mW diode laser (VA-Serie; Roithner Laser Technik, Wien, Austria) is coupled via a dichroic mirror (550 nm cut-off) into the light path. It is focused into the back focal plane of a 60x water immersion objective (Universal Plan Apochromat 60x, NA=1.2, W3, IR; Olympus, Center Valley, PA) at the lower part of the microscope. The images are visualized by a Retiga EX (QImaging, Surrey, Canada). The laser is triggered by the camera which allowed only illumination at the acquisition times of the camera without illumination at the read-out times to reduce fluorophore bleaching. The laser frequency is 30 Hz. The image is reflected through a 593 nm bandpass filter (HC Beamsplitter BS593; AHF Analysentechnik, Tübingen) to the camera. A system of filter sets protects the camera from the the light of the transmitted LED, the green light and from the IR light of the laser for the optical trap at reasonable signal-to-noise ratio.

The optical trap is generated by a 5 W solid state NdYVO<sub>4</sub> laser (J20-BL-106C, Spectra Physics, Mountain View, CA) which is emitting planar polarized light at 1064 nm. IR-lasers are commonly used to reduce photo damage in biological samples and to prevent heating of the sample. The laser is focussed into the object plane through the 60x objective. Stable trapping can be achieved at depths above 50  $\mu\text{m}$ . Fig. 8.5 shows the whole system again schematically.

The alphaSNOM mounting stage which provides manual adjustment in x- and y-direction is coupled with a piezo controlled stage (Physik Instrumente, Karlsruhe). Except for the Phantom camera and the Axiocam, all electronic parts are controlled by several LabView routines (LabVIEW v.8.2, National Instruments, Austin, TX). The routines also provide real-time imaging processing for the fluorescent image. The particles were detected by a home-written program in MATLAB using tracking routines developed by J.C. Crocker and D. Grier<sup>[71]</sup>, originally written in IDL and transferred to MATLAB code by D. Blair and E. Dufresne. (Download: <http://physics.georgetown.edu/matlab/>). The images were processed to reduce background signals. Then a two dimensional gaussian profile was fitted to the images. The microparticles had a gaussian profile in brightfield. This allowed for the localization of the beads' centers in subpixel resolution.

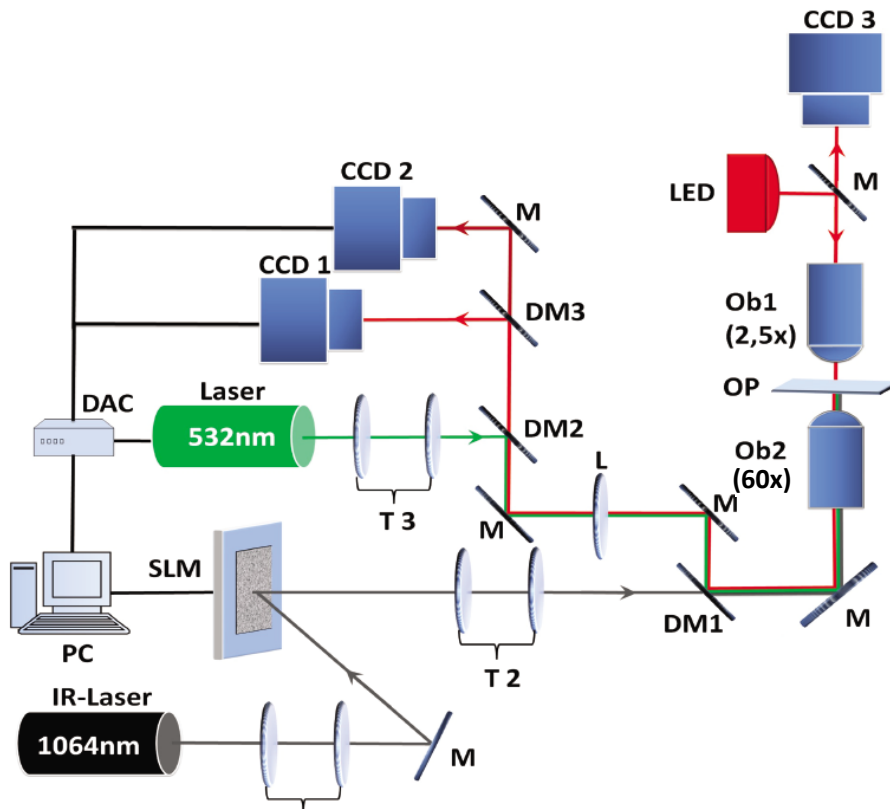


**Figure 8.5:** Complete optical tweezers setup. The optical trap is created by the IR laser which is focussed into the back focal plane of the objective Ob2. The dichroic mirror DM1 transmits above 950 nm. The green laser (excitation 532 nm) is reflected by DM2 and DM1 and is focussed in the back focal plane of Ob2. The emitted fluorescence is passing DM2 and reflected by DM3 into CC1. For high speed bright field recording the LED is transmitting light at 633 nm through the object, reflected by DM1 and passing DM2 and DM3 and recorded by CCD2. Low magnification bright field imaging is achieved with CCD3 which records the reflected light from the LED. The cameras, the green laser and the object stage are synchronized via a data acquisition card (DAC) connected to a computer. Scheme with courtesy of Kai Uhrig.



## Biomimetic of quasi 2-dimensional Actin Networks on PDMS-Micropillars

The actin cytoskeleton of a cell consists of two types of networks. A three dimensional one in the cytoplasm, built up by microtubules, intermediate filaments and actin, which gives the cell gel-like properties, and the actin cortex. The actin cortex is a flat thin filamentous actin network, crosslinked to bundles forming various angles, and attached point-wise to the cell membrane.<sup>[104]</sup> It can spread over tens of square-micrometers but only has a thickness of about 200 nm. So it can be considered as a quasi two-dimensional network. It gives the cell its shape and acts as an important mechanosensor for the cell. Many studies on the mechanical properties and crosslink behavior of the actin cytoskeleton have been only addressed to three-dimensional networks.<sup>[111,112,188-192]</sup> Others only considered single filament mechanics.<sup>[33,193-197]</sup> However, there is evidence, that the mechanical properties of viscoelastic two-dimensional networks differ from that in bulk. There are only a few studies taking the quasi two-dimensional appearance of the actin cortex into account.<sup>[198-200]</sup>

A strategy to create a free dangling quasi two-dimensional, self assembled actin networks, which additionally mimics the point-like anchorage to the cell membrane, was presented by Roos.<sup>[7]</sup> He anchored and crosslinked filamentous actin on an array of silicon pillars. We followed this strategy and improved the system.

The micropillar arrays were microfabricated from poly-dimethyl-siloxane (PDMS), a transparent, non-toxic, non-fluorescent, elastic polymer. The pillars exhibited a diameter between 5-10  $\mu\text{m}$ , a height of 15  $\mu\text{m}$  and a inter-pillar distance between

5-11  $\mu\text{m}$ . The pillar tops were biofunctionalized for local anchorage of the actin filaments. Due to the inter-pillar distance, which was below the contour length of the filaments, physisorption of the filaments to the surface between the pillars was prevented.

We developed a microfluidic system which allowed us both to provide a constant chemical environment at very low consumption of the desired proteins (volume of the reaction chamber was  $\sim 1.5 \mu\text{l}$ ) and a defined flow speed. Subsequently, the free dangling actin network was crosslinked by either filamin, magnesium ions, calcium ions, myosin II or  $\alpha$ -actinin.

In this study we presented quasi two-dimensional self assembled crosslinked actin networks. Moreover, the feasibility of our transparent setup, to follow the bundling dynamics of F-actin in real time, is demonstrated. We observed so-called zipping events where two free dangling filaments, which were locally defined by their anchorage to the pillars, bundled in a zip-like manner.

## 9.1 Actin Network Assembly in a Flow-cell

To build up a two dimensional network on the micropillars a flow-cell containing the desired PDMS-microstructure was assembled as described in chapter 8.1.

To exchange the solutions with a controlled speed easily, the outlet of the flow-cell was attached to a syringe pump. First the flow-cell was filled with a solution containing 30% ethanol in Milli-Q water to remove trapped air. After that the cell was rinsed with T-buffer. Then the pillar heads were functionalized with N-ethylmaleimid modified heavy meromyosin (NEMHMM, 5  $\mu\text{M}$  in T-buffer, 3-5 min). NEMHMM is able to bind actin, however lacks its motor activity.<sup>[185]</sup> The NEMHMM adsorbed unspecifically only to the pillar tops due to the superhydrophobic character of the PDMS.<sup>[201]</sup> The flow-channel was again rinsed with T-buffer to remove excessive NEMHMM. Then a freshly prepared F-actin solution, diluted to 50 nM F-actin in T-buffer, was slowly sucked into the flow-cell and incubated for 10 min. The flow should be very slow to guarantee the formation of a two-dimensional network. After that the cell was rinsed slowly with T-buffer. The desired solutions, e.g. crosslinker, were then applied. Fig. 9.1 shows again a schematic drawing of the assembly of F-actin to a micropillar array. A typical example of a so-constructed network is shown in Fig. 9.2.

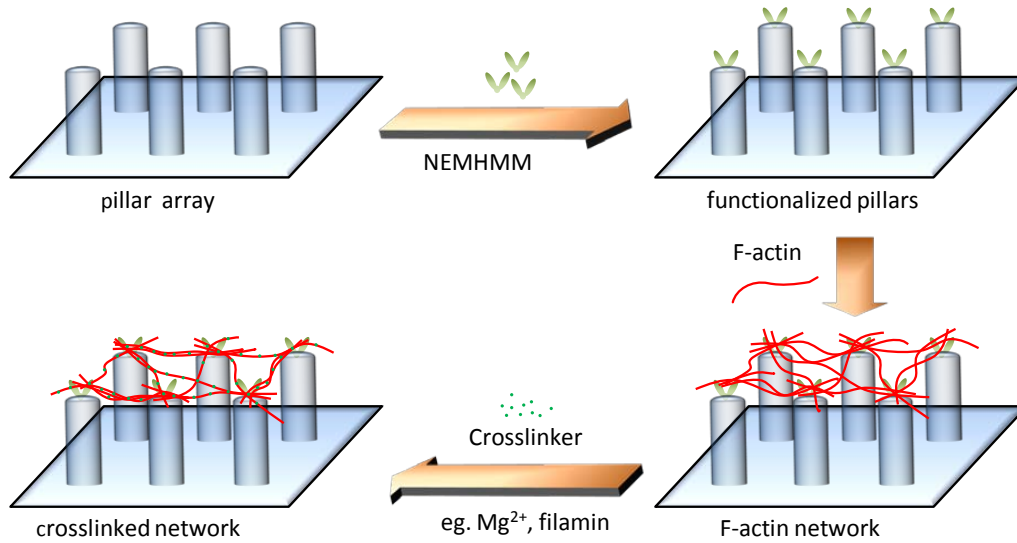


**Figure 9.1:** Schematic view for the assembly of a quasi 2-dimensional F-actin network on micropillars. First the pillar heads are functionalized with NEMHMM. Then actin is added which grafts specifically to the pillar tops. Thereafter the network can be crosslinked.

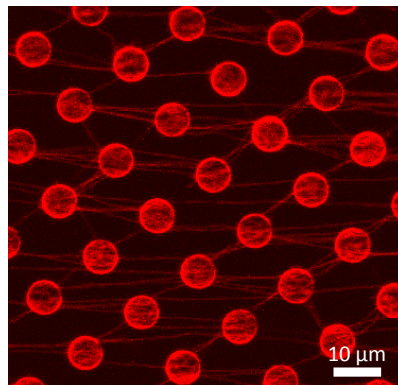


**Figure 9.2:** A typical network of F-actin stained with phalloidin-TRITC on PDMS-micropillars. The single filaments are grafted on one or more sites to the pillar tops. Between the pillars they dangle free and can fluctuate. The image is made by confocal microscopy. The scale bar corresponds to 20  $\mu\text{m}$ .

In the following we always refer to such preassembled actin networks.

## 9.2 Crosslinked actin networks

There are many actin binding proteins known. Proteins like tropomodulin and CapZ are actin capping proteins to inhibit polymerization and depolymerization. Gelsolin severs actin and there are actin binding proteins that form crosslinks. Therefore

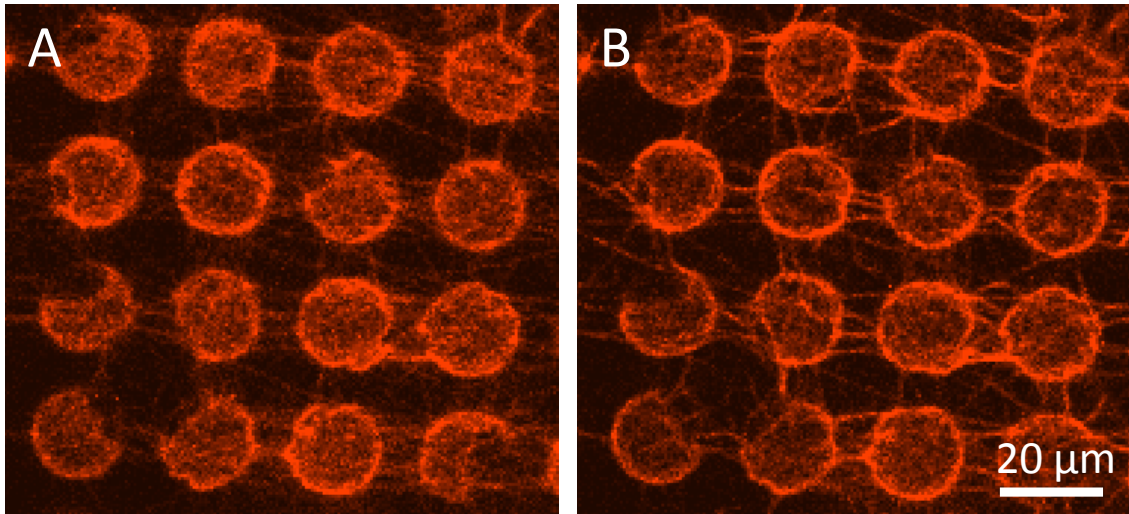


**Figure 9.3:** Actin crosslink mediated by filamin. (A) shows the free pending actin network on the pillar tops. The single filaments occur blurry due to fluctuation in the flow. After adding filamin the actin is crosslinked (B). Noticeable is the tendency of filamin to form "Y"-like crosslinks. The images are made by confocal microscopy. The scale bar is 20  $\mu\text{m}$ .

they have to bind to 2 moieties on two different actin fibers. The most prominent members amongst them are myosin, filamin,  $\alpha$ -actinin and ARP2/3. Additionally divalent or multivalent cations like magnesium or calcium ions are known to mediate crosslinks above a certain concentration as well.

Here we show the successful assembly of crosslinked 2-dimensional F-actin networks on PDMS micropillar substrates mediated by filamin, magnesium ions and myosin II. While filamin and divalent cations formed so-called passive networks, myosin networks could be disassembled again by adding ATP.

### 9.2.1 Filamin

Filamin is a dimeric protein with a fork-like structure with one actin binding site on each monomer and plays an important role in cell mechanics and signalling.<sup>[137,202,203]</sup> Filamin was diluted to a concentration of 500 nM in T-buffer and injected into the cell. A formation of a quasi-two dimensional network was observed (Fig. 9.3 (B)) The filaments were crosslinked and formed bundles. Fig. 9.3 (A) shows the unbundled actin network before injection of filamin. The filaments were blurry due to their fluctuations in the flow.

## 9.2.2 Divalent Cations

In contrast to proteins, magnesium ions are present everywhere in the cell. Actin is a highly negatively charged polymer. It attracts cations from the solution, which increases the local concentration of counterions on the filament. The Manning counterion condensation theory describes this phenomenon.<sup>[204]</sup> Fluctuations in the counterion charge shielding could overcome the actin's electrostatic repulsion and lead to long range attractions of the actin.<sup>[205–207]</sup> Since divalent cations are present in the cell in the micromolar range, it could be shown, that this bundling may also play an important role in cells.<sup>[206,208]</sup> It was observed by confocal microscopy and small-angle x-ray scattering that an increasing concentration of alkali metals resulted in an increased charge shielding of the actin filaments.<sup>[209]</sup> In 1996 Tang *et al.* found out, that a threshold concentration of polycations is required for bundling and that it is dependent on the valence of the cation.<sup>[206]</sup> They performed light scattering experiments on several cation containing actin solutions. It was shown, that magnesium ions above a concentration of 12 mM are able to form actin bundles.<sup>[210]</sup> Contrary, in our experiments performed with F-actin on pillar tops, we found that a concentration of 14 mM  $Mg^{2+}$  was at least needed to form bundles.<sup>[211]</sup>

To create a network of actin bundles crosslinked by  $Mg^{2+}$ , T-buffer containing 80 mM  $Mg^{2+}$  was added to the network. A formation of a two-dimensional network containing thick bundles was observed. While the grafted F-actin dangling freely from the pillar tops were fluctuating in the flow (Fig. 9.4 (A)) a stiffening resulted by the bundle formation by  $Mg^{2+}$  was observed.

Bundled networks crosslinked by calcium ions appeared similar.

While filamin and magnesium ions are rather considered as passive crosslinkers we also established crosslinked networks of active myosin II on the pillar arrays.

## 9.2.3 Myosin II

Myosin II is an ubiquitously found protein in cells. It plays the major role in force production in the muscle cells and it is also pivotal for cell's maintenance.<sup>[106]</sup> It is dimeric active motor protein with two heavy and two light chains. The heavy chain consists of a head region, which contains the binding site for actin and ATP a neck and a tail region. The tail regions can form bundles below a concentration of 300 mM KCl. Above this concentration myosin II is present as a dimer.

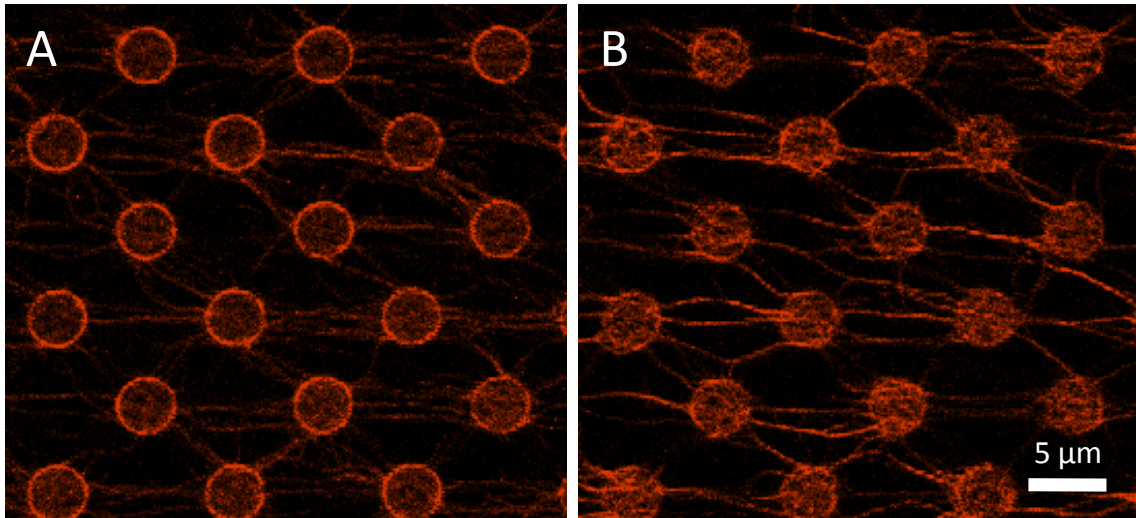


**Figure 9.4:** Formation of a quasi-two-dimensional F-actin network on micropillars. The F-actin filaments grafted to the pillar tops are fluctuating in the flow (A). After addition of 80 mM  $Mg^{2+}$  a bundled network is assembled on the pillar tops. The scale bar is 20  $\mu m$ .

In the experiments presented here, an intermediate state of myosin II organization is used. At KCl concentrations of 200 mM myosin II forms mini-filaments whereas at lower salt concentrations the myosin II clusters to big bundles which are unable to crosslink the actin in a defined way. The mini-filaments, which consist of a few myosin dimers, can act as a crosslinker for F-actin.

To visualize the myosin II besides the actin it was stained with 5-iodoacetamido-fluorescein. The fluorescent myosin II was diluted to a concentration of 400 nM in T-buffer, containing 200 mM KCl. After applying this solution to the actin containing flow-cell bundle formation was observed. Merging the two different fluorescent signals (Fig.9.5 (C)) it was seen that the myosin and the actin were colocalized. The networks formed appeared similar to that formed by filamin.

Also dynamic unbundling of actin, crosslinked by myosin, could be performed by adding 100 mM ATP in T-buffer, containing 200 mM KCl, to the flow-cell (Fig. 9.6). Without ATP, myosin binds to actin, but can not dissociate (*rigor state*). With ATP present, there is a dynamic situation between association and dissociation, of which the latter process proceeds with a force stroke. However, the set-up presented here did not have a sufficient spatial and temporal resolution to image this force stroke. After dissociation of myosin II from the actin filament, the myosin could easily diffuse away. Due to the three-dimensional flow chamber used in the experiments presented here, there was a negligible chance that the myosin II associated

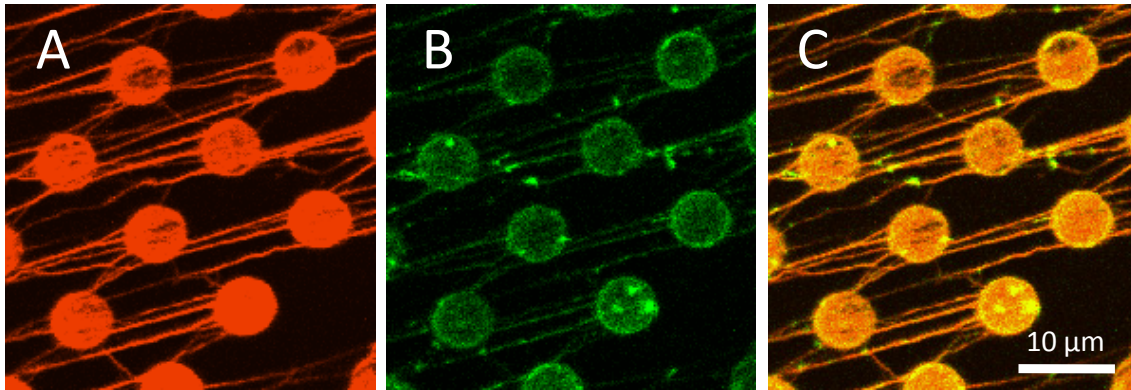


**Figure 9.5:** Network of actin (red) crosslinked by fluorescent myosin II (green). (A) shows thick actin bundles which are crosslinked by fluorescent myosin II (B). The merged image in (C) confirms the correlation between actin and crosslinker. The scale bar is 10  $\mu\text{m}$ .

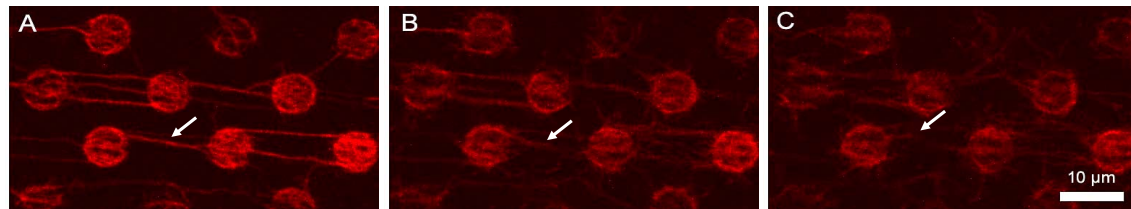


**Figure 9.6:** Unbundling of with myosin crosslinked actin, initialized by adding 1 mM ATP. (A) shows the actin bundled by myosin II. After injection of ATP to the right side of the channel proceeding bundle disassembly is observed, which is indicated by the white arrows in (B) and (C). The scale bar corresponds 10  $\mu\text{m}$ .

again to the actin filament. Even when they rebound, force strokes were produced again and subsequently the myosin mini-filament could diffuse away.

The ATP was injected at the right side of Fig. 9.6 (A). The white arrow indicates the actin unbundling.

It was seen that the bundle was made up of several single actin filaments. These experiments show, that variations in the ATP concentration can be used as a switch to turn crosslinking of actin filaments by myosin II on and off. Turning cross-linking on can either be done by removing the ATP in solution by using a flow or by waiting for depletion of all the present ATP. The latter will also result in the formation of cross-links as has been shown for filaments in bulk.<sup>[212]</sup> Turning crosslinking off can be done by addition of ATP, as shown in bulk<sup>[213]</sup> and in two dimensions in the experiments discussed here.

During the bundling process of actin with fluorescent myosin II so-called zipping events were observed (Fig. 9.7). Two actin filaments, which were attached at one

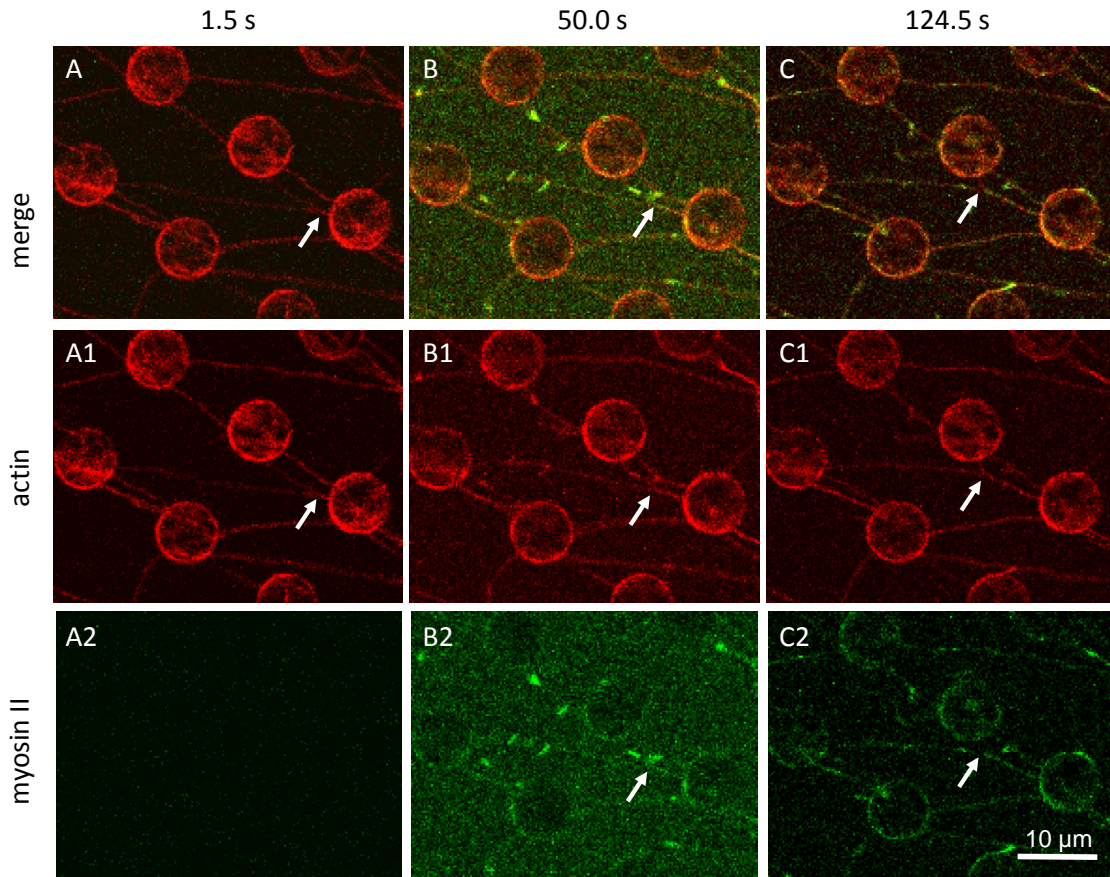


**Figure 9.7:** Actin zipping mediated by fluorescent myosin II. Two free dangling filaments (red) start to zip by increasing the concentration 5-IAF labeled myosin II (green) continuously to 400 nM (arrow in (A)). The zipping (arrow in (B)) propagates to its end point (arrow in (C)). Images (A1-C1) only show the red actin channel and in (A2-C2) only the green myosin channel is visible corresponding to (A-C) respectively, which indicates the correlation between actin and myosin crosslinker. The scale bar is 10  $\mu\text{m}$ .

side attached to the same pillar (Fig. 9.7 (A), white arrow) were covered by fluorescent myosin II by increasing the crosslinker's concentration slowly to 400 nM. The myosin was again diluted in T-buffer, containing 200 mM KCl. The bundling started from the point where the actin filaments came in close contact (Fig. 9.7 (B), white arrow). The zipping ended at a point where the geometrical constraints and/or forces, that acted on the actin filaments stopped the bundling (Fig. 9.7 (C), white arrow, also indicating the correlation between actin (red) and myosin (green)).

This observations motivated us to investigate the zipping phenomenon more in detail. This is the topic of the next section.

## 9.3 Actin Zipping

In biological context the most known example of zipping occurs in the case of DNA where proteins unzip the double strands to single strands. This is a widely investigated field in science.<sup>[214–216]</sup> Various unzipping forces related to the DNA sequence could be observed by optical tweezers.<sup>[217]</sup> However, DNA strands are rather flexible compared to actin filaments. Zipping was also observed and quantified for hemoglobin-S-fibers.<sup>[218]</sup>

Here, we present for the first time a biomimetic tool to follow the bundling kinetics of quasi two-dimensional actin networks *in vitro* in an extremely simplified biomimetic system.

The implementation of the micropillars to the closed flow-cell system in combination with fluorescence microscopy allowed us to observe bundling events in real time with full control over the biochemical environment provided for the network.

The free dangling actin filaments were trapped with defined boundary conditions by local anchorage to the pillar tops. With that, surface interaction could be prevented as well.

If a crosslinker is present in the flow-cell and the filaments come close enough

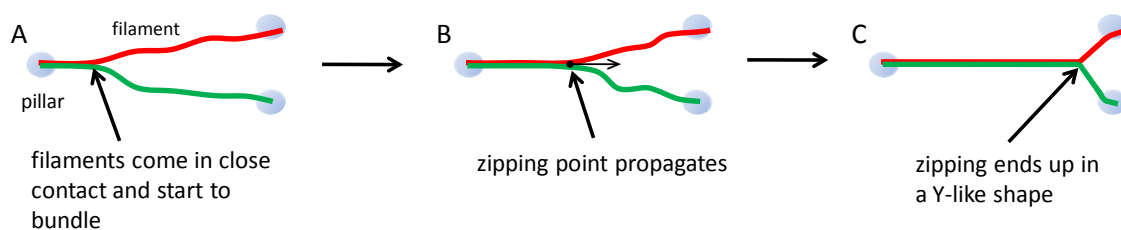


**Figure 9.8:** Schematic drawing of filament zipping. If crosslinkers are present the filaments start to bundle when they come to a close contact (A). The bundling propagates in a zip-like manner (B), ending up in a "Y"-like shape (C), which in this case is only limited by the contour lengths of the two filaments.

together by thermal fluctuations they begin to crosslink. At this point the fluctuations decay and further crosslinking is enhanced. This zipping process propagates until the contour length of the participating filaments is used up<sup>1</sup>. Depending on their anchorage positions on the pillar tops this could end up in a "Y"-like shape

<sup>1</sup>This is not completely right. The end point of zipping and therefore the configuration of the zipping is influenced by other mechanical and entropic effects as well which will be discussed later in this section. For the moment we only refer to the geometrical configuration.

(Fig. 9.8).

Fig. 9.9<sup>2</sup> shows an actin zipping initialized by 20 mM  $Mg^{2+}$  in T-buffer. In Fig. 9.9

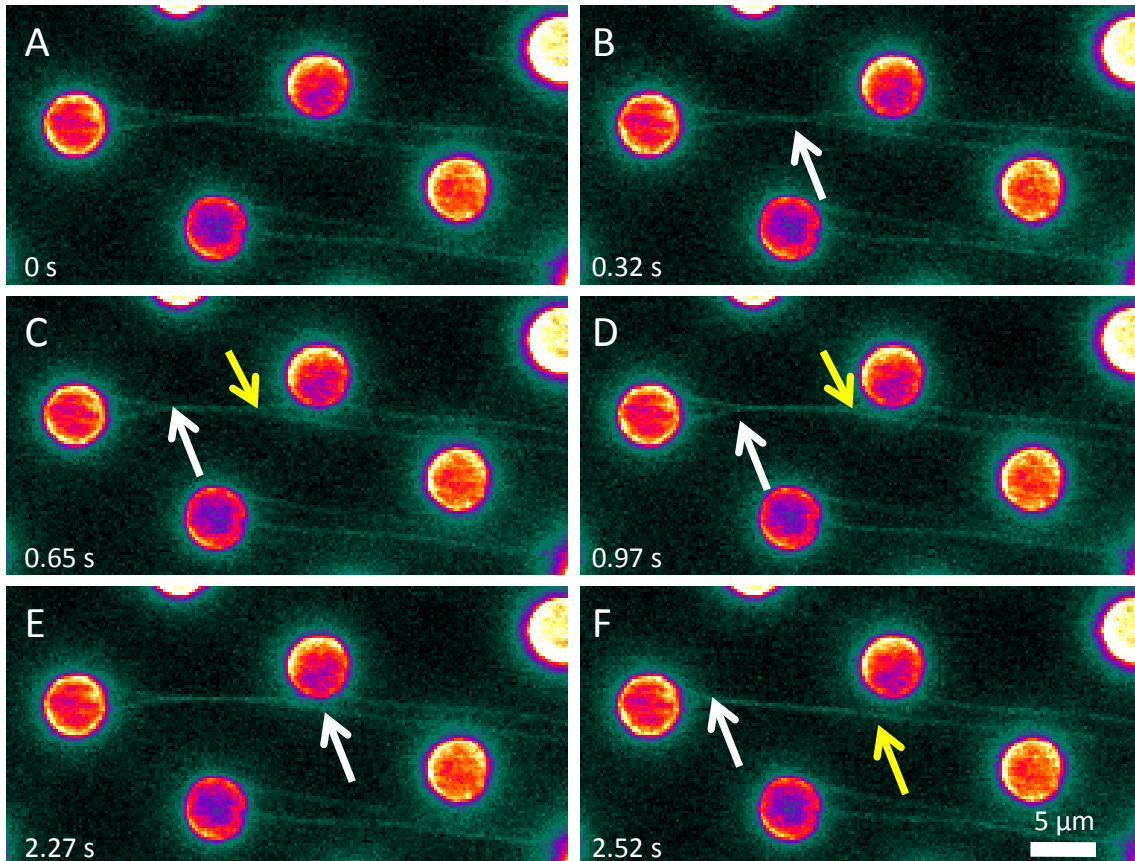


**Figure 9.9:** Series of images showing the actin zipping mediated by 20 mM  $Mg^{2+}$ . Through fluctuations in the flow the two crossed, free dangling filaments in (A) come close together to undergo crosslinking which starts around the point indicated by the arrow in (B). The zipping propagates on both sides to two points (arrows in (C) and (D)). In (E) the upper filament detaches from the pillar (arrow in (E) and yellow arrow in (F)). Released tension from the lower filament results in further propagation of the zipping point (white arrow in (F)). The picture is pseudo-colored for better visibility of the filaments. The scale bar is 5  $\mu\text{m}$ .

(A) two actin filaments were grafted to the same pillar on one end and to different pillars on the other end, crossing each other. After injecting the  $Mg^{2+}$  to the flow-cell, bundling started at the crossing point (Fig. 9.9 (B), white arrow). The zipping points propagated in two directions at 6-8  $\mu\text{m/s}$  to the opposite ends of the filaments (Fig. 9.9 (C), arrows) until they stopped due to the tension from bundling

<sup>2</sup>These and the following images in this chapter are made by fluorescence microscopy. The images were inverted and/or graphically enhanced for better actin visibility.

applied to the filaments (Fig. 9.9 (D), arrows). In Fig. 9.9 (E) the upper filament was released from the pillar (white arrow) resulting in released tension to the lower filament (yellow arrow in Fig. 9.9 (F)) and further propagation of the zipping point to the anchorage points of the filaments (white arrow in Fig. 9.9 (F)).

Dynamic filament zipping could be observed on quasi two-dimensional actin networks for all crosslinkers used in this study. This opens up the possibility to studies on a wide range of applications.

Fig. 9.10 shows an actin network crosslinked by injecting 750 nM  $\alpha$ -actinin in T-

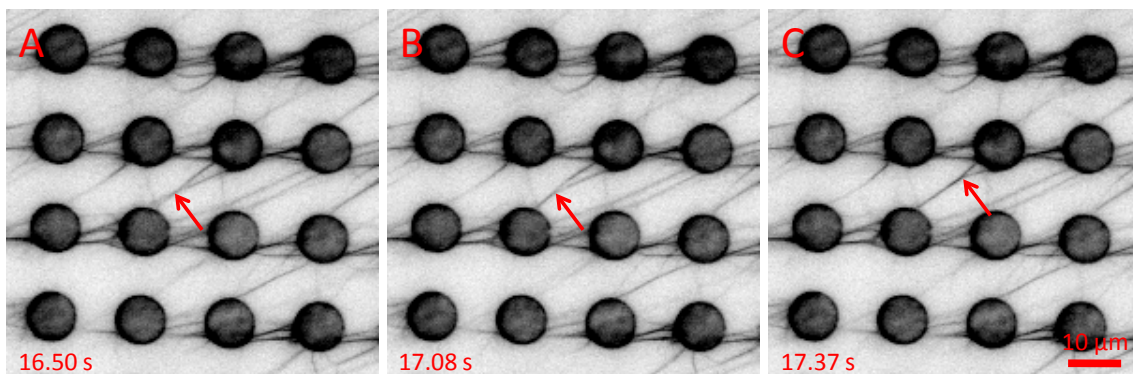


**Figure 9.10:** Dynamic bundling of actin by  $\alpha$ -actinin (A). Two actin filaments are in close contact (red arrow). After injection of 750 nM  $\alpha$ -actinin, the bundling starts at the point indicated by the red arrow in (B). The zipping propagates to the point where the forces are balanced (red arrow in (C)). The scale bar corresponds to 10  $\mu\text{m}$ .

buffer to the flow-cell. Again the crosslinking started at the point where the filaments came in close contact (Fig. 9.10 (A), red arrow), propagated (Fig. 9.10 (B), red arrow) and stopped at the balance of the forces (Fig. 9.10 (C)). The velocity of propagation of the zipping point was measured to be about 15  $\mu\text{m}/\text{s}$ .

In Fig. 9.11 400 nM filamin diluted in T-buffer mediated the bundling. Two actin filaments were closely grafted to the same pillar (Fig. 9.11 (A), orange arrow). After injecting of the filamin they zipped together (Fig. 9.11 (B), orange arrow). During the injection there was a strong flow in the direction of the blue arrow (Fig. 9.11 (A)), resulting in bending of the actin in the direction of this flow. The flow speed was unknown but resulted it prevented the mentioned actin filaments from complete zipping along their contour lengths. Whereas the filaments indicated by the right arrow in Fig. 9.11 (B) were close enough to each other to zip even against this flow (red arrows in Fig. 9.11 (D-F)). The propagation speed of the bundling point was measured to be only around 3.5  $\mu\text{m}/\text{sec}$ .

We also saw successive dynamic bundling of F-actin by first injecting 40 mM  $Mg^{2+}$

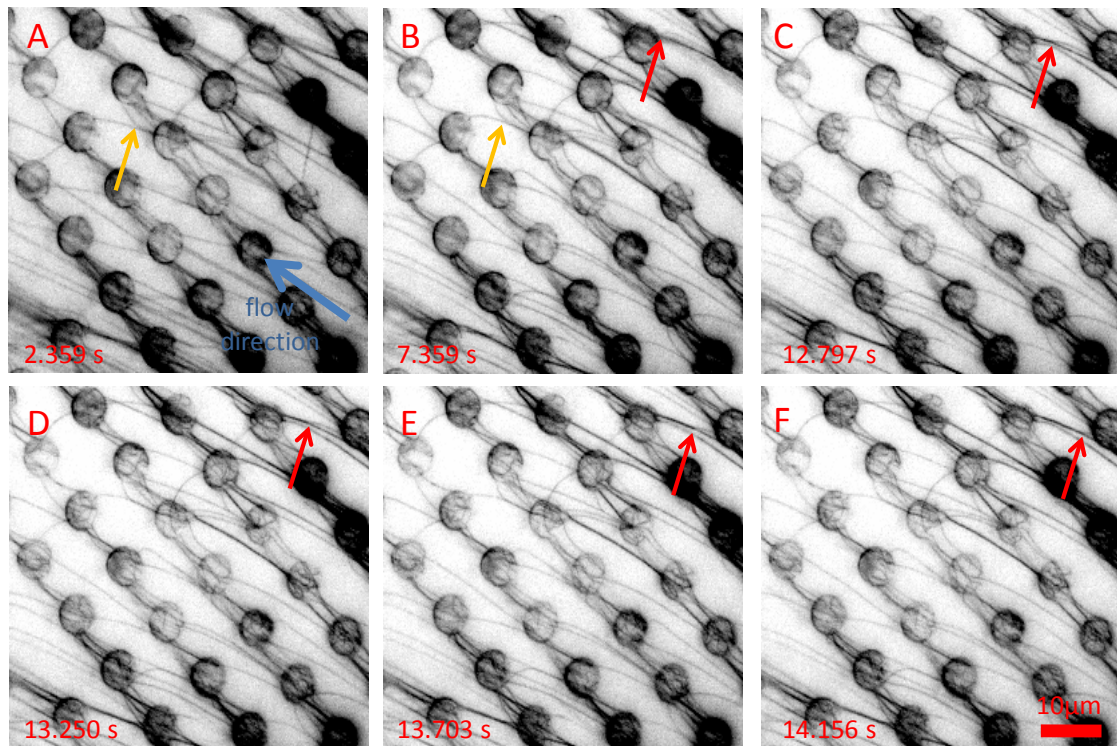


**Figure 9.11:** Dynamic actin bundling by filamin. Two actin filaments which are close together (arrow in (A)) bundle in a zip-like manner after injection of filamin (red arrow in (B)). The strong flow (blue arrow) in the cell generates bending of filaments in the flow direction. However, the filaments indicated by the right red arrow in (B) are close enough to bundle against the flow (D-F). The scale bar corresponds to 10  $\mu\text{m}$ .

in T-buffer and, thereafter, adding T-buffer containing 80 mM  $Mg^{2+}$ .

Fig. 9.12 shows two actin bundles crosslinked by 40 mM  $Mg^{2+}$ . Each bundle lever contained about 5-10 filaments. These bundles were significantly stiffer than single filaments. This stiffness worked against the bundling force. The zipping point was not determined only by the contour length of the filaments (red arrow in Fig. 9.12 (A)). By increasing the concentration of  $Mg^{2+}$  to 80 mM the length of the zipped part grew (red arrow in Fig. 9.12 (B)) to its new equilibrium point (red arrow in Fig. 9.12 (C)). The propagation velocity measured to  $\sim 2 \mu\text{m/s}$  was significantly lower than that for bundling of single filaments (Fig. 9.12 (D)).

These observations show the interplay between attractive force, which is the adhesion force, and the repelling force, which is here the bending stiffness of the bundle. However, the number of bundles was undefined. Inspired by this result we were

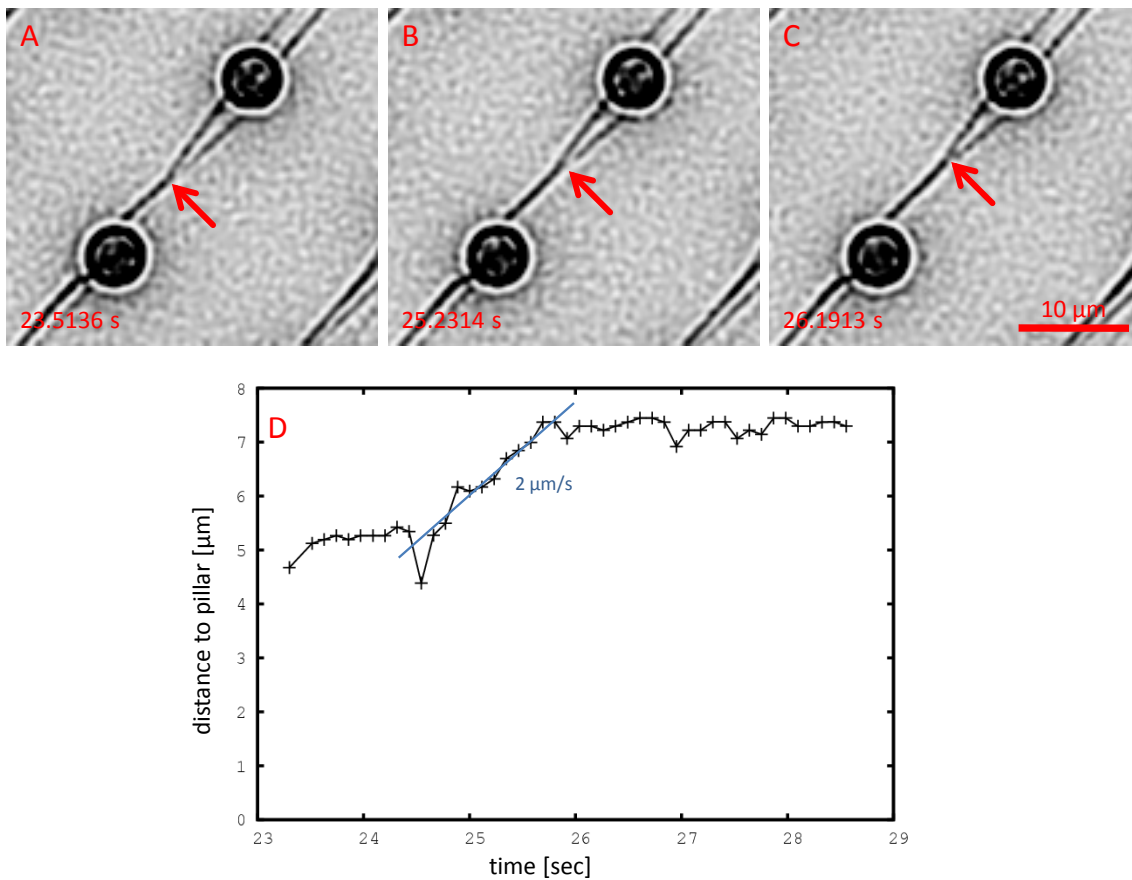


**Figure 9.12:** Propagation of zipping caused by increased ion concentration. Two bundles of actin, each consisting of 5-10 filaments are zipped to the point indicated by the red arrow in (A) by 40 mM  $Mg^{2+}$ . By increasing the ion concentration to 80 mM, the zipping point propagates (B) to its equilibrium point (C). The velocity of the zipping point is  $\sim 2 \mu\text{m/s}$  (D). The distance is measured to the pillar from where the zipping starts. The scale bar is 10  $\mu\text{m}$ .

interested if we could derive quantitative data for the adhesion forces between two zipped actin filaments.

### 9.3.1 The Theory of Zipping

In the recent years Kierfeld *et al.* published several theoretical works to describe phase transitions in the unbundling and desorption process of semiflexible polymers.<sup>[219-221]</sup> They described equilibrium phase transitions during bundle formation as well.<sup>[222]</sup> Based on this work and inspired by our biomimetic system, which has

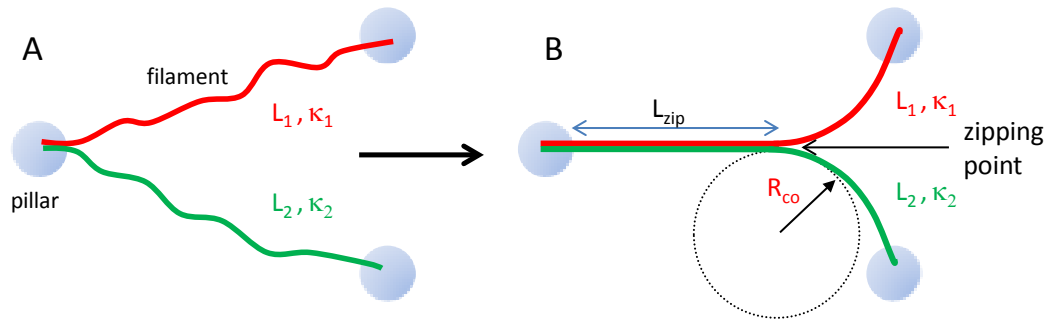


**Figure 9.13:** Schematic drawing of filament zipping. (A) Two filaments with the lengths  $L_1$  and  $L_2$  and the bending stiffness  $\kappa_1$  and  $\kappa_2$  are anchored on the pillar. While zipping the filaments are deformed. The zipping point propagates to a point where the attractive and repulsive forces are equilibrated. This results in a curvature of the filaments at this point. The radius of curvature  $R_{co}$  gives a hint on the dominating forces.

defined boundary conditions while the filaments are unaffected by surface interaction, Gutjahr developed a theoretical description for the parameters needed to derive interfilament attraction forces from our system in her PhD thesis.<sup>[223]</sup> The model she developed to estimate the attractive interaction, based on a similar method as presented by Jones *et al.* in 2005 who investigated and theoretically described interaction forces between hemoglobin-S fibers.<sup>[218]</sup>

In the following a brief description will be given to extract attraction forces  $|W_{zip}|$  on zipped actin filaments from experimental data.<sup>[223]</sup>

Actin filaments are semiflexible polymers which have a persistence length  $l_p$  and a bending stiffness  $\kappa$ . The bending stiffness  $\kappa$  is correlated to  $l_p$  via

$$l_p = \frac{\kappa}{k_B T} \quad (9.1)$$

where  $k_b$  is the Boltzmann constant and  $T$  is the temperature in Kelvin<sup>3</sup>.

First it is assumed that two filaments are grafted on one side to the same position on one pillar whereas their other ends are fixed on different pillars, respectively (Fig. 9.13 (A)). They have the length  $L_1$  and  $L_2$  (which have to be determined in the experiment before zipping (!) and which are the contour lengths between the anchoring points) and a bending stiffness of  $\kappa_1$  and  $\kappa_2$ .

The contour lengths  $L_1$  and  $L_2$  both have to be smaller than their persistence lengths  $L_p$ . If a crosslinker is present they zip together to a certain point (Fig. 9.13 (B)).

<sup>3</sup>For example for actin having a persistence length of  $12 \mu\text{m}$  at RT ( $T=298 \text{ K}$ ) and  $k_B = 1,38 \times 10^{-23} \text{ J/K}$ , its bending stiffness is calculated to  $\kappa = 4,93 \times 10^{-26} \text{ Nm}^2$ .

The length  $L_{zip}$  is defined as the length of this bundling which is from the position where the filaments are anchored together on one pillar, to the end point of the crosslinking. This zipping results in a deformation of the filaments, which increases by increasing adhesion length  $L_{zip}$ . Hence there is an energy gain  $-|W_{zip}|L_{zip}$  by the attraction of the filaments mediated by the crosslinker and an energy loss generated by the bending of the filaments with the bending stiffness  $\kappa_1$  and  $\kappa_2$  and the entropy which is working against the attraction.

The conformation of such a crosslink depends on many parameters, e.g. the length of the filaments, their stiffness, the strength of the attraction, the pillar position. Thus, to get a rough idea, the crosslinks' conformations are classified into two scenarios: regime of weak attraction and regime of strong attraction dependent on the bending stiffness of the filaments.

In the regime of weak attraction, the energy loss is generated by the bending of the filaments dominates, whereas, in the regime of strong attraction, the energy loss through entropy dominates.<sup>[223]</sup> The curvatures of the filaments at the equilibrium point of the zipping give a hint on the dominating energy contribution. The radius  $R_{co}$  of a circle fitted to the curvature of the filaments at this point is proportional to the square root of the bending stiffness  $\kappa$  divided by the attraction force  $|W_{zip}|$

$$R_{co} \sim \sqrt{\frac{\kappa}{|W_{zip}|}} \quad (9.2)$$

As mentioned at regime of weak attraction the bending stiffness works against the deformation and costs binding energy. This results in a rounded "Y"-configuration (Fig. 9.14 (A)). This means the contact radius  $R_{co}$  is bigger than the contour length  $L$  of the filaments.

$$R_{co} \sim \sqrt{\frac{\kappa}{|W_{zip}|}} \gg L \quad (9.3)$$

Therefore the attraction force between the filaments  $|W_{zip}|$  can be derived from fitting exactly the curved filament configuration and measuring the bending radius  $R_{co}$ , or from determination of the exact zipping length  $L_{zip}$ .<sup>[223]</sup>

In the regime of strong attraction the entropy is working against the full stretching of the filaments. The filaments fluctuate around the "Y"-shaped configuration (Fig. 9.14 (B)). The contact radius  $R_{co}$  is small compared to the length of the fila-

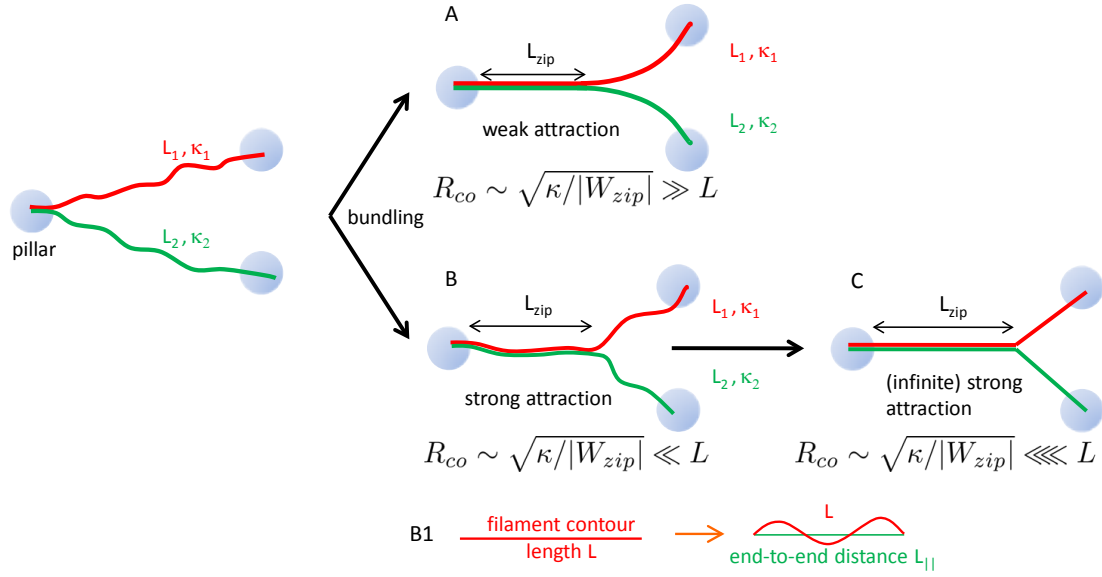


**Figure 9.14:** Schematic drawing of different regimes possible during filament zipping. [223] During bundling of anchored filaments with the lengths  $L_1$  and  $L_2$  and the bending stiffness  $\kappa_1$  and  $\kappa_2$  the filaments are deformed resulting in energy loss by both the bending and the entropy which work against the attractive forces of the bundling. In principle two regimes are possible for bundle formation depending on which of the repulsive forces dominate: (A) If the filaments have a high stiffness the loss by bending energy dominates, resulting in a curved "Y"-shape configuration and a therefore a high radius of curvature  $R_{co}$ . (B) if the entropy dominates as the repulsive force, the radius of curvature at the zipping point at the equilibrium is small. The filaments fluctuate around the "Y"-shaped configuration (B1). If the attraction is much higher than the repulsive forces the configuration ends up in a pure geometrical regime (C). No visible curvature and fluctuations occur.

ments.

$$R_{co} \sim \sqrt{\frac{\kappa}{|W_{zip}|}} \ll L \quad (9.4)$$

Therefore an additional parameter has to be considered which is the end-to-end distance  $L_{||}$  of the filaments which is the direct connection between the end points around which the filaments fluctuate (Fig. 9.13 (B1)). Thus, in this case the exact value of the difference between  $L$  and  $L_{||}$  has to be determined to derive the attractive force  $|W_{zip}|$  between the filaments. [223]

However if the attraction is much stronger (or infinite) than the entropy no fluctuations are visible any more. The contact radius  $R_{co}$  is much smaller or even infinitely

small in contrast to the filament length  $L$  (Fig. 9.14 (C)).<sup>[223]</sup>

$$R_{co} \sim \sqrt{\frac{\kappa}{|W_{zip}|}} \lll L \quad (9.5)$$

The zipping ends up in an "Y"-configuration with sharp edges (Fig. 9.14 (C)). The filament configuration in this case depends only on the geometry of the pillars and the contour lengths of the filaments  $L_1$  and  $L_2$ . However the configuration is independent of the adhesion force  $|W_{zip}|$  and of the bending stiffness  $\kappa$  and no information about  $|W_{zip}|$  can be derived.

### 9.3.2 The Experiment

Based on this model, experiments were designed to possibly derive the attractive forces  $|W_{zip}|$  mediated by the crosslinker during zipping.

However, the observations made on all zipping events presented indicated that the attraction force between the filaments was high in contrast to the repulsive forces, so the configuration of the zipping was only constrained to the pillars' geometry and the contour lengths of the grafted filaments (Fig. 9.14 (C)). Moreover, the only bending of the filaments observed, was that, mediated by the flow during the experiment (Fig. 9.11 (B), orange arrow).

Experiments were performed both to stop the flow completely while bundling and to reduce the attractive forces by reducing the crosslinker concentration to right above the critical concentration limit for bundling.

15 mM  $Mg^{2+}$  in T-buffer<sup>4</sup> was injected very slowly into a flow-cell containing a pre-assembled, unbundled actin network. The flow was stopped and dynamic actin zipping was observed. Fig. 9.15 (A) shows the unbundled network. Three filaments marked by the the red arrow in Fig. 9.15 (A) were attached on one end to the same pillar while the other ends were grafted to different pillars respectively. It is also visible that most of the filaments that were anchored in short distance between the pillars were already bundled.

As soon as they came in contact due to thermal fluctuations they zipped together (red arrows in Fig. 9.15 (B) and (C)). Later another zipping event could also be de-

<sup>4</sup>Below concentrations of 15 mM  $Mg^{2+}$  crosslinks could not be detected in the two dimensional networks.

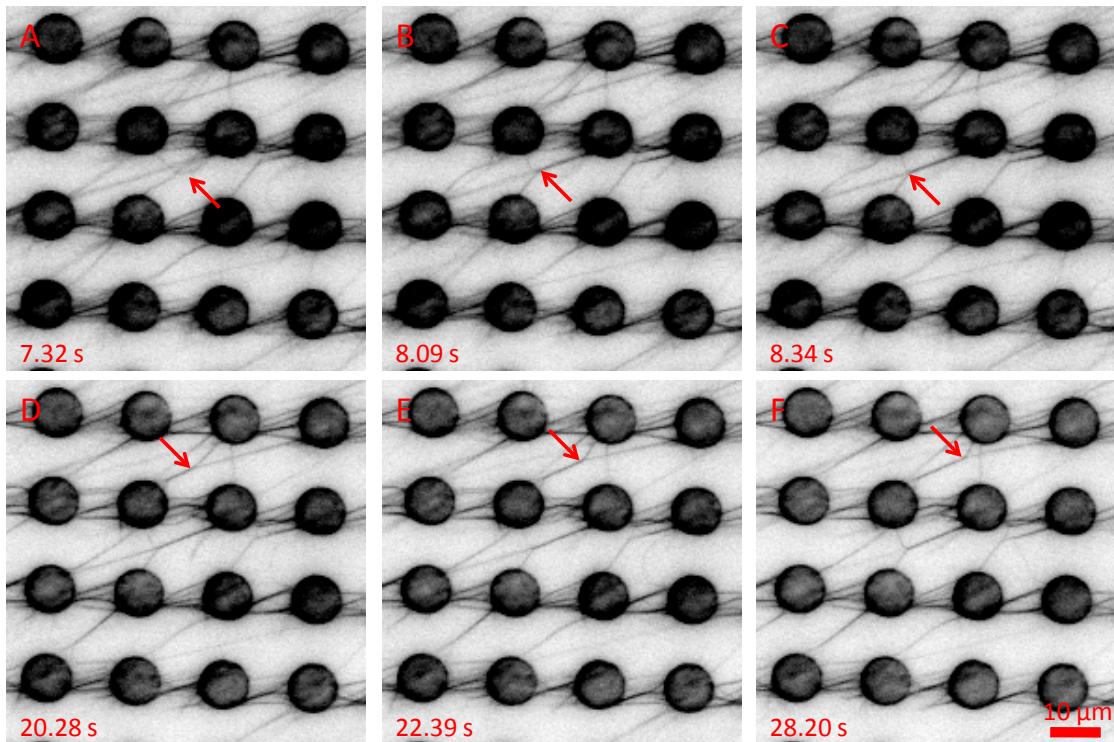


**Figure 9.15:** Actin zipping mediated by 15 mM  $Mg^{2+}$ . Two free dangling actin filaments (red arrow in (A)) zip along another filament (arrow in (B)) to the same equilibrium point (arrow in (C)). After a few seconds another zipping event occurs (arrows in (D-F)). The scale bar is 10  $\mu$ m.

tected (red arrows in Fig. 9.15 (D-E)).

However, there were no fluctuations within the bundled actin detectable or they were below the temporal and spatial resolution limits of the system. The zipping again ended up in a purely geometrical constrained configuration, only determined by the geometry of the pillars and the contour length of the filaments.

To confirm these findings Fig. 9.16 shows an example of a high-power magnification of the zipping event marked by the red arrows in Fig. 9.15 (A-C). As shown in Fig. 9.16 (A-D), the radius of curvature  $R_{co}$  decreased until there was no curvature detectable any more (estimations limited by the resolution; curvature of the filament marked by thicker red line within the circle). Moreover, high magnification cut of the region around the zipping point (Fig. 9.16 (E)) revealed that only rough estimations could be made about the exact position of the zipping point. The angles between the filaments at the estimated zipping point varied in this case from about  $93^\circ$  to  $150^\circ$ , which means that the bending radius can not be resolved any more.

Additionally, a series of three consecutive, high magnification images of the region of the two unzipped actin levers made clear that fluctuations were not detectable (Fig. 9.16 (F-F2)) within the spatial and temporal resolution limit of the experiment. The spatial resolution of the camera was about 250 nm per pixel.

As our data indicated above, it is impossible to derive data about the binding forces of crosslinked actin on micropillars by conventional fluorescence microscopy. Due to the distance of the free standing pillars to the objective it is neither possible to measure the actin on the micropillars by total internal reflection fluorescence microscopy (TIRF) nor by reflection interference contrast microscopy (RICM). However, from its optical design, it was straightforward to use our flow-cell in combination with optical trapping. Thus, we implemented the presented system in an optical tweezers setup to measure the forces directly on the zipped filaments. This will be presented in the next chapter.

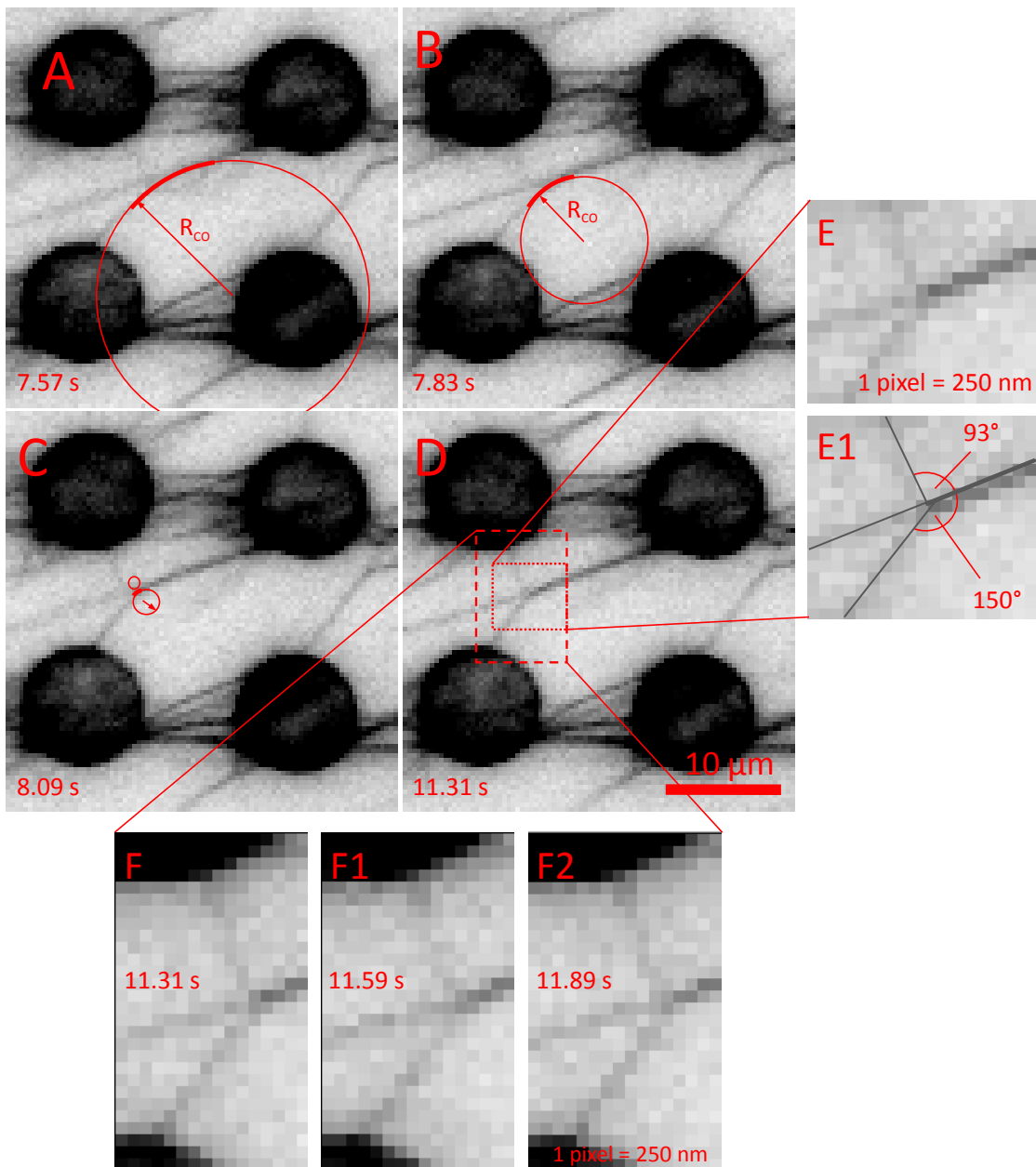


**Figure 9.16:** High magnification cuts of actin zipping shown in Fig. 9.15 (A-C). The radius of curvature  $R_{co}$  of the lower filament decreases during propagation of the zipping point (A-C) and ends up in a state where the curvature is not detectable (D). A high magnification cut in (E) shows the zipping-point region. The exact zipping point can not be determined. (E1) reveal the estimated angles for the filaments in the zipping point. (F-F2) shows a time series of three consecutive images. The region around the zipping point is magnified. The exact position of the filaments is blurred. The scale bar in (A-D) is  $10\ \mu\text{m}$ , one square in (E-F2) corresponds to one pixel of the camera, which is about  $250\ \text{nm}$ .

# Unbundling Forces of Freely Suspended Crosslinked F-actin measured by Optical Tweezers

As shown in the previous chapter, freely suspended quasi two-dimensional actin networks on micropillars could be successfully crosslinked with various actin bundling agents. Within the experiments filaments showed bundling in a zip-like manner. According to the theory of actin zipping<sup>[223]</sup> it should be possible to derive the bundling force between the filaments mediated by the crosslinking molecule by determining the contour length of the zipped filaments, the exact zipping point and the thermal fluctuation of the filaments after zipping. However it was proven that due to the limited spacial and temporal resolution of normal fluorescence microscopy it was hardly possible to get values for calculating the involved bundling force from these experiments.

A possibility to circumvent this challenge is to directly measure the bundling or the unbundling forces. In literature, the forces of protein-protein interaction were measured to be in the lower piconewton regime. Systems, which are able to resolve such forces are for example the optical tweezers.

In optical tweezers dielectric spheres are trapped by a focused laser beam. The laser transfers a momentum to these spheres, trapping them in the center of the focus. The trap has a certain spring constant, which has to be measured before each experiment. If the sphere is pulled out of the trap by an external force it behaves like being attached to a simple spring. By measuring the displacement of the sphere the

external force is simply calculated by Hooke's law (7.1).

The optical tweezers system used in these studies was built up by Jennifer Curtis and Christian Schmitz.<sup>[167,224-227]</sup> Further important improvements by Kai Uhrig<sup>[169]</sup> made it possible both to perform fluorescence and high speed bright-field imaging simultaneously while trapping. With this setup it was possible to follow actin unbundling and sphere displacement at the same time.

To perform experiments on two dimensional actin networks on micropillars the microfluidic system has to provide some important features: The chemical environment has to be controllable at any time, the flow has to be stopped while measuring to prevent flow artifacts in the sensitive system, the device has to be transparent and a reservoir of microspheres has to be provided prior to the trapping.

Our unique flow-cell design fulfilled all these features. In the presented study we measured actin unzipping on micropillar interfaces. Additionally, unlike other groups who measured actin unzipping on protein coated surfaces<sup>[195,228]</sup>, we completely prevented the risk to measure surface artifacts by anchoring the actin to the top of the pillars with a height comparable the persistence length of the actin.

The actin network was locally anchored to the pillar tops and crosslinked by both 20 mM  $Mg^{2+}$  and  $\alpha$ -actinin. The presented work was done in collaboration with Kai Uhrig.

## 10.1 Unzipping Forces of Actin Bundles

The pillars acted as rigid anchoring points for the actin. Since the micropillar field provided almost 25,000 obstacles it was possible to either find various zipping events after crosslinking the actin network and minimize photo bleaching effects to the filaments within one experiment. After crosslinking the network, a microsphere was trapped by the laser (Fig. 10.1 (A)) and attached to one lever arm of the zipped filament (Fig. 10.1 (B)). Applying a force, which was perpendicular to the zipped filaments it was possible to open the zipper and measure the retraction forces (Fig. 10.1 (C)).

A flow channel was built containing a micropillar field with interpillar distances of 5, 7, 9 and 11  $\mu\text{m}$ , a pillar diameter of 5  $\mu\text{m}$  and a height of 15  $\mu\text{m}$ . The flow channel was connected to a syringe pump. The substances to create a crosslinked F-actin network on the pillar tops were injected in the flow-cell the same way as already

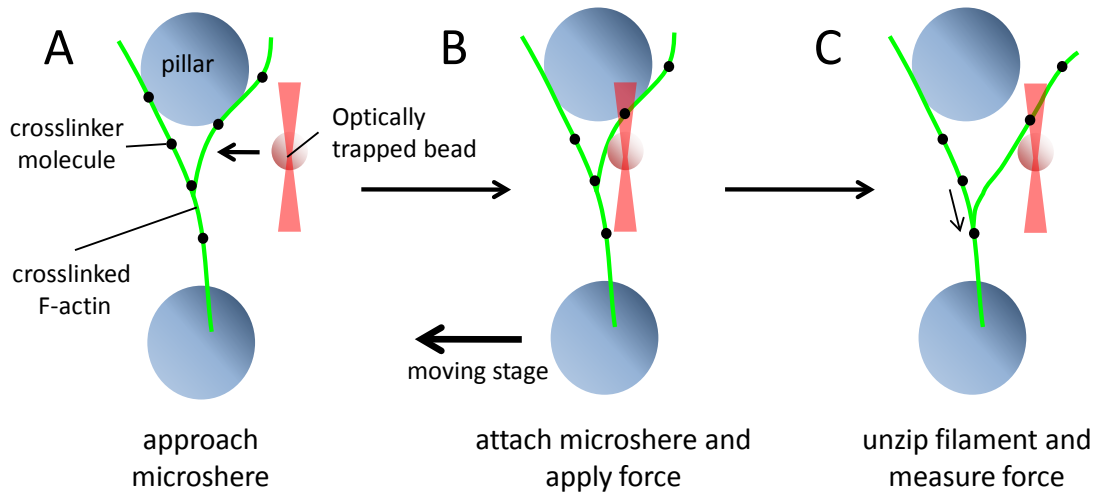


**Figure 10.1:** Scheme of actin unbundling by optically trapped microspheres. A microsphere is trapped in an optical trap and brought nearby a zipped actin bundle (A). After attaching the sphere to one lever arm of the zipper an external force is applied by moving the underlying stage (B). The zipper opens and the sphere is retracted towards the center of the optical trap (C). Measuring the displacement difference to the trap's center reveals the unbundling force of the filaments.

described in the previous chapter. To allow the assembly of a not too dense network which would complicate the later measurements we chose an actin concentration of 25 nM. Flow velocities between 0.5-2  $\mu\text{l}/\text{min}$  were found to be suitable to create a filament network configuration with a big chance of zipping events and minimized damaging effects to the network by the flow. The network formation was followed by fluorescence microscopy.

As crosslinking mediating substances 750 nM  $\alpha$ -actinin and 20 mM  $\text{Mg}^{2+}$  were used, both diluted in T-buffer. After crosslinking the flow-cell was again rinsed with T-buffer and a dilution of 0.02% poly-L-lysine functionalized microspheres were injected. Right after the approaching of the beads in the microchamber the flow was stopped. A bead was trapped by the single optical tweezers and attached to one lever arm of two zipped actin filaments. To avoid photo damage on the actin, the force measurements had to be started right after the attachment. The piezo stage, the fluorescent and the high speed bright field recording were started simultaneously. The stage was moved at constant speed (0.2  $\mu\text{m}/\text{s}$ ) while the optical trap was kept at the same position to apply an external force on the bundled actin. The position of the bead was recorded at 500 frames/s in bright field. With that we could directly measure the force that the filament exerted on the trapped bead. The trap's

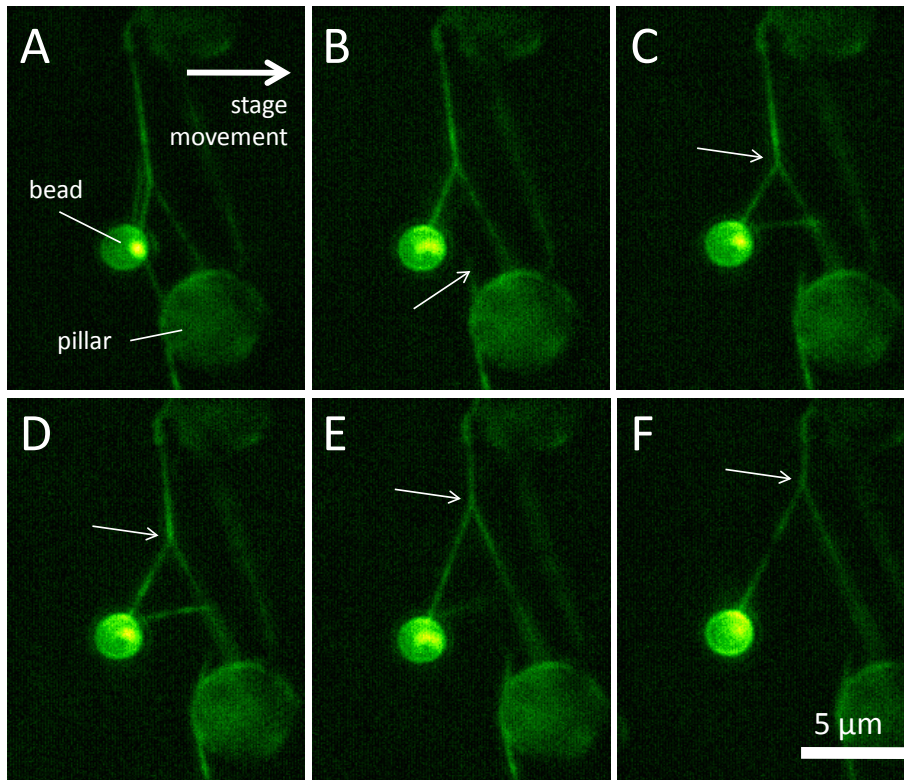


**Figure 10.2:** The snapshots show fluorescent images of actin unzipping which is bundled by  $20\text{mM Mg}^{2+}$ . After the trapped bead is attached to one lever of the actin zipper (green) the underlying stage is moved to the right (A). The trap position is kept constant. (B) The left lever arm of the zipped actin breaks at the bead (white arrow). Further stage movement increases the tension on the filaments (white arrow in C) which results in unzipping and propagation of the zipping point (white arrow in (D)). Moving the stage further unzipping events occur (white arrows in (E) and (F)). Such events are tracked and used for force calculations. The scale bar corresponds to  $5\ \mu\text{m}$ .

stiffness was calibrated by Brownian motion calibration and power spectral analysis after each experiment.

In Fig. 10.2 a force induced unzipping event is shown. The actin was crosslinked with  $20\text{mM Mg}^{2+}$ . The stage and with it the micropillar field was moved to the right (Fig. 10.2 (A)). The applied external force resulted a tension of the filaments and the filament broke away at the bead (arrow in Fig. 10.2 (B)). This made it possible to subsequently measure the force induced unzipping only at the zipping point. A propagation of the zipping point could be achieved by further moving the stage (arrows in Fig. 10.2 (C-F)).

The exact position of the bead was tracked via bright field imaging and compared

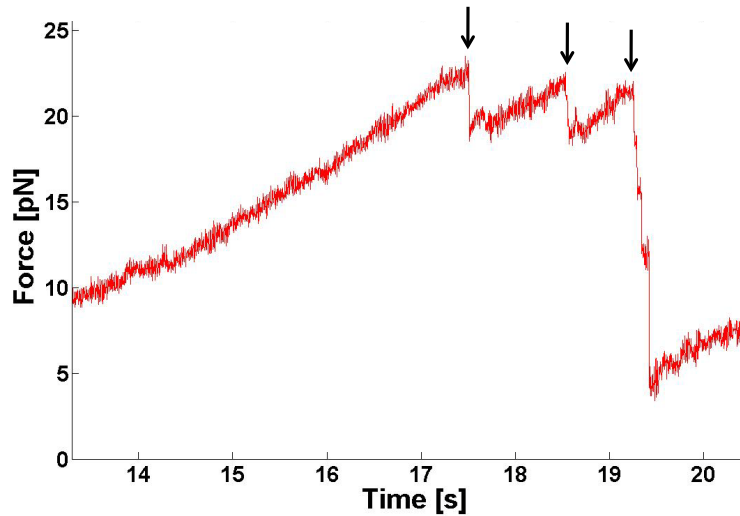


**Figure 10.3:** Force graph of actin unzipping shown in Fig 10.2. The retraction force acting on the bead which is attached to an actin zipper increases continuously until the external force overcomes the bundling force and the bead snaps back in direction to the trap's center (arrows). The steps indicate the unzipping and within the unbundling force. The last event is the release of part of the filament which is not crosslinked.

to the equilibrium position of the optical trap. The breaking of a bond could be determined by a drop in the measured force which was due to released tension in the adjacent filament. A part of the force curve which was derived from the experiment in Fig. 10.2 is presented in Fig. 10.3. The first two steps, marked with the arrows, could be associated to the unzipping between Fig. 10.2 (D) and (E). The last step was the release of a long piece of the filament between Fig. 10.2 (E) and (F). The filaments were apparently not bundled in that region.

As seen in Fig. 10.2, the angle at the zipping point was not perpendicular. Thus, the force measured for the bead spliced up at the zipping point in a perpendicular component and a component which is parallel to the crosslinked part of the filament. However, only the perpendicular forces were responsible for unzipping. Therefore, the measured forces were corrected by the sine of the angle between the two filament levers. This correction was only possible with our setup where the measured unzipping could be correlated to the respective fluorescence images.

Another important fact, which has to be considered is the loading rate. The loading

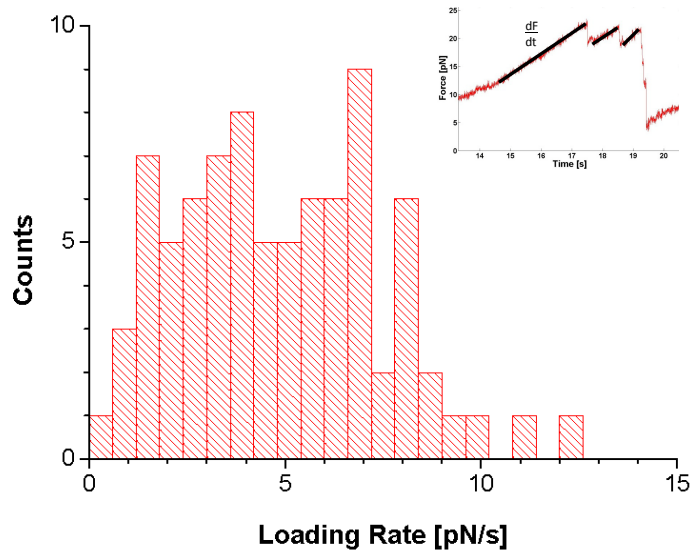


**Figure 10.4:** The histogram shows the loading rates on the actin zipper 82 unzipping events with  $20 \text{ mM Mg}^{2+}$ . Although they are widely distributed over a range from 0-10 pN/s they are still in an order of magnitude. The inset shows the calculation of the corresponding loading rates from the force graph.

rate is the force, which is applied to the bond per time interval. A bond can be thermally activated and therefore when measured a broad distribution is obtained. The rupture force logarithmically depends on the loading rate.<sup>[229,230]</sup> The loading rate has only a significant influence on the rupture forces if its value span through orders of magnitudes.<sup>[231,232]</sup>

In our case, the retraction velocity of the moving stage exerted the external force. However, our measured system consisted of elastic elements which the actual loading rate deviating from the value set by the stage. The resulted loading rates are shown in the histogram in Fig. 10.4. The loading rates for the above presented unzipping were calculated by measuring the slope of a linear fit to the force curve before the unzipping event (inset in Fig. 10.4). The loading rates were all in same order of magnitude and therefore the measured unzipping forces were not significantly influenced.

By fluorescence imaging we could also exclude artifacts in the force measurements, such as the complete rupture of a filament from the bead. Fig. 10.5 shows an example of this event. Again the bead was first attached to one lever arm of the actin and the stage was moved to the right (Fig. 10.5 (A)). Then the filament close to the

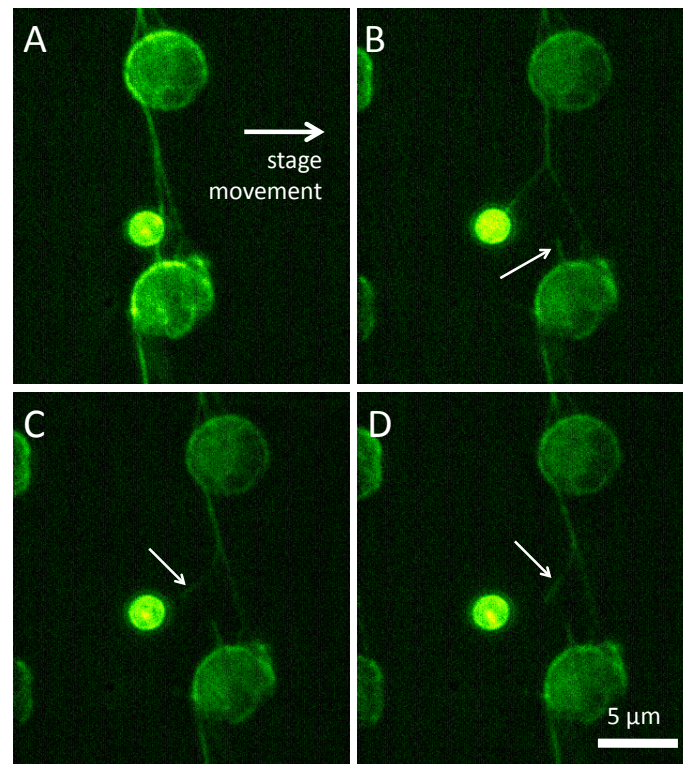


**Figure 10.5:** Rupture of a bundled filament. The actin is crosslinked with 20 mM  $Mg^{2+}$ . A bead is attached to one lever arm of the actin zipper (A). Tension is applied to the filaments by moving the stage to the right (B). The filament ruptures at the bead (C) releasing the filament (D). The scale bar corresponds to 5  $\mu\text{m}$ .

pillar first detached from the bead (white arrow in Fig. 10.5 B) and afterwards the upper lever ruptured (white arrows in Fig. 10.5 (C) and (D)).

We measured the forces of unzipping events for filaments crosslinked with 20 mM  $Mg^{2+}$  and with 750 nM  $\alpha$ -actinin. Fig. 10.6 shows a histogram of 82 unzipping events for 20 mM  $Mg^{2+}$ . It revealed two mean rupture force peaks between 6-8 pN and 17-20 pN. Unzipping forces above 30 pN were not detectable. In contrast the force histogram for 101 unzipping events for actin crosslinked with  $\alpha$ -actinin showed a peak between 30-45 pN (Fig. 10.7).

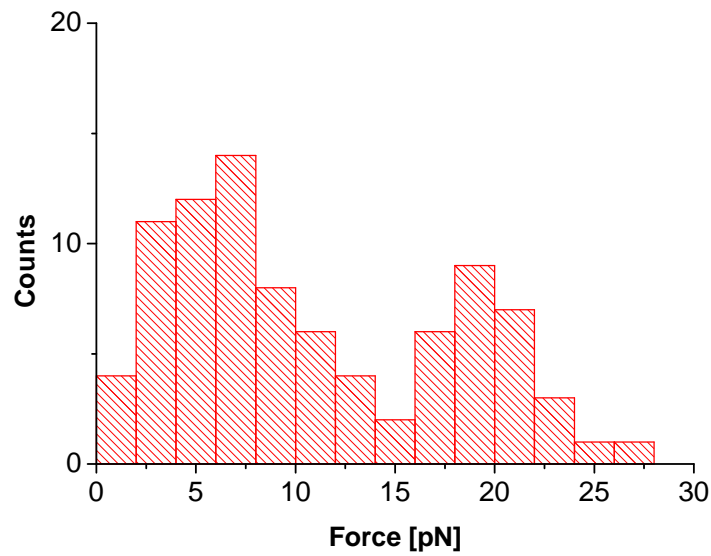


**Figure 10.6:** Unzipping force histogram of actin bundled by 20 mM Mg<sup>2+</sup> showing two mean rupture force peaks between 6-8 pN and 17-20 pN. n=82

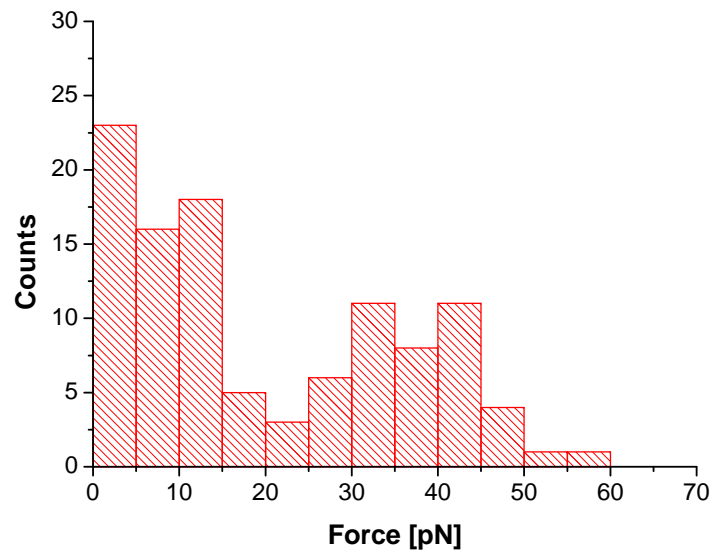


**Figure 10.7:** Unzipping force histogram of actin bundled by 750 nM  $\alpha$ -actinin shows a rupture force peak between 30-45 pN and undefined rupture events between 0-15 pN. n=101

## Conclusion and Outlook

The presented study aimed to create a model system for the actin cortex in cells to get more insights in the mechanics of these two-dimensional networks and to develop a versatile, closed microfluidic system in which these networks can be investigated under various conditions.

The exact influence of single factors on the mechanical properties of cells *in vivo* is often undetermined. Even if the system is simplified to single cells *in vitro*, the system remains very complex. We created an extremely minimized mimick of the actin cortex.

Therefore, arrays of micropillars made of PDMS were fabricated by standard photolithography. The microposts had inter-pillar distances between 5-12  $\mu\text{m}$ , a height of 15  $\mu\text{m}$  and diameters between 5-10  $\mu\text{m}$ . The pillars were free standing in a regular array, with an overall dimension of  $5000 \times 5000 \mu\text{m}$ . One single field exhibited more than 25,000 obstacles. The pillar arrays were incorporated in a newly designed flow-cell. The flow channel itself was made of PDMS and had a height of 40  $\mu\text{m}$ . Assembly of the channel with the micropost arrays resulted in a closed flow-cell with a reaction chamber containing a volume of  $\sim 1.5 \mu\text{l}$  with free standing obstacles upside down into the channel. This unique design enabled the exact control of the physico-chemical environment in the chamber. Additionally, this system is transparent and non-fluorescent, which offers the possibility to use it in two-objective setups.

Such systems can serve as scaffolds for biomimetic models of the actin cytoskeleton. Roos *et al.* already demonstrated the creation of a quasi two-dimensional filamentous actin network on silicon pillar arrays.<sup>[7]</sup> Hereby, the actin filaments self-assemble to the pillar tops, forming a wide-spread thin network, which is locally anchored on

the pillar tops. This mimics the configuration of the actin cortex *in vivo* where the thin network is locally anchored to the plasma membrane. This biomimetic system can be easily manipulated by biofunctional agents like crosslinkers since the dangling network is freely accessible in contrast to systems deposited directly to surfaces.

To create a quasi two-dimensional actin network on the pillar tops they were biofunctionalized with N-ethyl-maleimid modified heavy meromyosin (NEMHMM), which provides specific anchor points for the filaments. The inter-pillar distance was chosen to be smaller than the contour length of an actin filament determined to be around  $20\ \mu\text{m}$  *in vitro*.

To further investigate the behavior of this network with respect to crosslinkers, not only so-called passive crosslinkers like filamin,  $\alpha$ -actinin and divalent cations were added to the network, but also mini-filaments of the active motor protein myosin II were applied. Myosin II was fluorescently labeled to identify the motor protein separately from the labeled F-actin. It was shown, that the myosin regularly bound all over the actin filaments. By adding ATP the myosin dissociated, resulting again in single filaments. This means that a simple on-off switch for network and bundle formation was obtained. Such a system of network disassembly has been already demonstrated in three dimensions.<sup>[213]</sup> Here, the biologically relevant network disassembly in two dimensions was demonstrated.

Crosslinking of the actin networks on the pillar tops resulted in a similar configuration irrespective of the type of crosslinker used. The configuration only differed due to geometrical aspects (position of the pillars), their local protein concentration in the flat network sheet and the flow direction. This might give a hint that the configuration of the actin cortex *in vivo* is more dependent on its anchoring points, in this case to the plasma membrane, and the local availability of crosslinkers than on the type of crosslinker. This is in contrast to observations made for actin crosslinks in bulk.<sup>[111,112]</sup> It was observed that the concentration of  $\text{Mg}^{2+}$  has to be at least 15 mM to crosslink actin. Thus, *in vivo* crosslinking with divalent cations seems to play a minor role since the maximum  $\text{Mg}^{2+}$  concentration found in cells usually does not exceed 2.5 mM.<sup>[20]</sup> However, it could play a cooperative effect with other crosslinkers by decreasing the electrostatic repulsion between the actin filaments and promote further crosslinking.

The flow-cell design allowed us to observe zipping of actin filaments during the crosslinking by all investigated crosslinkers. Actin filaments, anchored to the pil-

---

lar tops in the right configuration, bundled in a zip-like manner. The dynamics of these zipping events could be followed in real-time. Kinetics of these events were strongly dependent on the configuration of the zipped filaments and not on the type of crosslinker. Additionally no dependence on the crosslinker concentration could be detected. But the number of filaments involved in the zipping played a role in the crosslinking velocity. It seemed, that the zipping velocity for single filaments did not fall below  $6 \mu\text{m/s}$  in our experiments independent of type and concentration of the crosslinker and the configuration of the actin filaments. However, bundles of pre-crosslinked actin filaments showed a lower velocity of further zipping. This was due to the increased stiffness of the bundles. The attractive forces mediated by the bundling agent work against the bending stiffness of the bundle resulting in a decreased zipping velocity. It was recently described theoretically how to directly calculate the attractive forces from experimental data of the zipping events on the micropillars.<sup>[223]</sup> Therefore, the exact position of the zipping point and the exact contour length of the involved filaments had to be determined. However, it was not possible to derive this data for the calculations due to the limited spatial and temporal resolution of conventional microscopy. Further investigations could aim to use high resolution stimulated emission depletion (STED)-microscopy to determine the exact position of the filaments, since other high resolution methods like TIRF or RICM can not be applied because of the distance of the pillars from the surface. Preliminary experiments have proven the feasibility of using STED for actin observation in the flow-cell.

But we also showed a system to directly measure unzipping forces circumventing the problem of limited resolution. Therefore, we implemented the free standing micropillars in the flow-cell in an optical tweezers system. Unlike measurements by other groups made on actin bundling forces<sup>[195,228]</sup> we could completely exclude surface artifacts due to the free dangling actin filaments on the pillar tops. Additionally, we could stop the flow in the microchamber with our closed flow-cell system, which is crucial for accurate force measurements on the optical tweezers. Biofunctionalized microspheres were attached to the actin zippers and an external force was applied to unzip the filaments and measure directly the retraction forces. In this system it was possible to use simultaneously fluorescence and high speed bright field imaging during trapping. Unspecific rupture events and unspecific unbinding within the experiments could be excluded. We measured the unzipping forces of actin filaments

crosslinked with 20 mM  $Mg^{2+}$  and 750 nM  $\alpha$ -actinin, respectively. For  $\alpha$ -actinin, an unzipping force between 30-45 pN was observed, while the unzipping forces for 20 mM  $Mg^{2+}$  did not exceed 28 pN. However, the nature of this difference is still undetermined. Furthermore, cooperative effects of the crosslinker may play a role broadening the distribution of the measured unzipping forces. Measurements at different crosslinker concentrations and loading rates could help to derive the exact nature of the measured forces. A further possibility is to label the crosslinkers fluorescently to determine the exact decoration of binding agents on the actin filaments. Nonetheless, with the present system it was for the first time possible to measure unzipping forces in piconewton resolution on a free-standing quasi two-dimensional actin network.

To summarize, we presented a novel tool to investigate the mechanics of a biomimetic actin cortex model. We could establish a point-wisely anchored, free dangling quasi two-dimensional actin network on an array of micropillars and crosslink it with different passive and active actin binding agents. A novel closed flow-cell system enabled us to follow the dynamics of actin zipping in real-time and combine the system with optical tweezers to measure unzipping forces. Still, the general problems of fast photobleaching and low signal-to-noise ratio within all actin measurements remain. Nonetheless such a biomimetic system of the actin cortex in combination with the novel, flexible flow-cell design can give deeper insights in the mechanics of two-dimensional actin networks.

# List of Figures

2.1	Schematic view of a cell connected to the ECM	6
2.2	Schematic view of a fibronectin	7
2.3	Schematic view of a cell adhered on a pillar	10
2.4	The structure of the gingiva	11
2.5	Structure of intermediate filaments	13
3.1	Catalytic cycle of the PDMS-hydrosilylation	16
3.2	Chromium photomask production	17
3.3	SEM-Pictures of microfabricated pillar arrays	20
3.4	Scheme of the steps needed for PDMS mould fabrication	20
3.5	FN coated on micropillar tops	21
3.6	Bending of single pillar	22
3.7	Steps to co-culture system establishment	25
4.1	SEM images of a 8 $\mu\text{m}$ and a 5 $\mu\text{m}$ -Field	33
4.2	IHGKs cultured on FN-coated glass	33
4.3	SEM images of IHGKs cultured on micropillars	34
4.4	Cell viability on Micropillars	35
4.5	Keratinocytes deflecting micropillars	36
4.6	Morphology of IHGKs on different pillar fields	38
4.7	Optical cuts and 3D reconstruction of a IHGK on a 5 $\mu\text{m}$ substrate	39
4.8	Optical cuts and 3D reconstruction of an IHGK on a 11 $\mu\text{m}$ substrate	40
4.9	IHGKs on different substrates stained for K1	41
4.10	IHGKs on different substrates stained for K10	43

4.11	sqPCR and qPCR of IHGKs on micropillar arrays . . . . .	44
5.1	Force exerted by a GCTF on a micropillar . . . . .	49
5.2	GCTFs on micropillars at different time points . . . . .	51
5.3	Confluent sheet of GCTFs on micropillars after a culture time of 14 h . . . . .	52
5.4	IIF and PCR of K1 and K10 of co-cultured IHGKs . . . . .	54
7.1	Structure of microtubules . . . . .	67
7.2	Structure of actin . . . . .	69
7.3	Multi-step mechanism of actin polymerization . . . . .	70
7.4	Structure of human filamin . . . . .	71
7.5	F-Actin network crosslinked with Filamin . . . . .	72
7.6	Schematic of the structure of $\alpha$ -actinin . . . . .	73
7.7	Scheme of an optical trap . . . . .	76
8.1	Chromium photomask production for flow-channels . . . . .	78
8.2	Schematic view of flow-cell assembly . . . . .	81
8.3	Confocal micrographs of actin filaments attached to a glass surface . . . . .	84
8.4	Structure of 5-iodoacetamidofluoresceine (5-IAF) . . . . .	85
8.5	Complete setup of the optical tweezers . . . . .	89
9.1	Schematic view for the assembly of a quasi 2-dimensional network . . . . .	93
9.2	Typical actin network on micropillars . . . . .	93
9.3	Network of actin crosslinked by filamin . . . . .	94
9.4	Network of actin crosslinked by magnesium ions . . . . .	96
9.5	Network of actin crosslinked by fluorescent myosin II . . . . .	97
9.6	Disassembly of actin crosslinked by myosin . . . . .	97
9.7	Dynamic bundling of actin by fluorescent myosin II . . . . .	98
9.8	Schematic of filament zipping 1 . . . . .	99
9.9	Dynamic bundling of actin by $Mg^{2+}$ . . . . .	100
9.10	Dynamic bundling of actin by $\alpha$ -actinin . . . . .	101
9.11	Dynamic actin bundling by filamin . . . . .	102
9.12	Propagation of zipping point . . . . .	103
9.13	Schematic of filament zipping 2 . . . . .	104
9.14	Schematic of filament zipping 3 . . . . .	106
9.15	Actin zipping mediated by 15 mM $Mg^{2+}$ . . . . .	108

---

9.16 High magnification cuts of actin zipping . . . . .	110
10.1 Scheme of actin unbundling by optical trapped microspheres . . . . .	113
10.2 Unzipping of actin bundled by 20 mM $Mg^{2+}$ . . . . .	114
10.3 Force graph of actin unzipping . . . . .	115
10.4 Loading rate within an unzipping experiment . . . . .	116
10.5 Rupture of a bundled filament . . . . .	117
10.6 Unzipping force histogram of actin bundled by 20 mM $Mg^{2+}$ . . . . .	118
10.7 Unzipping force histogram of actin bundled by 750 nM $\alpha$ -actinin . . . . .	118



# Bibliography

- [1] R. J. Pelham and Y. Wang. Cell locomotion and focal adhesions are regulated by substrate flexibility. *Proceedings of the National Academy of Sciences*, 94(25):13661–13665, 1997. [1](#), [6](#), [23](#)
- [2] J.L. Tan, J. Tien, D.M. Pirone, D.S. Gray, K. Bhadriraju, and C.S. Chen. Cells lying on a bed of microneedles: An approach to isolate mechanical force. *Proceedings of the National Academy of Sciences*, 100(4):1484–1489, 2003. [1](#), [9](#)
- [3] M.T. Frey, I. Y. Tsai, T.P. Russell, S.K. Hanks, and Y. Wang. Cellular Responses to Substrate Topography: Role of Myosin II and Focal Adhesion Kinase. *Biophysical Journal*, 90(10):3774–3782, 2006. [1](#), [10](#)
- [4] D.E. Ingber. Mechanics and chemistry of biosystems. 1:58–68, 2004. [2](#)
- [5] M.J. Bowick, A. Cacciuto, G. Thorleifsson, and A. Travesset. Universality classes of self-avoiding fixed-connectivity membranes. *The European Physical Journal E-Soft Matter*, 5(2):149–160, 2001. [2](#), [64](#)
- [6] M. Bowick, A. Cacciuto, G. Thorleifsson, and A. Travesset. Universal Negative Poisson Ratio of Self-Avoiding Fixed-Connectivity Membranes. *Physical Review Letters*, 87(14):148103, 2001. [2](#), [64](#)
- [7] W.H Roos, A. Roth, J. Konle, H. Presting, E. Sackmann, and J.P. Spatz. Freely suspended actin cortex models on arrays of microfabricated pillars. *Chemphyschem*, 4(8):872–877, 2003. [2](#), [65](#), [91](#), [119](#)

- [8] A. Gefen and S.S. Margulies. Are in vivo and in situ brain tissues mechanically similar? *Journal of Biomechanics*, 37(9):1339–1352, 2004. [5](#)
- [9] A.J. Engler, M.A. Griffin, S. Sen, C.G. Bönnemann, H.L. Sweeney, and D.E. Discher. Myotubes differentiate optimally on substrates with tissue-like stiffness: pathological implications for soft or stiff microenvironments. *The Journal of Cell Biology*, 166(6):877, 2004.
- [10] S. Diridollou, F. Patat, F. Gens, L. Vaillant, D. Black, JM Lagarde, Y. Gall, and M. Berson. In vivo model of the mechanical properties of the human skin under suction. *Official Journal of International Society for Bioengineering and the Skin (ISBS) International Society for Digital Imaging of Skin (ISDIS) International Society for Skin Imaging (ISSI)*, 6(4):214–221, 2000. [5](#)
- [11] K.R. Buckley, I.K. and Porter. Cytoplasmic fibrils in living cultured cells. a light and electron microscope study. *Protoplasma*, 64(4):349–80, 1967. [5](#)
- [12] J.A. Schloss. Myosin subfragment binding for the localization of actin-like microfilaments in cultured cells. a light and electron microscope study. *The Journal of Cell Biology*, 74(3):794–815, 1977. [5](#)
- [13] R.D. Goldman, A. Milsted, J.A. Schloss, J. Starger, and M.J. Yerna. Cytoplasmic fibers in mammalian cells: Cytoskeletal and contractile elements. *Annual Reviews in Physiology*, 41(1):703–722, 1979. [5](#)
- [14] B. Geiger, A. Bershadsky, R. Pankov, and K. M. Yamada. Transmembrane crosstalk between the extracellular matrix–cytoskeleton crosstalk. *Nat Rev Mol Cell Biol*, 2(11):793–805, Nov 2001. [5](#), [6](#)
- [15] H.M. Blau. Differentiation requires continuous regulation. *The Journal of Cell Biology*, 112(5):781–783, 1991. [6](#), [57](#)
- [16] E. Ruoslahti and B. Obrink. Common principles in cell adhesion. *Experimental Cell Research*, 227(1):1–11, 1996. [6](#), [57](#)
- [17] C. S. Chen, J. Tan, and J. Tien. Mechanotransduction at cell-matrix and cell-cell contacts. *Annual Review of Biomedical Engineering*, 6(1):275–302, 2004. [6](#)

- [18] D.E. Ingber. Cellular mechanotransduction: putting all the pieces together again. *FASEB Journal*, 20(7):811–827, May 2006.
- [19] A. J. Engler, S. Sen, H. L. Sweeney, and D. E. Discher. Matrix elasticity directs stem cell lineage specification. *Cell*, 126(4):677–689, 2006. [6](#), [57](#), [64](#)
- [20] B. Alberts, D. Bray, J. Lewis, M. Raff, K. Roberts, and J. D. Watson. Molecular biology of the cell. *New York*, 2002. [6](#), [66](#), [67](#), [120](#)
- [21] K. V. Vliet, G. Bao, and S. Suresh. The biomechanics toolbox: experimental approaches for living cells and biomolecules. *Acta Materialia*, 51:5881–5905, 2003.
- [22] A. Gutman and A.R. Kornblihtt. Identification of a third region of cell-specific alternative splicing in human fibronectin mrna. *Proceedings of the National Academy of Sciences*, 84(20):7179–7182, 1987.
- [23] S. Miyamoto, B.E.N.Z. Kathz, R.M. Lafrenie, and K.M. Yamada. Fibronectin and integrins in cell adhesion, signaling, and morphogenesis. *Annals of the New York Academy of Sciences*, 857(1):119–129, 1998. [7](#)
- [24] K.A. Piez and B.L. Trus. A new model for packing of type-i collagen molecules in the native fibril. *Bioscience Reports*, 1(10):801–810, 1981. [7](#)
- [25] A.J. Engler, L. Richert, J.Y. Wong, C. Picart, and D.E. Discher. Surface probe measurements of the elasticity of sectioned tissue, thin gels and polyelectrolyte multilayer films: Correlations between substrate stiffness and cell adhesion. *Surface Science*, 570(1-2):142–154, 2004. [7](#)
- [26] D. Lehnert, B. Wehrle-Haller, C. David, U. Weiland, C. Ballestrem, B. A. Imhof, and M. Bastmeyer. Cell behaviour on micropatterned substrata: limits of extracellular matrix geometry for spreading and adhesion. *Journal of Cell Science*, 117(1):41–52, 2004. [7](#)
- [27] A. Yeung and E. Evans. Cortical shell-liquid core model for passive flow of liquid-like spherical cells into micropipets. *Biophysical Journal*, 56(1):139–149, 1989. [8](#)

- [28] E. Evans and A. Yeung. Apparent viscosity and cortical tension of blood granulocytes determined by micropipet aspiration. *Biophysical Journal*, 56(1):151–160, 1989. [8](#)
- [29] M. Beil, A. Micoulet, G.v Wichert, S. Paschke, P. Walther, M. B. Omary, P. P Van Veldhoven, U. Gern, E. Wolff-Hieber, J. Eggermann, J. Waltenberger, G. Adler, J.P. Spatz, and T. Seufferlein. Sphingosylphosphorylcholine regulates keratin network architecture and visco-elastic properties of human cancer cells. *Nature Cell Biology*, 5(9):803–811, 2003. [8](#)
- [30] A. Ashkin and J. M. Dziedzic. Optical trapping and manipulation of viruses and bacteria. *Science*, 235(4795):1517–1520, 1987. [8](#)
- [31] K. Svoboda and S. M. Block. Biological applications of optical forces. *Annual Reviews in Biophysics and Biomolecular Structure*, 23(1):247–285, 1994. [8](#)
- [32] A.D. Mehta, M. Rief, J.A. Spudich, D.A. Smith, and R.M. Simmons. Single-molecule biomechanics with optical methods. *Science*, 283(5408):1689–1695, 1999. [8](#)
- [33] J. C. Gebhardt, A. E. Clemen, J. Jaud, and M. Rief. Myosin-v is a mechanical ratchet. *Proceedings of the National Academy of Sciences*, 103(23):8680–5, 2006. [8](#), [91](#)
- [34] A. E. Clemen, M. Vilfan, J. Jaud, J. Zhang, M. Barmann, and M. Rief. Force-dependent stepping kinetics of myosin-v. *Biophysical Journal*, 88(6):4402–10, 2005. [8](#)
- [35] C. Rotsch and M. Radmacher. Drug-induced changes of cytoskeletal structure and mechanics in fibroblasts: An atomic force microscopy study. *Biophysical Journal*, 78(1):520–535, 2000. [8](#)
- [36] A.K. Harris, P. Wild, and D. Stopak. Silicone rubber substrata: a new wrinkle in the study of cell locomotion. *Science*, 208(4440):177–179, 1980. [9](#)
- [37] J.A. Spudich, R.J. Pelham, and Y. Wang. High resolution detection of mechanical forces exerted by locomoting fibroblasts on the substrate. *Molecular Biology of the Cell*, 10(4):935–945, 1999. [9](#)

- [38] T. Hunter, D.M. Helfman, E.T. Levy, C. Berthier, M. Shtutman, D. Riveline, I. Grosheva, A. Lachish-Zalait, M. Elbaum, and A.D. Bershadsky. Caldesmon Inhibits Nonmuscle Cell Contractility and Interferes with the Formation of Focal Adhesions. *Molecular Biology of the Cell*, 10(10):3097–3112, 1999. [9](#)
- [39] M. Chrzanowska-Wodnicka. Rho-stimulated contractility drives the formation of stress fibers and focal adhesions. *The Journal of Cell Biology*, 133(6):1403–1415, 1996. [9](#)
- [40] J. Lee, M. Leonard, T. Oliver, A. Ishihara, and K. Jacobson. Traction forces generated by locomoting keratocytes. *J. Cell Biol.*, 127(6):1957–1964, 1994. [9](#)
- [41] C.M. Lo, H.B. Wang, M. Dembo, and Y. Wang. Cell movement is guided by the rigidity of the substrate. *Biophysical Journal*, 79(1):144–152, 2000. [9](#)
- [42] S. Munevar, Y. Wang, and M. Dembo. Traction Force Microscopy of Migrating Normal and H-ras Transformed 3T3 Fibroblasts. *Biophysical Journal*, 80(4):1744–1757, 2001. [9](#)
- [43] N. Q. Balaban, U. S. Schwarz, D. Riveline, P. Goichberg, G. Tzur, I. Sabanay, D. Mahalu, S. Safran, A. Bershadsky, L. Addadi, and B. Geiger. Force and focal adhesion assembly: a close relationship studied using elastic micropatterned substrates. *Nature Cell Biology*, 3(5):466–472, 2001. [9](#), [64](#)
- [44] M. Dembo and Y.L. Wang. Stresses at the Cell-to-Substrate Interface during Locomotion of Fibroblasts. *Biophysical Journal*, 76(4):2307–2316, 1999. [9](#)
- [45] D. Riveline, E. Zamir, N. Q. Balaban, U. S. Schwarz, T. Ishizaki, S. Narumiya, Z. Kam, B. Geiger, and A. D. Bershadsky. Focal contacts as mechanosensors: externally applied local mechanical force induces growth of focal contacts by an mdia1-dependent and rock-independent mechanism. *Journal of Cell Biology*, 153(6):1175–1186, Jun 2001.
- [46] N. Wang, E. Ostuni, G. M. Whitesides, and D. E. Ingber. Micropatterning tractional forces in living cells. *Cell Motility and the Cytoskeleton*, 52(2):97–106, 2002.

- [47] R. Merkel, N. Kirchgessner, C.M. Cesa, and B. Hoffmann. Cell force microscopy on elastic layers of finite thickness. *Biophysical Journal*, 93(9):3314–2007. [9](#)
- [48] C. Barentin, Y. Sawada, and J.P. Rieu. An iterative method to calculate forces exerted by single cells and multicellular assemblies from the detection of deformations of flexible substrates. *European Biophysics Journal*, 35(4):328–339, 2006. [9](#)
- [49] L. Landau and EM Lifshitz. Theory of elasticity. *Pergamon Press, Oxford, 1986*, 1986. [9](#), [22](#), [23](#)
- [50] C.G. Galbraith and M.P. Sheetz. A micromachined device provides a new bend on fibroblast traction forces. *Proceedings of the National Academy of Sciences*, 94(17):9114–9118, 1997. [9](#)
- [51] O. du Roure, A. Saez, A. Buguin, R.H. Austin, P. Chavrier, P. Silberzan, and B. Ladoux. Force mapping in epithelial cell migration. *Proceedings of the National Academy of Sciences*, 102(7):2390–2395, 2005.
- [52] A. Kajzar, C. M. Cesa, N. Kirchgessner, B. Hoffmann, and R. Merkel. Toward physiological conditions for cell analyses: Forces of heart muscle cells suspended between elastic micropillars. *Biophysical Journal*, 94(5):1854–1866, 2008.
- [53] N.J. Sniadecki and C.S. Chen. Microfabricated silicone elastomeric post arrays for measuring traction forces of adherent cells. *Methods in Cell Biology*, 83:314–2007.
- [54] S. Schluger. Periodontal diseases: basic phenomena, clinical management, and occlusal and restorative interrelationship. *Philadelphia, PA : Lea & Febiger*, 1990.
- [55] P.M. Bartold, L.J. Walsh, and A.S. Narayanan. Molecular and cell biology of the gingiva. *Periodontology 2000*, 24(1):28–55, 2000. [11](#), [47](#)
- [56] H.E. Schroeder. Oral mucosa. *Oral Structural Biology*, pages 350–391, 1991.

- [57] K. Boehnke, N. Mirancea, A. Pavesio, N.E. Fusenig, P. Boukamp, and H.J. Stark. Effects of fibroblasts and microenvironment on epidermal regeneration and tissue function in long-term skin equivalents. *European Journal of Cell Biology*, 86(11-12):731–746, 2007. [12](#), [47](#)
- [58] T. Steinberg, S. Schulz, J.P. Spatz, N. Grabe, E. Mssig, A. Kohl, G. Komposch, and P. Tomakidi. Early keratinocyte differentiation on micropillar interfaces. *Nano Letters*, 7(2):287–294, 2007. [12](#), [33](#), [34](#), [35](#), [36](#), [41](#), [43](#), [44](#)
- [59] E. Müssig, T. Steinberg, S. Schulz, J.P. Spatz, J. Ulmer, N. Grabe, A. Kohl, G. Komposch, and P. Tomakidi. Connective-tissue fibroblasts established on micropillar interfaces are pivotal for epithelial-tissue morphogenesis. *Advanced Functional Materials*, 18(19):2919–2929, 2008. [12](#), [49](#), [51](#), [52](#), [54](#)
- [60] R. D. Goldman, S. Khuon, Y. H. Chou, P. Opal, and P. M. Steinert. The function of intermediate filaments in cell shape and cytoskeletal integrity. *Journal of Cell Biology*, 134(4):971–983, 1996. [12](#), [31](#)
- [61] Elaine Fuchs. The cytoskeleton and disease:genetic disorders of intermediate filaments. *Annual Review of Genetics*, 30(1):197–231, 1996. [12](#), [13](#), [64](#)
- [62] E. Fuchs and K. Weber. Intermediate filaments: Structure, dynamics, function and disease. *Annual Reviews in Biochemistry*, 63(1):345–382, 1994.
- [63] H. Baribault, J. Price, K. Miyai, and R. G. Oshima. Mid-gestational lethality in mice lacking keratin 8. *Genes & Development*, 7(7a):1191, 1993.
- [64] M. Nosonovsky and B. Bhushan. Biomimetic superhydrophobic surfaces: Multiscale approach. *Nano Letters*, 7(9):2633–2637, 2007.
- [65] Z. Yoshimitsu, A. Nakajima, T. Watanabe, and K. Hashimoto. Effects of surface structure on the hydrophobicity and sliding behavior of water droplets. *Langmuir*, 18(15):5818–5822, 2002.
- [66] N.J. Shirtcliffe, S. Aqil, C. Evans, G. McHale, M.I. Newton, C.C. Perry, and P. Roach. The use of high aspect ratio photoresist (su-8) for superhydrophobic pattern prototyping. *Journal of Micromechanics and Microengineering*, 14(10):1384–1389, 2004.

- [67] J.P. Youngblood and T.J. McCarthy. Ultrahydrophobic polymer surfaces prepared by simultaneous ablation of polypropylene and sputtering of poly (tetrafluoroethylene) using radio frequency plasma. *Macromolecules*, 32:6800–6806, 1999.
- [68] A. Saez, A. Buguin, P. Silberzan, and B. Ladoux. Is the mechanical activity of epithelial cells controlled by deformations or forces? *Biophysical Journal*, 89(6):L52–54, 2005.
- [69] M.T. Yang, N.J. Sniadecki, and C.S. Chen. Geometric considerations of micro-to nanoscale elastomeric post arrays to study cellular traction forces. *Advanced Materials*, 19(20):3119–3123, 2007.
- [70] A. Buguin, P. Chavrier, B. Ladoux, O. du Roure, A. Saez, and P. Silberzan. An array of microfabricated pillars to study cell migration. *Medicine Sciences (Paris)*, 21(8-9):765–767, 2005.
- [71] J. C. Crocker and D. G. Grier. Methods of digital video microscopy for colloidal studies. *Journal of Colloid Interface Science*, 179:298–310, 1996.
- [72] M. Roesch-Ely, T. Steinberg, F.X. Bosch, E. Mssig, N. Whitaker, T. Wiest, A. Kohl, G. Komposch, and P. Tomakidi. Organotypic co-cultures allow for immortalized human gingival keratinocytes to reconstitute a gingival epithelial phenotype in vitro. *Differentiation*, 74(9-10):622–637, 2006. [23](#)
- [73] P. Tomakidi, N.E. Fusenig, A. Kohl, and G. Komposch. Histomorphological and biochemical differentiation capacity in organotypic co-cultures of primary gingival cells. *Journal of Periodontal Research*, 32(4):388–400, 1997. [26](#), [48](#), [52](#)
- [74] P. Tomakidi, D. Breitzkreutz, N.E. Fusenig, J. Zöllner, A. Kohl, and G. Komposch. Establishment of oral mucosa phenotype in vitro in correlation to epithelial anchorage. *Cell and Tissue Research*, 292(2):355–366, 1998.
- [75] D.B. Shannon, S.T.W. McKeown, F.T. Lundy, and C.R. Irwin. Phenotypic differences between oral and skin fibroblasts in wound contraction and growth factor expression. *Wound Repair and Regeneration*, 14(2):172–178, 2006. [26](#), [48](#), [52](#)

- [76] P. Tomakidi, H.J. Stark, C. Herold-Mende, F.X. Bosch, H. Steinbauer, N.E. Fusenig, and D. Breitkreutz. Discriminating expression of differentiation markers evolves in transplants of benign and malignant human skin keratinocytes through stromal interactions. *The Journal of Pathology*, 200(3):298–307, 2003. [26](#)
- [77] K.J. Livak and T.D. Schmittgen. Analysis of relative gene expression data using real-time quantitative pcr and the 2- delta-delta-ct method. *Methods*, 25(4):402–408, 2001. [29](#), [42](#)
- [78] W.Y. Yeong, C.K. Chua, K.F. Leong, M. Chandrasekaran, and M.W. Lee. Comparison of drying methods in the fabrication of collagen scaffold via indirect rapid prototyping. *Journal of Biomedical Materials Research Part B*, 82(1):260, 2007. [30](#)
- [79] H.J. Stark, M. Baur, D. Breitkreutz, N. Mirancea, and N.E. Fusenig. Organotypic keratinocyte cocultures in defined medium with regular epidermal morphogenesis and differentiation. *Journal of Investigative Dermatology*, 112(5):681–691, 1999. [31](#)
- [80] H. Green, E. Fuchs, and F. Watt. Differentiated structural components of the keratinocyte. *Cold Spring Harb Symp Quant Biol*, 46(Pt 1):293–301, 1982. [31](#)
- [81] B. Lu, JA Rothnagel, MA Longley, SY Tsai, and DR Roop. Differentiation-specific expression of human keratin 1 is mediated by a composite ap-1/steroid hormone element. *Journal of Biological Chemistry*, 269(10):7443–7449, 1994. [31](#), [42](#), [53](#)
- [82] R.H. Rice and H. Green. Presence in human epidermal cells of a soluble protein precursor of the cross-linked envelope: activation of the cross-linking by calcium ions. *Cell*, 18(3):681–694, 1979. [31](#)
- [83] B.A. Dale. Filaggrin, the matrix protein of keratin. *American Journal of Dermatopathology*, 7(1):65–8, 1985. [31](#)
- [84] B. M. Gumbiner. Cell adhesion: the molecular basis of tissue architecture and morphogenesis. *Cell*, 84(3):345–357, Feb 1996.

- [85] D.R. Roop, H. Huitfeldt, A. Kilkenny, and S.H. Yuspa. Regulated expression of differentiation-associated keratins in cultured epidermal cells detected by monospecific antibodies to unique peptides of mouse epidermal keratins. *Differentiation*, 35(2):143–150, 1987. [34](#), [57](#)
- [86] H. Hennings, K. Holbrook, P. Steinert, and S. Yuspa. Growth and differentiation of mouse epidermal cells in culture: effects of extracellular calcium. *Current Problems in Dermatology*, 10:3–25, 1980.
- [87] B.S. Eckert, R.A. Daley, and L.M. Parysek. Assembly of keratin onto ptk1 cytoskeletons: evidence for an intermediate filament organizing center. *Journal of Cell Biology*, 92(2):575–578, 1982.
- [88] G. Embery, R.J. Waddington, R.C. Hall, and K.S. Last. Connective tissue elements as diagnostic aids in periodontology. *Periodontology 2000*, 24(1):193–214, 2000. [47](#)
- [89] S. Werner and H. Smola. Paracrine regulation of keratinocyte proliferation and differentiation. *Trends in Cell Biology*, 11(4):143–146, 2001. [47](#)
- [90] B.A. Harley, T.M. Freyman, M.Q. Wong, and L.J. Gibson. A New Technique for Calculating Individual Dermal Fibroblast Contractile Forces Generated within Collagen-GAG Scaffolds. *Biophysical Journal*, 93(8):2911, 2007. [48](#)
- [91] K.S. Chapple, E.J. Cartwright, G. Hawcroft, A. Tisbury, C. Bonifer, N. Scott, A.C.J. Windsor, P.J. Guillou, A.F. Markham, P.L. Coletta, et al. Localization of Cyclooxygenase-2 in Human Sporadic Colorectal Adenomas. *American Journal of Pathology*, 156(2):545–553, 2000.
- [92] S.A. Smith and B.A. Dale. Immunologic Localization of Filaggrin in Human Oral Epithelia and Correlation with Keratinization. *Journal of Investigative Dermatology*, 86(2):168–172, 1986.
- [93] A. Mahdavi, L. Ferreira, C. Sundback, J.W. Nichol, E.P. Chan, D.J.D. Carter, C.J. Bettinger, S. Patanavanich, L. Chignozha, E. Ben-Joseph, A. Galakatos, H. Pryor, I. Pomerantseva, P.T. Masiakos, W. Faquin, A. Zumbuehl, S. Hong, J. Borenstein, J. Vacanti, R. Langer, and J.M. Karp. A biodegradable and biocompatible gecko-inspired tissue adhesive. *Proceedings of the National Academy of Sciences*, 105(7):2307–2312, 2008. [57](#)

- [94] J. M. Vasiliev. Polarization of pseudopodial activities: cytoskeletal mechanisms. *Journal of Cell Science*, 98(1):1–4, 1991. [64](#)
- [95] G. T. Charras, C. K. Hu, M. Coughlin, and T. J. Mitchison. Reassembly of contractile actin cortex in cell blebs. *The Journal of Cell Biology*, 175(3):477, 2006.
- [96] T. D. Pollard and G. G. Borisy. Cellular motility driven by assembly and disassembly of actin filaments. *Cell*, 112(4):453–65, 2003.
- [97] R. Pelham and F. Chang. Actin dynamics in the contractile ring during cytokinesis in fission yeast. *Nature*, 419(6902):82–86, 2002.
- [98] B. Qualmann, M. M. Kessels, and R. B. Kelly. Molecular links between endocytosis and the actin cytoskeleton. *Journal of Cell Biology*, 150(5):F111–6, 2000. [64](#)
- [99] H. Braak and E. Braak. Pathoanatomy of Parkinson’s disease. *Journal of Neurology*, 247(14), 2000. [64](#)
- [100] J.D. Fine, E. Bauer, R.A. Briggaman, D.M. Carter, R.A.J. Eady, N.B. Esterly, K.A. Holbrook, S. Hurwitz, L. Johnson, A. Lin, et al. Revised clinical and laboratory criteria for subtypes of inherited epidermolysis bullosa. *Journal of the American Academy of Dermatology*, 24(1):119–135, 1991. [64](#)
- [101] E. Braak, K. Griffing, K. Arai, J. Bohl, H. Bratzke, and H. Braak. Neuropathology of Alzheimer’s disease: what is new since A. Alzheimer? *European Archives of Psychiatry and Clinical Neuroscience*, 249(9):14–22, 1999. [64](#)
- [102] R.D. Terry. The pathogenesis of Alzheimer disease: An alternative to the amyloid hypothesis. *Journal of neuropathology and experimental neurology*, 55(10):1023–1025, 1996.
- [103] V.M.Y. Lee. Disruption of the cytoskeleton in Alzheimer’s disease. *Current Opinion in Neurobiology*, 5(5):663–668, 1995. [64](#)
- [104] H. Lodish, A. Berk, S. L. Zipursky, P. Matsudaira, D. Baltimore, and J. Darnell. *Molecular cell biology*. W,H. Freeman, 2000. [64](#), [74](#), [91](#)

- [105] T.M. Svitkina, A.B. Verkhovskiy, and G.G. Borisy. Improved Procedures for Electron Microscopic Visualization of the Cytoskeleton of Cultured Cells. *Journal of Structural Biology*, 115(3):290–303, 1995. [64](#)
- [106] Bruce Alberts. *Molecular Biology of the Cell*. Garland, 2006. [64](#), [95](#)
- [107] N. Wang, J. P. Butler, and D. E. Ingber. Mechanotransduction across the cell surface and through the cytoskeleton. *Science*, 260(5111):1124–1127, 1993. [67](#)
- [108] P.A. Janmey. The cytoskeleton and cell signaling: Component localization and mechanical coupling. *Physiological Reviews*, 78(3):763–781, 1998. [64](#)
- [109] E. Helfer, S. Harlepp, L. Bourdieu, J. Robert, FC MacKintosh, and D. Chateau. Buckling of Actin-Coated Membranes under Application of a Local Force. *Physical Review Letters*, 87(8):88103, 2001. [64](#)
- [110] P.A. Janmey, S. Hvidt, J. Kas, D. Lerche, A. Maggs, E. Sackmann, M. Schliwa, and T.P. Stossel. The mechanical properties of actin gels. Elastic modulus and filament motions. *Journal of Biological Chemistry*, 269(51):32503–32513, 1994.
- [111] M. L. Gardel, J. H. Shin, F. C. MacKintosh, L. Mahadevan, P. Matsudaira, and D. A. Weitz. Elastic behavior of cross-linked and bundled actin networks. *Science*, 304(5675):1301–1305, 2004. [91](#), [120](#)
- [112] M. L. Gardel, F. Nakamura, J. Hartwig, J. C. Crocker, T. P. Stossel, and D. A. Weitz. Stress-dependent elasticity of composite actin networks as a model for cell behavior. *Physical Review Letters*, 96(8):88102, 2006. [71](#), [72](#), [91](#), [120](#)
- [113] P. M. Bendix, G. H. Koenderink, D. Cuvelier, Z. Dogic, B. N. Koeleman, W. M. Briehner, C. M. Field, L. Mahadevan, and D. A. Weitz. A quantitative analysis of contractility in active cytoskeletal protein networks. *Biophysical Journal*, 94(8):3126–36, 2008. [64](#)
- [114] D. Bray and J. G. White. Cortical flow in animal cells. *Science*, 239(4842):883–888, 1988. [64](#)
- [115] B. Geiger. Membrane-cytoskeleton interaction. *BBA-Reviews on Biomembranes*, 737(3-4):305–341, 1983. [64](#)

- [116] W.H. Roos, J. Ulmer, S. Grter, T. Surrey, and J.P. Spatz. Microtubule gliding and cross-linked microtubule networks on micropillar interfaces. *Nano Letters*, 5(12):2630–2634, 2005. [65](#), [67](#)
- [117] U. Eichenlaub-Ritter and J. B. Tucker. Microtubules with more than 13 protofilaments in the dividing nuclei of ciliates. *Nature*, 307(5946):60–62, 1984. [66](#)
- [118] J. Howard, Author, R. L. Clark, and Reviewer. Mechanics of motor proteins and the cytoskeleton. *Applied Mechanics Reviews*, 55(2):B39, 2002. [66](#), [74](#)
- [119] A. Desai and T.J. Mitchison. Microtubule polymerization dynamics. *Annual Review of Cell and Developmental Biology*, 13(1):83–117, 1997.
- [120] S Reinsch and P Gonczy. Mechanisms of nuclear positioning. *Journal of Cell Science*, 111(16):2283–2295, 1998.
- [121] T. Wittmann, A. Hyman, and A. Desai. The spindle: a dynamic assembly of microtubules and motors. *Nature Cell Biology*, 3(1):E28–E34, 2001.
- [122] F. Verde, M. Dogterom, E. Stelzer, E. Karsenti, and S. Leibler. Control of microtubule dynamics and length by cyclin a- and cyclin b- dependent kinases in xenopus egg extracts. *Journal of Cell Biology*, 118(5):1097–1108, 1992. [67](#)
- [123] F. Gittes, B. Mickey, J. Nettleton, and J. Howard. Flexural rigidity of microtubules and actin filaments measured from thermal fluctuations in shape. *Journal of Cell Biology*, 120(4):923–934, 1993. [67](#)
- [124] Fr. Pampaloni, G. Lattanzi, JonA., T. Surrey, E. Frey, and E.L. Florin. Thermal fluctuations of grafted microtubules provide evidence of a length-dependent persistence length. *Proceedings of the National Academy of Sciences*, 103(27):10248–10253, 2006. [67](#)
- [125] B.L. Goode, D.G. Drubin, and G.Barnes. Functional cooperation between the microtubule and actin cytoskeletons. *Current Opinion in Cell Biology*, 12(1):63 – 71, 2000. [67](#)
- [126] C.P. Brangwynne, F.C. MacKintosh, S. Kumar, N.A. Geisse, J. Talbot, L. Mahadevan, K.K. Parker, D.E. Ingber, and D.A. Weitz. Microtubules can bear

- enhanced compressive loads in living cells because of lateral reinforcement. *Journal of Cell Biology*, 173(5):733, 2006. [67](#)
- [127] D. E. Ingber. Tensegrity: The architectural basis of cellular mechanotransduction. *Annual Reviews in Physiology*, 59(1):575–599, 1997. [67](#)
- [128] R.D. Vale and R.A. Milligan. The Way Things Move: Looking Under the Hood of Molecular Motor Proteins. *Science*, 288(5463):88, 2000. [67](#), [74](#)
- [129] T. Surrey, F. Nedelec, S. Leibler, and E. Karsenti. Physical properties determining self-organization of motors and microtubules. *Science*, 292(5519):1167–1171, 2001. [67](#)
- [130] K. C. Holmes. Solving the structures of macromolecular complexes. *Structure*, 2(7):589–593, 1994. [68](#)
- [131] E.S. Bullitt. Three-dimensional reconstruction of an actin bundle. *The Journal of Cell Biology*, 107(2):597–611, 1988. [68](#)
- [132] C. Frieden. Actin and tubulin polymerization: The use of kinetic methods to determine mechanism. *Annual Reviews in Biophysics and Biophysical Chemistry*, 14(1):189–210, 1985.
- [133] T. D. Pollard and J. A. Cooper. Actin and actin-binding proteins. a critical evaluation of mechanisms and functions. *Annual Reviews in Biochemistry*, 55(1):987–1035, 1986.
- [134] L. D. Burtnick, E. K. Koepf, J. Grimes, E. Y. Jones, D. I. Stuart, P. J. McLaughlin, and R. C. Robinson. The crystal structure of plasma gelsolin: Implications for actin severing, capping, and nucleation. *Cell*, 90:661–670, 1997.
- [135] Y. Yang, J. Dowling, Q. C. Yu, P. Kouklis, D. W. Cleveland, and E. Fuchs. An essential cytoskeletal linker protein connecting actin microfilaments to intermediate filaments. *Cell*, 86(4):655–65, 1996.
- [136] L. M. Griffith and T. D. Pollard. Cross-linking of actin filament networks by self-association and actin-binding macromolecules. *Journal of Biological Chemistry*, 257(15):9135–9142, 1982.

- [137] T.P. Stossel, J. Condeelis, L. Cooley, J.H. Hartwig, A. Noegel, M. Schleicher, and S.S. Shapiro. Filamins as integrators of cell mechanics and signalling. *Nature Reviews of Molecular Cell Biology*, 2(2):138–145, 2001. [71](#), [72](#), [94](#)
- [138] T.P. Stossel, C. Chaponnier, R.M. Ezzell, J.H. Hartwig, P.A. Janmey, D.J. Kwiatkowski, S.E. Lind, D.B. Smith, F.S. Southwick, and H.L. Yin. Non-muscle actin-binding proteins. *Annual Reviews in Cell Biology*, 1(1):353–402, 1985.
- [139] J.M. Tyler, J.M. Anderson, and D. Branton. Structural comparison of several actin-binding macromolecules. *Journal of Cell Biology*, 85(2):489–495, 1980.
- [140] R.H. Gomer and E. Lazarides. The synthesis and deployment of filamin in chicken skeletal muscle. *Cell*, 23(2):524–32, 1981.
- [141] R.H. Gomer. Switching of filamin polypeptides during myogenesis in vitro. *The Journal of Cell Biology*, 96(2):321–329, 1983.
- [142] M. Li, M.e Serr, K. Edwards, S. Ludmann, D. Yamamoto, L.G. Tilney, C. M. Field, and T.S. Hays. Filamin is required for ring canal assembly and actin organization during drosophila oogenesis. *Journal of Cell Biology*, 146(5):1061–1074, 1999.
- [143] R.R. Weihing. The filamins: properties and functions. *Canadian Journal of Biochemistry and Cell Biology*, 63(6):397–413, 1985.
- [144] K. Wang and SJ Singer. Interaction of Filamin with F-Actin in Solution. *Proceedings of the National Academy of Sciences*, 74(5):2021–2025, 1977.
- [145] E.A. Brotschi, J.H. Hartwig, and T.P. Stossel. The gelation of actin by actin-binding protein. *Journal of Biological Chemistry*, 253(24):8988–8993, 1978.
- [146] T. Ito, A. Suzuki, and TP Stossel. Regulation of water flow by actin-binding protein-induced actin gelatin. *Biophysical Journal*, 61(5):1301–1305, 1992.
- [147] W.H. Goldmann and G. Isenberg. Analysis of filamin and a-actinin binding to actin by stopped flow method. *FEBS Letters*, 336(3):408–410, 1993.

- [148] Makoto Honda, Kingo Takiguchi, Satoshi Ishikawa, and Hirokazu Hotani. Morphogenesis of liposomes encapsulating actin depends on the type of actin-crosslinking. *Journal of Molecular Biology*, 287(2):293 – 300, 1999.
- [149] J.H. Hartwig, J. Tyler, and T.P. Stossel. Actin-binding protein promotes the bipolar and perpendicular branching of actin filaments. *Journal of Cell Biology*, 87(3):841–848, 1980.
- [150] A. Blanchard, V. Ohanian, and D. Critchley. The structure and function of alpha-actinin. *Journal of Muscle Research and Cell Motility*, 10(4):280–9, 1989. [72](#)
- [151] D. H. Wachsstock, W. H. Schwartz, and T. D. Pollard. Affinity of alpha-actinin for actin determines the structure and mechanical properties of actin filament gels. *Biophysical Journal*, 65(1):205–214, 1993. [72](#)
- [152] M. Tempel, G. Isenberg, and E. Sackmann. Temperature-induced sol-gel transition and microgel formation in alpha -actinin cross-linked actin networks: A rheological study. *Physical Review E*, 54(2):1802, 1996. [73](#)
- [153] M.C. Lebart, C. Mejean, C. Roustan, and Y. Benyamin. Further characterization of the alpha-actinin-actin interface and comparison with filamin-binding sites on actin. *Journal of Biological Chemistry*, 268(8):5642–5648, 1993. [73](#)
- [154] B. Sjoebloom, A. Salmazo, and K. Djinovi-Carugo. Alpha-actinin structure and regulation. *Cellular and Molecular Life Sciences*, 65(17):2688–2701, 2008. [73](#)
- [155] R. Cooke. The mechanism of muscle contraction. *CRC Critical Reviews in Biochemistry*, 21(1):53–118, 1986. [73](#)
- [156] H.V. Sellers, J.R. and Goodson. Motor Proteins 2: Myosin Protein Profile. *Protein Profile*, 2(12), 1995. [73](#)
- [157] S.J. Kron and J.A. Spudich. Fluorescent Actin Filaments Move on Myosin Fixed to a Glass Surface. *Proceedings of the National Academy of Sciences*, 83(17):6272–6276, 1986. [73](#)
- [158] S.S. Margossian and S. Lowey. Preparation of myosin and its subfragments from rabbit skeletal muscle. *Methods Enzymol*, 85(Pt B):55–71, 1982. [74](#), [84](#)

- [159] Y.Y. Toyoshima, S.J. Kron, E.M. McNally, K.R. Niebling, C. Toyoshima, and J.A. Spudich. Myosin subfragment-1 is sufficient to move actin filaments in vitro. *Nature*, 328(6130):536–539, 1987. [74](#)
- [160] A. Kishino and T. Yanagida. Force measurements by micromanipulation of a single actin filament by glass needles. *Nature*, 334(6177):74–76, 1988. [74](#)
- [161] H.E. Huxley. The contraction of muscle. *Science America*, 199(5):67–72, 1958. [74](#)
- [162] A. Ishijima, T. Doi, K. Sakurada, and T. Yanagida. Sub-piconewton force fluctuations of actomyosin in vitro. *Nature*, 352(6333):301–306, 1991. [74](#)
- [163] T.D. Pollard. The myosin crossbridge problem. *Cell*, 48(6):909–10, 1987. [74](#)
- [164] E. Pate, GJ Wilson, M. Bhimani, and R. Cooke. Temperature dependence of the inhibitory effects of orthovanadate on shortening velocity in fast skeletal muscle. *Biophysical Journal*, 66(5):1554–1562, 1994. [74](#)
- [165] R. Cooke, K. Franks, GB Luciani, and E. Pate. The inhibition of rabbit skeletal muscle contraction by hydrogen ions and phosphate. *The Journal of Physiology*, 395(1):77–97, 1988.
- [166] Y.Y. Toyoshima, C. Toyoshima, and J.A. Spudich. Bidirectional movement of actin filaments along tracks of myosin heads. *Nature*, 341(6238):154–156, 1989. [74](#)
- [167] C.H.J. Schmitz, K. Uhrig, J.P. Spatz, and J.E. Curtis. Tuning the orbital angular momentum in optical vortex beams. *Optics Express*, 14(15):6604–6612, 2006.
- [168] F. Merenda, G. Boer, J. Rohner, G. Delacrtaz, and R. P. Salath. Escape trajectories of single-beam optically trapped micro-particles in a transverse fluid flow. *Optics Express*, 14(4):1685–1699, 2006. [75](#)
- [169] K. Uhrig. *Investigation of Molecular Interactions in Cytoskeletal Systems with Holographic Optical Tweezers*. PhD thesis, 2009. [76](#), [112](#)
- [170] W. Roos. Biomimetic cytoskeleton assemblies and living cells on micropillar force sensor arrays. *Ph.D.Thesis*, 2004. [77](#)

- [171] D.C. Duffy, J.C. McDonald, O. J.A. Schueller, and G.M. Whitesides. Rapid prototyping of microfluidic systems in poly(dimethylsiloxane). *Anal Chem*, 70:4974–4984, 1998. 77
- [172] Y.N. Xia and G.M. Whitesides. Softlithography. *Angewandte Chemie International Edition England*, 37:551–577, 1998. 77
- [173] C.H.J. Schmitz, A.C. Rowat, S. Koster, and D.A. Weitz. Dropspots: a picoliter array in a microfluidic device. *Lab on a Chip*, 9:44–49, 2009. 1. 80
- [174] M. Morra, E. Occhiello, R. Marola, F. Garbassi, P. Humphrey, and D. Johnson. On the aging of oxygen plasma-treated polydimethylsiloxane surfaces. *Journal of Colloid Interface Science*, 137(1):1124, 1990. 80
- [175] M.K. Chaudhury and G.M. Whitesides. Direct measurement of interfacial interactions between semispherical lenses and flat sheets of poly (dimethylsiloxane) and their chemical derivatives. *Langmuir*, 7(5):1013–1025, 1991.
- [176] M.K. Chaudhury and G.M. Whitesides. Correlation between surface free energy and surface constitution. *Science*, 255(5049):1230–1232, 1992. 80
- [177] J. W. Park Lin, M. Protein solubility in pacific whiting affected by proteolysis during storage. *Journal of Food Science*, 61(3):536–539, 1996.
- [178] A. Coffey, B. van den Burg, R. Veltman, and T. Abee. Characteristics of the biologically active 35-kda metalloprotease virulence factor from listeria monocytogenes. *Journal of Applied Microbiology*, 88(1):132–141, 2000.
- [179] A. V. Morozova, I. N. Skovorodkin, S. Yu Khaitlina, and A. Yu Malinin. Bacterial protease ecp32 specifically hydrolyzing actin and its effect on cytoskeleton in vivo. *Biochemistry (Moscow)*, 66(1):83–90, 2001.
- [180] J.X. Tang, P.A. Janmey, T.P. Stossel, and T. Ito. Thiol oxidation of actin produces dimers that enhance the elasticity of the f-actin network. *Biophysical Journal*, 76(4):2208–2215, 1999.
- [181] S. Ishiwata. Freezing of actin. reversible oxidation of a sulfhydryl group and structural change. *Journal of Biochemistry*, 80(3):595, 1976.

- [182] J. D. Pardee and J. A. Spudich. Purification of muscle actin. *Methods Enzymology*, 85 Pt B:164–81, 1982. [81](#)
- [183] S. MacLean-Fletcher and T.D. Pollard. Identification of a factor in conventional muscle actin preparations which inhibits actin filament self-association. *Biochemical and Biophysical Research Communication*, 96(1):18–27, 1980. [81](#)
- [184] R.O. Hynes. Integrins: a family of cell surface receptors. *Cell*, 48(4):549–554, 1987.
- [185] W.Z. Cande. Preparation of N-ethylmaleimide-modified heavy meromyosin and its use as a functional probe of actomyosin-based motility. *Methods Enzymology*, 134:473–7, 1986.
- [186] R.L. DeBiasio. The dynamic distribution of fluorescent analogues of actin and myosin in protrusions at the leading edge of migrating Swiss 3T3 fibroblasts. *The Journal of Cell Biology*, 107(6):2631–2645, 1988.
- [187] Y. Shizuta, H. Shizuta, M. Gallo, P. Davies, and I. Pastan. Purification and properties of filamin, and actin binding protein from chicken gizzard. *Journal of Biological Chemistry*, 251(21):6562–6567, 1976. [86](#)
- [188] Y. Tseng and D. Wirtz. Mechanics and multiple-particle tracking microheterogeneity of  $\alpha$ -actinin-cross-linked actin filament networks. *Biophysical Journal*, 81(3):1643–1656, 2001. [91](#)
- [189] D.H. Wachsstock, W.H. Schwarz, and T.D. Pollard. Cross-linker dynamics determine the mechanical properties of actin gels. *Biophysical Journal*, 66(3):801–809, 1994.
- [190] M. Claessens, R. Tharmann, K. Kroy, and A. Bausch. Microstructure and viscoelasticity of confined semiflexible polymer networks. *Nature Physics*, 2(3):186–189, 2006.
- [191] P. Dalhaimer, D.E. Discher, and T.C. Lubensky. Crosslinked actin networks show liquid crystal elastomer behaviour, including soft-mode elasticity. *Nature Physics*, 3(5):354–360, 2007.

- [192] J. Xu, D. Wirtz, and T.D. Pollard. Dynamic cross-linking by alpha -actinin determines the mechanical properties of actin filament networks. *Journal of Biological Chemistry*, 273(16):9570–9576, 1998. [91](#)
- [193] Y. Tsuda, H. Yasutake, A. Ishijima, and T. Yanagida. Torsional rigidity of single actin filaments and actin-actin bond breaking force under torsion measured directly by in vitro micromanipulation. *Proceedings of the National Academy of Sciences*, 93(23):12937–12942, 1996. [91](#)
- [194] R. Bunk, J. Klinth, L. Montelius, I.A. Nicholls, P. Omling, S. Tagerud, and A. Mansson. Actomyosin motility on nanostructured surfaces. *Biochemical and Biophysical Research Communications*, 301(3):783–788, Feb 2003.
- [195] J.M. Ferrer, H. Lee, J. Chen, B. Pelz, F. Nakamura, R.D. Kamm, and M.J. Lang. Measuring molecular rupture forces between single actin filaments and actin-binding proteins. *Proceedings of the National Academy of Sciences*, 105(27):9221, 2008. [112](#), [121](#)
- [196] M.J. Footer, J.W.J. Kerssemakers, J.A. Theriot, and M. Dogterom. Direct measurement of force generation by actin filament polymerization using an optical trap. *Proceedings of the National Academy of Sciences*, 104(7):2181, 2007.
- [197] X. Liu and G. H. Pollack. Mechanics of f-actin characterized with microfabricated cantilevers. *Biophysical Journal*, 83(5):2705–15, 2002. [91](#)
- [198] W. Haeckl, M. Baermann, and E. Sackmann. Shape Changes of Self-Assembled Actin Bilayer Composite Membranes. *Physical Review Letters*, 80(8):1786–1789, 1998. [91](#)
- [199] K. Sengupta, L. Limozin, M. Tristl, I. Haase, M. Fischer, and E. Sackmann. Coupling artificial actin cortices to biofunctionalized lipid monolayers. *Langmuir*, 22(13):5776–5785, 2006.
- [200] L. Limozin, A. Roth, and E. Sackmann. Microviscoelastic Moduli of Biomimetic Cell Envelopes. *Physical Review Letters*, 95(17):178101, 2005. [91](#)

- [201] N.A. Patankar. Transition between superhydrophobic states on rough surfaces. *Langmuir*, 20(17):7097–7102, 2004.
- [202] F. Nakamura, E. Osborn, P.A. Janmey, and T.P. Stossel. Comparison of Filamin A-induced Cross-linking and Arp2/3 Complex-mediated Branching on the Mechanics of Actin Filaments. *Journal of Biological Chemistry*, 277(11):9148–9154, 2002.
- [203] P.A. Janmey, J.X. Tang, and C.F. Schmidt. Actin filaments. *Supramolecular Assemblies*, 2001.
- [204] G. S. Manning. The molecular theory of polyelectrolyte solutions with applications to the electrostatic properties of polynucleotides. *Quarterly Reviews of Biophysics*, 11(2):179–246, 1978.
- [205] R. Furukawa and M. Fechheimer. The structure, function, and assembly of actin filament bundles. *International Review of Cytology*, 175:29–90, 1997.
- [206] J. X. Tang and P. A. Janmey. The polyelectrolyte nature of f-actin and the mechanism of actin bundle formation. *Journal of Biological Chemistry*, 271(15):8556–63, 1996.
- [207] K. Kruse and F. Juelicher. Self-organization and mechanical properties of active filament bundles. *Physical Review E*, 67(5):051913, 2003.
- [208] W. Xian, J.X. Tang, P.A. Janmey, and W.H. Braunlin. The polyelectrolyte behavior of actin filaments: a 25mg nmr study. *Biochemistry*, 38(22):7219–26, 1999.
- [209] G.C.L. Wong, A. Lin, J.X. Tang, Y. Li, P.A. Janmey, and C.R. Safinya. Lamellar Phase of Stacked Two-Dimensional Rafts of Actin Filaments. *Physical Review Letters*, 91(1):18103, 2003.
- [210] M. Hase and K. Yoshikawa. Structural transition of actin filament in a cell-sized water droplet with a phospholipid membrane. *Journal of Chemical Physics*, 124(10):104903, 2006.
- [211] T. Haraszti, S. Schulz, K. Uhrig, R. Kurre, W. Roos, C.H.J. Schmitz, J.E. Curtis, T. Maier, A.E.M. Clemen, and Joachim P. Spatz. Biomimetic models of the actin cortex. *Biophysical Reviews and Letters*, 2009. accepted.

- [212] J. Uhde, M. Keller, E. Sackmann, A. Parmeggiani, and E. Frey. Internal motility in stiffening actin-myosin networks. *Physical Review Letters*, 93(26):268101, 2004.
- [213] D. Humphrey, C. Duggan, D. Saha, D. Smith, and J. Kaes. Active fluidization of polymer networks through molecular motors. *Nature*, 416(6879):413–416, 2002. [97](#), [120](#)
- [214] D.K. Lubensky and D.R. Nelson. Pulling Pinned Polymers and Unzipping DNA. *Physical Review Letters*, 85(7):1572–1575, 2000.
- [215] S. Cocco, R. Monasson, and J.F. Marko. Force and kinetic barriers to unzipping of the DNA double helix. *Proceedings of the National Academy of Sciences*, 98:8608–8613, 2001.
- [216] B. Essevaz-Roulet, U. Bockelmann, and F. Heslot. Mechanical separation of the complementary strands of DNA. *Proceedings of the National Academy of Sciences*, 94(22):11935–11940, 1997.
- [217] U. Bockelmann, P. Thomen, B. Essevaz-Roulet, V. Viasnoff, and F. Heslot. Unzipping DNA with Optical Tweezers: High Sequence Sensitivity and Force Flips. *Biophysical Journal*, 82(3):1537–1553, 2002.
- [218] C.W. Jones, J. C. Wang, R. W. Briehl, and M. S. Turner. Measuring forces between protein fibers by microscopy. *Biophysical Journal*, 88(4):2433–2441, 2005.
- [219] J. Kierfeld. Force-induced desorption and unzipping of semiflexible polymers. *Physical Review Letters*, 97(5):58302, 2006.
- [220] J. Kierfeld, T. Kühne, and R. Lipowsky. Discontinuous unbinding transitions of filament bundles. *Physical Review Letters*, 95(3):38102, 2005.
- [221] J. Kierfeld and R. Lipowsky. Unbundling and desorption of semiflexible polymers. *Europhysics Letters*, 62(2):285–291, 2003.
- [222] J. Kierfeld, P. Gutjahr, T. Kuhne, P. Kraikivski, and R. Lipowsky. Buckling, bundling, and pattern formation: From semi-flexible polymers to assemblies of interacting filaments. *Journal of Computational and Theoretical Nanoscience*, 3(6):898, 2006.

- [223] P. Gutjahr. *Conformations of semiflexible polymers and filaments*. PhD thesis, Mathematisch-Naturwissenschaftlichen Fakultät der Universität Potsdam, 2007. [104](#), [105](#), [106](#), [107](#), [111](#), [121](#)
- [224] J.E. Curtis, B.A. Koss, and D.G. Grier. Dynamic holographic optical tweezers. *Optics Communications*, 207(1-6):169–175, 2002.
- [225] J.E. Curtis, C.H.J. Schmitz, and J.P. Spatz. Symmetry dependence of holograms for optical trapping. *Optics Letters*, 30(16):2086–2088, 2005.
- [226] C.H. Schmitz, J. Curtis, and J.P. Spatz. Constructing and probing biomimetic models of the actin cortex with holographic optical tweezers. *Proceedings of SPIE*, 5514:446–454, 2004.
- [227] C. H. J. Schmitz, J. P. Spatz, and J. E. Curtis. High-precision steering of multiple holographic optical tweezers. *Optics Express*, 13:8678–8685, 2005.
- [228] H. Miyata, R. Yasuda, and K. Kinosita. Strength and lifetime of the bond between actin and skeletal muscle  $\alpha$ -actinin studied with an optical trapping technique. *Biochimica et Biophysica Acta*, 1290(1):83–88, 1996. [112](#), [121](#)
- [229] E. Evans. Probing the relation between force-lifetime and chemistry in single molecular bonds. *Annual Reviews in Biophysics and Biomolecular Structure*, 30(1):105–128, 2001.
- [230] O.K. Dudko, G. Hummer, and A. Szabo. Intrinsic Rates and Activation Free Energies from Single-Molecule Pulling Experiments. *Physical Review Letters*, 96(10):108101, 2006.
- [231] E. Evans and K. Ritchie. Dynamic strength of molecular adhesion bonds. *Biophysical Journal*, 72(4):1541–1555, 1997.
- [232] P.M. Williams. Analytical descriptions of dynamic force spectroscopy: behaviour of multiple connections. *Analytica Chimica Acta*, 479(1):107–115, 2003.



# Appendix



# A

## Abbreviations

**ABP** actin-binding protein

**AFM** atomic force microscopy

**ADP** adenosine-diphosphate

**ATP** adenosine-triphosphate

**BM** basement membrane

**CC** co-culture

**DTT** dithiothreitol

**cDNA** cyclic desoxyribonucleic acid

**DMEM** dulbeccos modified Eagles medium

**ECM** extracellular matrix

**G-actin** globular actin

**GAPDH** glycerinaldehyd-3-phosphat-dehydrogenase

**GCTF** gingival-connective-tissue fibroblast

**F-actin** filamentous actin

**FAK** focal adhesion kinase

**FN** fibronectin

- FCS** foetal calf serum
- HMM** heavy meromyosin
- IF** intermediate filaments
- IIF** indirect immunofluorescence
- IHGK** immortalized human gingival keratinocyte
- K1** keratin type-1
- K10** keratin type-10
- KGM** keratinocyte growth medium
- LMM** light meromyosin
- mRNA** messenger ribonucleic acid
- MT** microtubule
- NEMHMM** N-ethylmaleinimid-modified heavy meromyosin
- OT** optical tweezers
- PBS** phosphate buffered saline
- PCR** polymerase chain reaction
- PDMS** polydimethyl-siloxane
- PEG** polyethylene-glycol)
- qPCR** quantitative polymerase chain reaction
- RGD** amino acid sequence arginine-glycin-asparagine
- RT** room temperature
- SEM** scanning electron microscope
- sqPCR** semiquantitative polymerase chain reaction
- TRITC** tetra-rhodamine-isothiocyanate

# B

## Own Publications

C. Mohrdieck, F. Dalmas, E. Arzt, R. Tharmann, M. Claessens, A. Bausch, A. Roth, E. Sackmann, C. Schmitz, J. Curtis, W. Roos, S. Schulz, K. Uhrig, and J.P. Spatz. Biomimetic models of the actin cytoskeleton. *Small*, 3(6):1015-1022, 2007.

T. Steinberg, S. Schulz, J.P. Spatz, N. Grabe, E. Müssig, A. Kohl, G. Komposch, and P. Tomakidi. Early keratinocyte differentiation on micropillar interfaces. *Nano Letters*, 7(2):287-294, 2007.

E. Müssig, T. Steinberg, S. Schulz, J.P. Spatz, J. Ulmer, N. Grabe, A. Kohl, G. Komposch, and P. Tomakidi. Connective-tissue fibroblasts established on micropillar interfaces are pivotal for epithelial-tissue morphogenesis. *Advanced Functional Materials*, 66(6):422-433, 2008.

T. Haraszti, S. Schulz, K. Uhrig, R. Kurre, W. Roos, C.H.J. Schmitz, J.E. Curtis, T. Maier, A.E.M. Clemen, and J.P. Spatz. Biomimetic models of the actin cortex. *Biophysical Reviews and Letters*, 2009, *accepted*.

E. Müssig, S. Schulz, J.P. Spatz, N. Ziegler, P. Tomakidi, and T. Steinberg. Distinct biomechanics of micropillar interfaces governs behavior of periodontal cells partly involved in mineralized tissue formation. *Journal of Bone and Mineral Research*, 2009, *submitted*



# Danksagung

Ganz besonders bedanken möchte ich mich in erster Linie bei meinem Betreuer Professor Joachim Spatz. Er gab mir die Möglichkeit, dieses interessante Themengebiet zu bearbeiten und die Freiheit, mich wissenschaftlich zu entfalten. Er war immer bereit, Probleme zu diskutieren, die sich während meiner Arbeit auftaten und gab mir die Möglichkeit, meine Arbeit zu präsentieren.

In einem so interdisziplinären Forschungsgebiet wie dem unsrigen ist Zusammenarbeit ungemein wichtig. Ohne die Unterstützung vieler Mitglieder unserer Gruppe und anderer wäre diese Arbeit nicht möglich gewesen.

Besonders danken möchte ich bei meinen Kooperationspartnern der "Kopfambulanz" PD Dr. Thorsten Steinberg, Prof. Pascal Tomakidi und Dr. Eva Müssig. Die immer nette Atmosphäre und die gute Zusammenarbeit trugen einen wesentlichen Teil zum Gelingen dieser Arbeit bei.

Ich möchte mich bedanken bei Dr. Tamás Haraszti. Zu ihm konnte ich immer kommen wenn ich an die Grenzen meines physikalischen Verständnisses gekommen war. Er war immer bereit, mir zu helfen, auch in der sehr stressigen Zeit meines Zusammenschreibens. Thank you Tamás for helping me throughout my whole time in this group and for spending the time to correct my thesis. Without you, it would not have been possible to complete this work.

Bedanken möchte ich mich auch bei Dr. Wouter Roos, von dem ich während meiner Diplomarbeit viel über Aktin gelernt habe.

Im Laufe so einer Doktorarbeit ist es auch wichtig, dass es Leute gibt, die dafür sorgen, dass man nicht im Sumpf der Bürokratie versinkt, und die einem Unannehmlichkeiten vom Hals halten. Besonders danken möchte ich daher Frau Boczek, die alles für ihre Jungs getan hat und auf die man sich immer verlassen konnte.

Bedanken möchte ich mich auch bei Frau Schönig-Erdinger, Frau Pfeilmeier und allen anderen, die administrative Dinge für mich erledigt haben.

Bedanken möchte ich mich auch bei unseren ehemaligen Mitstreitern unseres Arbeitskreises. Sie ermöglichten mir einen reibungslosen Einstieg in meine Doktorarbeit. Ich möchte allen Mitglieder des AK Spatz danken für die angenehme Arbeitsatmosphäre, besonders bei der Voggl-Fisch-Fisch-Voggl-Crew Babak Hosseini, Daniel Aydin, Kai Uhrig, Ilia Louban, Theo Lohmüller und Janosch Dreeg aus dem Heiderberger Teil unseres Arbeitskreises und Ferdi Belz und Marco Schwieder aus dem Stuttgarter Teil. Sie waren immer für fachliche Gespräche zu haben und sorgten auch abseits der Arbeit für gute Laune. Unsere gemeinsamen Abende und unsere Seminare in Antholz werden unvergessen bleiben. Danke Jungs!

Dem Herrn Babak, dem Herrn Daniel, dem Herrn Ilia, Jasmin Zahn und Nadine Perschmann möchte ich für die Korrektur meiner Arbeit danken und dafür, dass sie mir die Zeit des Schreibens erleichtert haben.

Ich möchte Dr. Anabel Clemen für die ausgedehnten fachlichen Gespräche danken. Danken möchte ich auch unseren Technikern Christine Mollenhauer und Richard Morlang und letztendlich den Handwerkern unserer Werkstatt.

Ich könnte die Liste der Leute, die ich während meiner Arbeit kennen und schätzen gelernt habe noch seitenlang füllen, aber hiermit danke ich einfach kurz und schmerzlos allen.

Diederik Berghauser-Pont hat mich während meines Studiums finanziell unterstützt, auch ihm danke ich.

Ich möchte meiner Schwester, Uli und Britta danken, die immer ein offenes Ohr für Probleme hatten.

Zuletzt möchte ich meiner Familie danken. Besonders ohne die immerwährende Unterstützung meiner Eltern würde ich nicht hier sitzen und diese letzten Zeilen verfassen. Sie standen mir in allen Lagen zur Seite und ich konnte mich immer auf sie verlassen. Sie taten immer alles für ihren "Jungen". Ich widme Euch daher diese Arbeit.

Ich erkläre hiermit, dass ich die vorgelegte Dissertation selbst verfasst und mich keiner anderen als der von mir ausdrücklich bezeichneten Quellen und Hilfen bedient habe.

Heidelberg, den 02. Februar 2009

.....

Simon Daniel Schulz